UNIVERSITY OF OKLAHOMA

GRADUATE COLLEGE

TRANSFER ZONES IN LISTRIC NORMAL FAULT SYSTEMS

A DISSERTATION

SUBMITTED TO THE GRADUATE FACULTY

in partial fulfillment of the requirements for the

Degree of

DOCTOR OF PHILOSOPHY

By

SHAMIK BOSE
Norman, Oklahoma
2010

TRANSFER ZONES IN LISTRIC NORMAL FAULT SYSTEMS

A DISSERTATION APPROVED FOR THE
CONOCOPHILLIPS SCHOOL OF GEOLOGY AND GEOPHYSICS

BY

Dr. Shankar Mitra, Chair

Dr. Ze'ev Reches

Dr. G. Randy Keller

Dr. May Yuan

Dr. Raymon Brown

This work is dedicated to

My grandmother, Mimi,

For showing the path to all of us

ACKNOWLEDGEMENTS

I am extremely grateful to my advisor, Dr. Shankar Mitra for providing invaluable guidance, insight and constant encouragement during my entire research. I would also like to thank Dr. Ze'ev Reches, Dr. G. Randy Keller, Dr. May Yuan and Dr. Raymon Brown for their immense help and suggestions in improving the dissertation. I am grateful to ExxonMobil for donating 3D seismic and well data from the South Timbalier block 54 and particularly to Doug Sturgis and Lori Summa of ExxonMobil Corporation for their constant efforts during the entire process. I am grateful to GeoLogic Systems for providing free licenses for Lithotect, to Landmark for providing academic licenses of GoCAD and to Schlumberger for licenses of Petrel. I would like to thank my fellow graduate students and staff at the ConocoPhillips School of Geology and Geophysics for their support. I am also thankful to my fellow past and present co-workers Subhotosh Banerjee, Kajari Ghosh and Debapriya Paul for numerous discussions that were greatly beneficial to my research. I am fortunate enough to have as my aunt, Prof. Sudipta Sengupta of Jadavpur University, India, who first introduced me to the fascinating world of structural geology even before I could spell "geology". My parents and family are my greatest strengths, who have sacrificed their all to make me what I am. I can never thank them enough. And lastly I would like to thank my wife, Rumela Bose for her immense support and patience without which my PhD would not have been possible.

TABLE OF CONTENTS

ABSTRACT

Listric normal faults are common in passive margin settings where sedimentary units are detached above weaker lithological units, such as evaporites or are driven by basal structural and stratigraphic discontinuities. The geometries and styles of faulting vary with the types of detachment and form landward and basinward dipping fault systems. Complex transfer zones therefore develop along the terminations of adjacent faults where deformation is accommodated by secondary faults, often below seismic resolution. The rollover geometry and secondary faults within the hanging wall of the major faults also vary with the styles of faulting and contribute to the complexity of the transfer zones. This study tries to understand the controlling factors for the formation of the different styles of listric normal faults and the different transfer zones formed within them, by using analog clay experimental models. Detailed analyses with respect to fault orientation, density and connectivity have been performed on the experiments in order to gather insights on the structural controls and the resulting geometries. A new high resolution 3D laser scanning technology has been introduced to scan the surfaces of the clay experiments for accurate measurements and 3D visualizations. Numerous examples from the Gulf of Mexico have been included to demonstrate and geometrically compare the observations in experiments and real structures. A salt cored convergent transfer zone from the South Timbalier Block 54, offshore Louisiana has been analyzed in detail to understand the evolutionary history of the region, which helps in deciphering the kinematic growth of similar structures in the Gulf of Mexico. The dissertation is divided

into three chapters, written in a journal article format, that deal with three different aspects in understanding the listric normal fault systems and the transfer zones so formed.

The first chapter involves clay experimental models to understand the fault patterns in divergent and convergent transfer zones. Flat base plate setups have been used to build different configurations that would lead to approaching, normal offset and overlapping faults geometries. The results have been analyzed with respect to fault orientation, density, connectivity and 3D geometry from photographs taken from the three free surfaces and laser scans of the top surface of the clay cake respectively.

The second chapter looks into the 3D structural analysis of the South Timbalier Block 54, offshore Louisiana in the Gulf of Mexico with the help of a 3D seismic dataset and associated well tops and velocity data donated by ExxonMobil Corporation. This study involves seismic interpretation techniques, velocity modeling, cross section restoration of a series of seismic lines and 3D subsurface modeling using depth converted seismic horizons, well tops and balanced cross sections.

The third chapter deals with the clay experiments of listric normal fault systems and tries to understand the controls on geometries of fault systems with and without a ductile substrate. Sloping flat base plate setups have been used and silicone fluid underlain below the clay cake has been considered as an analog for salt. The experimental configurations have been varied with respect to three factors viz. the direction of slope with respect to extension, the termination of silicone polymer with respect to the basal discontinuities and overlap of the base plates. The analyses for the experiments have again been performed from photographs and 3D laser scans of the clay surface.

CHAPTER 1

ANALOG MODELING OF DIVERGENT AND CONVERGENT TRANSFER ZONES IN LISTRIC NORMAL FAULT SYSTEMS

Abstract

Transfer zones are common features in passive margins such as the Gulf of Mexico, where deformation between adjacent listric normal faults is accommodated by the formation of complex secondary fault systems. Two common types of transfer zones are: (1) Convergent, with the main faults dipping towards each other and (2) Divergent, with the main faults dipping away from each other. Analog clay models are developed for both Convergent and Divergent transfer zones based on the relative position of the faults, with the faults (a) approaching each other, (b) offset by 90 degrees and (c) overlapping each other. During extension, the structures initiate as symmetric grabens and later transform into asymmetric half-grabens. The main fault and associated synthetic faults form a narrow zone of deformation whereas the antithetic faults develop into a broader zone constituting evenly spaced discrete fault segments. Orientations, lengths, densities and sizes of connected fault clusters vary with the type of transfer zone, structural position relative to the fault offsets, and total extension. The experiments show that the antithetic faults in convergent transfer zones and synthetic faults in divergent transfer zones tend to be more consistent in orientation and connect easily. Synthetic faults in convergent transfer zones and antithetic faults in divergent transfer zones change orientation along strike towards the transfer zone. Fault connectivity in approaching transfer zones is generally higher than in normal offset or overlapping configurations. The analog models provide important insights into the evolution of faults, the geometry of fault patterns and possible fluid migration pathways within transfer zones.

1.1 Introduction

Transfer zones are common features in passive margin settings such as the Gulf of Mexico, where the deformation between adjacent terminating listric normal faults is accommodated by the formation of complex secondary fault systems. Transfer zones in rift systems have been studied in detail, both at the surface and in the subsurface, and by using experimental and numerical models (McClay, 1989; Morley et al., 1990; Moustafa, 2002). However, there are very few studies on the evolution and deformation of transfer zones in listric normal fault systems, where the deformation patterns are more complex, because of the presence of rollover folds and secondary synthetic and antithetic faults (Figure 1.1). Although normal faults in rifts can also be listric at the crustal scale, the related complexities will typically not be seen at a much larger scale.

Transfer zones involving opposite-dipping faults can be classified as Divergent and Convergent depending on the dip directions of the main faults (Figure 1.2). Based on the relative locations of fault terminations, they can be further classified as Approaching, Normal offset and Overlapping, depending on whether the two faults are approaching each other, are offset by 90°, or have an overlapping zone between them, respectively (Figure 1.2 a to c).

Worrall and Snelson (1989) suggested that parts of the Texas shelf in the Gulf of Mexico shelf are characterized by long fault systems, mostly dipping basinward, whereas the Louisiana shelf is characterized by shorter, more arcuate fault systems, dipping both landward and basinward. The latter system, commonly associated with near surface salt structures in both regional and counter-regional systems, contain numerous examples of both convergent and divergent transfer zones, which provide important trapping

mechanisms for hydrocarbons. The growth fault systems in the Gulf of Mexico have been studied by a number of authors using balanced cross sections (McBride et al., 1998; Rowan et al., 1999, 1994; Diegel et al., 1995; Rowan, 1995; Worrall and Snelson, 1989) but the evolution of transfer zones in these fault systems have been rarely discussed.

In this paper, analog clay modeling has been used to understand the evolution of structures and related faults in both convergent and divergent transfer zones. A new method of three-dimensional laser scanning is used to analyze the progressive evolution of the structures. The focus is on the progressive evolution and interference of sub-seismic secondary synthetic and antithetic faults within the transfer zones.

1.1.1 Previous Work

Transfer zones in rift systems have been studied in detail by many authors, who have addressed fault linkages (Younes and McClay, 2002; Crider, 2001; Childs et al., 1995; Trudgill & Cartwright, 1994; Peacock and Sanderson, 1991), structural variations within different transfer zones (Moustafa, 2002; Rosendahl, 1987) and how they produce hydrocarbon traps (Morley et al., 1990). The different fault geometries and structural variations within transfer zones, based on relative positions of adjacent faults have been classified by Morley et al. (1990) and Fauld and Varga (1998). Analog experimental sand models have also been conducted in order to understand the role of salt substrate during formation of transfer zones (Le Calvez and Vendeville, 2002) and how en echelon faults form relay ramps in oblique extension.

Clay models have been successfully used in previous studies of listric fault systems for analyzing fault evolution and patterns during extension. Most setups consist

of a pre-existing rigid footwall ramp which defined the major fault surface. These setups are useful when studying only the secondary faults formed in response to the movement along the rigid ramp. However, they provide no information on the evolution of the main fault zone, footwall deformation in the main fault, or the evolution of transfer zones. Instead, experiments that involve the progressive evolution of the main faults through the model material are more useful for this purpose (Cloos, 1968; Serra and Nelson, 1988; Bose and Mitra, 2009).

1.1.2 Subsurface Examples of Transfer Zones in Listric Fault Systems

The growth fault patterns in the northern Gulf of Mexico vary from West in the Texas coast to the East along the Louisiana coast (Worrall and Snelson, 1989). The Texas growth fault system is characterized by long, basinward-dipping faults striking parallel to the Texas coastline. As a result, the transfer zones developed in this system are Synthetic transfer zones with the faults dipping in the same direction. The Louisiana system on the other hand consists of short, arcuate faults that comprise both basinward-dipping faults and counter-regional fault systems. This system therefore contains abundant examples of convergent and divergent transfer zone geometries, as well as synthetic transfer zones. Two examples have thus been chosen from offshore Louisiana (Figure 1.3), in order to illustrate the features of convergent and divergent transfer zones in a listric normal fault setting.

West Delta - Delta Farms field is located in the east-central Lafourche Parish, about 18 miles south-southwest of New Orleans (Figure 1.3). Subsurface maps of two producing horizons (Bausfield, 1983), the 6700 Sandstone marker and Textularia

Stapperi horizon (Figure 1.4) illustrate that the field is compartmentalized into two accumulations by the formation of a Divergent transfer zone between the regional faults (R1 and R2) and the counter-regional fault (CR1). One accumulation is located in the hanging wall rollover and the other in the structural high in the footwall caused by the transfer zone. The R1 and R2 merge at depth; however, they differ in timing with the R1 being older than R2 (Morgan, 1953) and this compartmentalizes the reservoir further.

The Lake Hatch field, located in east-central Terrebonne Parish (Figure 1.3), on the other hand, is an example of a Convergent transfer zone formed by the master regional fault (R3) and the counter-regional fault (CR2). The subsurface structure maps of 7800 and 9800 Sandstone markers (Conatser, 1983) reveal that the secondary faults form a complex framework and divide the reservoir into numerous compartments at depth (Figure 1.5). The locations of the traps are controlled by the structural highs in the rollovers, the configurations of the secondary antithetic and synthetic faults and the type of transfer zone.

The subsurface maps described above have been generated from about 150 well data and therefore do not have a high level of precision with respect to the number of faults and their exact orientations. Furthermore, the secondary antithetic and synthetic faults are below seismic resolution. Minor faults that cannot be interpreted from well and seismic data complicate the fault frameworks and influence production. Knowledge gathered from the experimental models regarding the structural relief and fault patterns in such settings can therefore be applied to enhance the precision of fault mapping. Calculation of density and connectivity at incremental steps during the progression of the experiments semi-quantitatively display the preferential growth of secondary faults in

certain areas as compared to others, thereby indicating the development of possible fluid migration pathways. An integrated overview of fault orientation, density, connectivity and structural relief provides insights ranging from structural evolution to migration and trap formation.

1.2 Experimental Methodology

1.2.1 Approach

Experimental clay models are used to study the geometry and evolution of convergent and divergent transfer zones, and the development of secondary faults in each of these systems. It has been established that wet clay can be used as modeling material since deformation in response to applied stress occurs in a similar manner as that in natural rocks (Oertel, 1965; Cloos, 1968; Hildebrand-Mittlefehldt, 1979; Reches, 1988). Both sand and clay possess similar coefficients of internal friction as natural rocks (0.5 and 0.6 for dry sand and wet clay respectively) and have cohesive strengths in the order of 10^{-4} to 10^{-5} of the cohesive strengths of upper crustal materials, thus allowing them to be used as scaled modeling materials (Hubbert, 1937; Withjack et al., 2007). The primary reason for selecting wet clay for the current experimental purposes was the deformation style of wet clay which, due to the higher ductility, generates distributed discrete faults (Rutter, 1986) and therefore enables various analyses to be performed with respect to length, orientation, density and displacement (Bose and Mitra, 2009).

The models involve two flat base plates overlying each other, with a clay cake on top (Cloos, 1968; Bose and Mitra, 2009). One of the base plates is attached to a fixed backstop and the other to a moveable backstop of the clay deformation table. The

moveable backstop is operated by two motors and pulled away at a constant rate of 0.4 mm/minute, thereby inducing basal displacement on the overlying clay. The initial thickness of the clay is maintained at about 8 cm for all the setups and the density at 1.6 to 1.65 gm/cc, which is ideal for the clay to support its own weight and yet form discrete faults when deformed. The flat base plate setup allows the major faults to evolve independently without any constraints such as rigid footwalls controlling their geometry.

Each base plate has indentations on the frontal edge that mimic the geometry of the six types of transfer zones being modeled (Figure 1.6). The master faults in the clay form along the contact edge of the overlapping plates and dip toward the lower plate. The physical significance of these contacts between overlapping plates is that they represent pre-existing structural and stratigraphic discontinuities which control the localization of the master faults. The geometry of the indentations and the configurations of overlap between the two plates enable the main faults to dip towards or away from each other, thereby giving rise to convergent or divergent transfer zones respectively (Figure 1.6). The angle of indentation varies from 45° (acute angle to the direction of extension) to 135° (obtuse angle to the extension direction) for the different setups based on the positions of the faults with respect to each other (Figure 1.6).

Photographs of the top and two sides of the clay model are taken at incremental steps throughout the length of the experiment. The analysis on fault orientations, densities and connectivity are conducted on the top photographs whereas the profile views are used to study the development and propagation of the master fault and secondary antithetic and synthetic faults. Each photograph is geo-rectified with reference to four known points on the deformation table in order to transform the photographs to correct scale and

minimize distortion. Fault traces are digitized manually in ArcView GIS (Environmental Systems and Research Institute, Redlands, CA) at finite stages of the experiment in order to demonstrate the evolution and change in fault characteristics.

1.2.2 Laser Scanning Methodology

The technology of scanning surfaces by a laser scanner and developing virtual three dimensional models has been in use in numerous industries, particularly reverse engineering and 3D animation. The same technology is applied here to scan the surfaces of the clay experiment in order to gather 3D information and thereby generate a virtual surface which can be used to visualize the development of the structure in much greater detail and to generate contour maps of surfaces.

The 3D scanner uses four sets of Class 1M, 10mW solid state line lasers and two sets of 3.0 Megapixel CMOS image sensors built into the instrument. The two sensors switch during the use of the scanner in macro or wide mode. The scanning size is 13.5 inches by 10.1 inches with a horizontal and vertical resolution of 75 DPI (~0.015 inches point density). The scanner is placed face down, approximately 15 inches vertically above the clay cake and top surfaces are scanned at equal increments of displacement.

The laser beam swipes across the clay surface at a constant velocity and the sensor continuously captures the light reflected from the clay surface. The coordinates of the points are computed by the scanner using the triangulation method (Figure 1.7). The known parameters are the angle α at which the laser projects its beam on the surface, the angle β at which the sensor collects the laser beam (β is known if the focal length and the pixel size of the sensor are given) and the triangulation distance between the sensor and

laser source (Petrov et al., 1998). Since all the geometric parameters are known, the coordinates x, y and z on the surface are calculated using trigonometric methods. The laser source produces a line, and all the coordinates x, y and z along that line are collected at the same time. Moreover, twin arrays of four laser beams are used as source in this instrument for cross validating each data point by measuring it at least twice. The origin or reference coordinate system is determined automatically during each run by the first point scanned on the surface. It therefore becomes necessary not to move the scanner during the experiment in order to spatially position the scanned surfaces in the same reference coordinate system. The scanned data are exported as point files into 3D modeling software GoCAD from Paradigm, where surfaces can be built from the point cloud.

1.3 Fault Evolution in Cross Section

Profile views of the structural evolution are essentially similar in all six experiments; therefore, observations from only one experiment will be discussed in this section. With the onset of displacement, faults begin to form at the contact between the overlying and underlying plates forming a saddle or symmetrical graben centered above the contact (Figure 1.8). The graben is bounded on either side by a set of primary synthetic faults (PS) and a conjugate set of antithetic faults (PA), both initiating at the basal contact of the plates. The PS faults are tied to the overlying base plates whereas the PA faults are associated to the underlying plate. The movement on the primary faults is accommodated by sets of secondary synthetic (SS) and antithetic (SA) faults that form along the primary sets. The primary faults initiate from the base to the top as en-echelon

discrete segments that curve upward towards the top free surface (Vendeville and Cobbold, 1988; Bose and Mitra, 2009). The main synthetic fault forms by linkage of these discrete segments present in the overlying plate (Figure 1.9). Once the master synthetic fault has formed, most of the displacement is accommodated along this fault. The antithetic faults, on the other hand, form a broad zone as the slip is progressively transferred from the older to newer faults (Figure 1.8b). This wide width of the antithetic faults is principally caused by the drop down of the hanging wall being attached to the base plate as well as to the footwall block.With progressive evolution, the final geometry of the structure changes from a symmetrical graben to an asymmetrical half-graben.

1.4 Divergent Transfer Zones

1.4.1 3-D Structural Geometry and Evolution

Laser-scan models of a divergent transfer zone with normal offset of the main fault are described in this section to illustrate the different stages of evolution of the main faults, the secondary faults and rollover structures. The master faults dipping in the direction of extension are termed regional faults and those dipping in the opposite direction are termed counter-regional faults. The structures initiate as two symmetrical grabens, offset along a transfer zone (Figure 1.10 a). The two master faults do not form simultaneously and there is a distinct lag between the formation of the regional (R) and the counter-regional (CR) faults (Figure 1.10b). Because of the earlier formation of the regional fault (R), the synthetic fault zone associated with it is narrower than the antithetic fault zone. On the other hand, the counter-regional master fault (CR) forms at a later stage, which results in a broader synthetic fault zone and a narrower antithetic zone

(Figure 1.10 c and d). The difference in time of formation of the two faults also results in larger displacement along the regional master fault (Figure 1.10c-d).

Rollover folds form in the hanging wall blocks adjacent to both the regional and counter-regional faults, with the front limb of each rollover progressively stepping down along a series of antithetic faults (Figure 1.10 c and d). A structural high develops towards the center of the transfer zone where the slips from both the master faults decrease (Figure 1.10d). The progressive formation of structural highs can be studied by gridding and contouring the elevation of the top surface (Figure 1.11 a-d). The most prominent structural highs form in the footwall zones of the two major faults, and curve into the crestal area of the rollover associated with the adjacent faults (Figure 1.11 b-d). The structural high is more prominent in the footwall of the regional fault because of the initial regional dip in the model. However, because of the low relief of most rollover structures, the locations of the structural highs are also strongly controlled by the initial relief of the surface. In the case of this particular experiment, there is a small initial dip towards the bottom left (Figure 1.11a), and this results in the highest regions being located to the top right of the model.

The formation of asymmetric half-grabens of opposite polarity on either side of the transfer zone is illustrated by three profiles (Figure 1.12a) across the divergent model. The figures show the intersection of the clay surfaces and the different profiles after significant displacement. The lines along the profiles indicate these intersections at progressive stages of the experiment. Profile AA' in Figure 1.12b contains the well-defined regional fault where most of the displacement is accommodated by the single fault and the maximum relief between the original clay surface and final surface is 23.6

mm. Profile CC’ illustrates the later developed counter-regional fault formed by the linkage of several smaller faults, although the final relief is close to that in Profile A (23.5 mm). The transfer zone is contained in Profile BB’, which in spite of the local low relief, is still higher (relief of 9.8 mm) than the adjoining half-grabens.

1.4.2 Fault Orientations

The orientations of the secondary faults are generally perpendicular to the extensional direction along the two master faults, except within the transfer zone. The synthetic faults remain consistent in orientation through all the experiments, but the antithetic faults tend to curve in towards the center of the transfer zone (Figure 1.13). The amount of curvature, measured with respect a vertical line perpendicular to the direction of extension, of the antithetic faults varies with the experimental setup, viz. Approaching, Normal Offset and Overlapping, and with total displacement. Figure 1.13 d-e illustrates the change in average orientation of antithetic and synthetic faults with displacement in the three experimental setups. The change in orientation is least for synthetic faults and remains between -1° to 8°. The maximum change for the antithetic faults is observed in the Normal Offset setup and the least in the Approaching setup. The antithetic faults in the Normal Offset configuration show a drastic increase in orientation in the initial stage but remain constant at about 35° after a certain displacement. The Approaching setup shows a constant decrease in orientation due to the formation of new faults at higher angles to the extension direction, whereas the Overlapping setup displays a continuous increase in orientation.

1.4.3 Fault Density and Connectivity

Fault densities were determined in ArcGIS (Environmental Systems and Research Institute, Redlands, CA) by calculating the sum of the total lengths of faults within an area of a circle of unit radius (1 cm). Figure 1.14 displays the variation of density through progressive stages of displacement in the Normal Offset setup. The initial stage displays most of the dense zones developing adjacent to the master faults with few faults developing within the transfer zone. With increasing displacement, faults tend to develop within the transfer zone both by lateral linkage and new fault growth. The secondary synthetic and antithetic faults associated with the master faults continue to form throughout the experiment.

Connectivity between faults is examined using cluster analysis, a concept based on percolation theory (Stauffer, 1985; Bebbington et al., 1990; Berkowitz, 1995). A connectivity cluster can be defined as a single connected network of faults that have been identified as convex hulls around connected faults within ArcView GIS. This analysis has been successfully applied for analyzing connectivity of rock fractures (Ghosh and Mitra, 2009) and provides important information on fluid flow pathways. Application of cluster analysis to clay experimental models illustrates the linkage patterns of the faults, the evolution and distribution of these clusters in both time and space (Bose and Mitra, 2009). Figure 1.15 displays the distribution of connected clusters (shaded areas) at different stages of displacement during the Normal Offset experiment. In the initial stage, small clusters develop in the secondary faults and with increasing displacement, the sizes of the clusters increase. In the later stages of displacement, most of the clusters are elongate and are present within the synthetic fault zone, both along the main faults as

well as in the transfer zone. Figure 1.16 shows the distribution of the clusters in the final stage of the Approaching and Overlapping experiments. For all of the setups, the synthetic fault sets tend to develop connectivity far more easily than antithetic sets, which remain isolated not only from each other but also from the synthetic sets. In the Approaching scenario, the size of the final cluster is much larger than that in the other setups. This is due to the fact that both antithetic and synthetic sets are very well connected due to the low angles between fault sets within the transfer zone.

1.5 Convergent Transfer Zones

1.5.1 3-D Structural Geometry and Evolution

The structures along a convergent transfer zone with normal offset initiate as two symmetric grabens separated by a transfer zone (Figure 1.17 a). The regional master fault forms earlier than the counter-regional fault, resulting in a narrower synthetic fault zone (Figure 1.17b). Rollover folds form in the hanging wall blocks adjacent to both the regional and counter-regional faults, with the front limb of each rollover progressively stepping down along a series of antithetic faults and the formation of asymmetric grabens (Figure 1.17 c and d). One of the major differences with the Divergent experiment is that initially the two grabens here are separated by a structural high, but with continuing deformation, the two grabens merge into a single low, although they remain structurally high compared to the adjacent grabens.

Structural highs and potential closures form in the footwall zones of the two major faults and curve into the crestal area of the rollover associated with the adjacent faults (Figure 1.18 a-d). The structural high is more prominent in the footwall of the

regional fault because of the initial regional dip in the model. A low relief closure also forms within the transfer zone from the interference of the two rollover structures.

Three profiles across the convergent transfer zone illustrate the asymmetry of the grabens in the transfer zone (Figure 1.19a). Profiles AA' and CC' in Figure 1.19b, shows a distinct difference in relief due to the lag between the formation of the regional and counter-regional faults. Profile AA', containing the counter-regional fault (CR) shows a maximum relief of 24.1 mm whereas Profile CC', containing the regional fault (R) shows a relief of 27.1 mm. Profile BB' through the middle of the transfer zone displays a maximum relief of 13.5 mm, which is greater than the equivalent profile in the Divergent zone in Figure 1.12. The models illustrate that a Convergent transfer zone creates a Low Relief Accommodation Zone (LRAZ) while a Divergent transfer zone forms a High Relief Accommodation Zone (HRAZ) (Morley et al., 1990; Rosendahl, 1987).

1.5.2 Fault Orientations

The orientations of the faults in the Convergent transfer zone experiments are also generally perpendicular to the direction of extension adjacent to the main faults. The antithetic faults remain constant in orientation for all of the three setups and remain at an average orientation of -0.5°. The synthetic faults, on the other hand, curve towards the center of the transfer zone (Figure 1.20). The orientations of the antithetic faults vary little (between -2° to 1.5°). The maximum change in orientation of synthetic faults is in the Overlapping setup, where it continuously increases from 5° to 24° (Figure 1.20 d-e). For the Normal Offset setup, the synthetic faults change from 10° to 20° and remain

consistent thereafter, while the synthetic faults in the Approaching setup change very little in orientation.

1.5.3 Fault Density and Connectivity

The development of density patterns in the Normal Offset experiment is illustrated in Figure 1.21. The densities evolve initially as isolated elongated zones adjacent to the master faults with little or no faulting in the transfer zone. With increasing displacement, the dense zones grow in size and connect through the entire transfer zone. The density maps of this experiment also display the formation of fault zones of similar widths, growing into much wider antithetic fault zones as compared to the narrower synthetic zones. The maximum density is observed where the synthetic faults of the regional fault interact with the antithetic faults of the counter-regional system.

Figure 1.22 displays the evolution of connectivity clusters in the Normal Offset experiment. The clusters initially develop along the master faults and increase in size with total displacement. In the final stage, clusters are largest in size along the antithetic faults and in the areas where the synthetic faults associated with the regional master fault connect with the antithetics of the counter-regional fault. This phenomenon is also observed for the Overlapping experiment (Figure 1.23). The cluster distribution for the Approaching setup is again different from the other setups and the sizes are also much larger (Figure 1.23). This can be attributed to the low angle of curvature of the secondary faults at the transfer zone and the secondary fault pattern developed in this setup.

1.6 Discussion and Conclusions

Analog clay experiments provide important insights for understanding the evolution of secondary faults and structural variations associated with divergent and convergent transfer zones in listric normal fault systems. Laser scanning technology applied to clay modeling enables the visualization and quantitative analysis of progressive changes in structural geometry for the different experimental setups. The relative changes in relief can not only be compared from one stage to the other but also for different experimental setups. Contour and relief maps and models provide information on the general trend and evolution of structural highs and therefore enable an analysis on the development of hydrocarbon traps and possible fluid accumulation in these areas.

Table 1.1 summarizes the observations for the fault pattern, density and connectivity for the different experimental setups. The fault patterns in the different experiments vary with the base plate configuration, and change with progressive displacement throughout an experiment. The synthetic faults in Divergent and antithetic faults in Convergent transfer zone remain consistent in orientation throughout the experiments, whereas the antithetic faults in the Divergent and synthetic faults in the Convergent transfer zones curve towards the center of the transfer zones. For the Normal Offset setup for both Divergent and Convergent experiments, the bending increases initially but remains constant after a certain amount of e. For the Overlapping setups, the faults continue to increase in orientation with increasing displacement. These fault patterns are helpful in predicting orientation of minor faults in nature that may be undetected by well data or may lie below the seismic resolution.

The distribution of density and connectivity clusters are important in identifying locations of intense faulting, possible fluid migration pathways and degree of compartmentalization in such structural settings. The synthetic faults in Divergent and antithetic faults in Convergent transfer zones connect with increasing displacement, and conversely, the antithetic faults in Divergent and synthetic faults in Convergent transfer zones remain separated from each other. There is also a tendency for the synthetic sets related to the regional fault in Convergent transfer zones to interact and connect with the antithetic sets of the counter-regional fault. Approaching setup for both types of transfer zones, the synthetic and antithetic fault sets have similar strikes. Therefore, with increasing displacement, as they propagate along strike, they are more likely to connect and result in larger connecting clusters. These experimental results are useful in predicting structural features and secondary fault patterns in passive margin settings such as the Gulf of Mexico, which contain abundant examples of various types of transfer zones.

References

Bausfield, J., 1983, Delta Farms: Lafourche and Jefferson Parishes, Louisiana, in McCormick, L. L. and R. S. Kline, eds., Oil and gas fields of Southeast Louisiana: The New Orleans Geological Society Publication 3, p. 18-18F.

Bebbington, M., D. Vere-Jones, and X. Zheng, 1990, Percolation theory: A model for rock fracture?: Geophysical Journal International, v. 100, p. 215–220.

Berkowitz, B., 1995, Analysis of fracture network connectivity using percolation theory: Mathematical Geology, v. 27, p. 467–483.

Bose, S., and S. Mitra, 2009, Deformation along oblique and lateral ramps in listric normal faults: Insights from experimental models: American Association of Petroleum Geologists Bulletin, v. 93, p. 431-451.

Childs, C., J. Watterson, and J. J. Walsh, 1995, Fault overlap zones within developing normal fault systems: Journal of the Geological Society of London, v. 152, p. 535-549.

Cloos, E., 1968, Experimental analysis of Gulf Coast fracture patterns: American Association of Petroleum Geologists Bulletin, v. 52, p. 420-444.

Conatser, W., 1983, Lake Hatch Field: Terrebonne Parish, Louisiana, in L. L. McCormick and R. S. Kline, eds., Oil and gas fields of Southeast Louisiana: The New Orleans Geological Society Publication 3, p. 24-24E.

Crider, J. G., 2001, Oblique slip and the geometry of normal-fault Linkage: mechanics and a case study from the Basin and Range in Oregon: Journal of Structural Geology, v. 23, p. 1997-2009.

Diegel, F. A., J. F. Karlo, D. C.Schuster, R. C. Shoup, and P. R. Tauvers, 1995, Cenozoic structural evolution and tectono-stratigraphic framework of the northern Gulf Coast continental margin, in M. P. A. Jackson, D. G. Roberts, and S. Snelson, eds., Salt tectonics: A global perspective: American Association of Petroleum Geologists Memoir 65, p. 109–151.

Faulds, J. E., and R. J. Varga, 1998, The role of accommodation zones and transfer zones in the regional segmentation of extended terranes, in J. E. Faulds, and J. H. Stewart, eds., Accommodation zones and transfer zones: The regional segmentation of the Basin and Range province: Geological Society of America Special Paper 323, p. 1-45.

Ghosh, K and S. Mitra, 2009, Structural controls of fracture orientations, intensity, and connectivity, Teton Anticline, Sawtooth Range, Montana: American Association of Petroleum Geologists Bulletin, v. 93, p. 995-1014.

Hildebrand-Mittlefehldt, N., 1979, Deformation near a fault termination, part I: A fault in a clay experiment: Tectonophysics, v. 57, p. 131-150.

Hubbert, M. K., 1937, Theory of scale models as applied to the study of geologic structures: Geological Society of America Bulletin, v. 48, p. 1459-1520.

Le Calvez, J. H. and B. C. Vendeville, 2002, Physical modeling of normal faults and graben relays above salt: A qualitative and quantitative analysis: Transactions of the Gulf Coast Association of Geological Societies, v. 52, p. 599-606.

McBride, B. C., M. G. Rowan, and P. Weimer, 1998, The evolution of allochthonous salt systems, Northern Green Canyon and Ewing Bank (offshore Louisiana), Northern

Gulf of Mexico: American Association of Petroleum Geologists Bulletin, v. 82, p. 1013-1036.

McClay, K. R., 1989, Physical models of structural styles during extension, in A. J. Tankard and H. R. Balkwill eds., Extensional tectonics and stratigraphy of the North Atlantic margins: American Association of Petroleum Geologists Memoir 46, p. 95-110.

Morgan, A. L., 1953, Structural analysis of Delta Farms Field, Lafourche Parish, Louisiana: American Association of Petroleum Geologists Bulletin, v. 37, p. 2649-2676.

Morley, C. K., R.A. Nelson, T. L. Patton and S. G. Munn, 1990, Transfer zones in the East African rift system and their relevance to hydrocarbon exploration in rifts: American Association of Petroleum Geologists Bulletin, v. 74, p. 1234-1253.

Moustafa, A. R., 2002, Controls on the geometry of transfer zones in the Suez rift and Northwest Red Sea: Implications for the structural geometry of rift systems: American Association of Petroleum Geologists Bulletin, v. 86, p. 979-1002.

Oertel, G., 1965, The mechanism of faulting in clay experiments: Tectonophysics, v. 2, p. 343-393.

Peacock, D. C. P and D. J. Sanderson, 1991, Displacements, segment linkage and relay ramps in normal fault zones: Journal of Structural Geology, v. 13, p. 721-733.

Petrov, M., A. Talapov, T. Robertson, A. Lebedev, A. Zhilyaev and L. Polonskiy, 1998, Optical 3D digitizers: Bringing life to the virtual world: IEEE Computer Graphics and Applications, v. 18, p. 28-37.

Reches, Z., 1988, Evolution of fault patterns in clay experiments: Tectonophysics, v. 145, p. 141-156.

Rosendahl, B. R., 1987, Architecture of continental rifts with special reference to East Africa: Annual Reviews of Earth and Planetary Science, v. 15, p. 445-503.

Rowan, M. G., M. P. A. Jackson and B. D. Trudgill, 1999, Salt-related fault families and fault welds in the Northern Gulf of Mexico: American Association of Petroleum Geologists Bulletin, v. 83, p. 1454-1484.

Rowan, M. G., 1995, Structural styles and evolution of allochthonous salt, central Louisiana outer shelf and upper slope, in M. P. A. Jackson, D. G. Roberts, and S. Snelson, eds., Salt tectonics: A global perspective: American Association of Petroleum Geologists Memoir 65, p. 199-228.

Rowan, M. G., P. Weimer and P. B. Flemings, 1994, Three-dimensional geometry and evolution of a composite, multilevel salt system, Western Eugene Island, offshore Louisiana: Transactions of the Gulf Coast Association of Geological Societies, v. 44, p. 641-648.

Rutter, E.H., 1986. On the nomenclature of mode of failure transition in rocks: Tectonophysics, v. 122, p. 381–387.

Serra, S., and R. A. Nelson, 1988, Clay modeling of rift asymmetry and associated structures: Tectonophysics, v. 153, p. 307–312,

Stauffer, D., 1985, Introduction to percolation theory: London, Taylor & Francis, 190 p.

Trudgill, B. D and J. Cartwright, 1994, Relay-ramp forms and normal-fault linkages, Canyonlands National Park, Utah: Geological Society of America Bulletin, v. 106, p. 1143-1157.

Vendeville, B. and P. R. Cobbold, 1988, How normal faulting and sedimentation interact to produce listric fault profiles and stratigraphic wedges: Journal of Structural Geology, v. 10, p. 649-659.

Withjack, M. O., R. W. Schlische and A. A. Henza, 2007, Scaled experimental models of extension: Dry sand vs. wet clay: Houston Geological Society Bulletin, v. 49, p. 31-49.

Worrall, D. M. and M. Snelson, 1989, Evolution of the Northern Gulf of Mexico, with emphasis on Cenozoic growth faulting and the role of salt, in A. W. Bally and A. R. Palmer, eds., The geology of North America; An overview: Geological Society of America Decade of North American Geology, v. A, p. 97–138.

Younes, A. I. and K. McClay, 2002, Development of accommodation zones in the Gulf of Suez-Red Sea rift, Egypt: American Association of Petroleum Geologists Bulletin, v. 86, p. 1003-1026.

Figure Captions

Figure 1.1. Differences in the geometry of transfer zones associated with (a) Planar normal faults and (b) Listric normal faults.

Figure 1.2. Types of Divergent and Convergent transfer zones in listric fault systems: (a) Approaching, with the two faults approaching each other and separated by a gap, (b) Normal Offset, with the two faults showing a 90 degree offset and (c) Overlapping, with an overlapping zone between the two faults.

Figure 1.3. Location map of West Delta and Delta Farms fields and the Lake Hatch field in offshore Louisiana in the Northern Gulf of Mexico.

Figure 1.4. Subsurface structure maps of (a) 6700 Sand and (b) Textularia Stapperi horizon in the West Delta and Delta Farms field, offshore Louisiana. (c) A well log section running North-South through the middle of the field, marked in (a), showing the structure and stratigraphic position of the two mapped horizons (modified from Bausfield, 1983). The oil-water contact is marked as the shaded region in the maps.

Figure 1.5. Subsurface structure maps of (a) 7800 Sand and (b) 9800 Sand in the Lake Hatch field, offshore Louisiana. (c) A well log section running approximately Northeast-Southwest through the middle of the field showing the structure and stratigraphic position of the two mapped horizons (modified from Conatser, 1983). The oil-water contact is marked as shaded region in the maps.

Figure 1.6. Experimental setups for the modeling of Divergent and Convergent transfer zones. Three setups were constructed for each of the transfer zone types to model (a & b) Approaching faults, (c & d) Normal Offset faults and (e & f) Overlapping faults, for a total of six experiments. Arrows indicate the direction of extension and the dip directions

of the master faults formed are shown on the base plates. The curved arrows indicate the portions of the plates that have been overlain by the opposite plate.

Figure 1.7. (a) Schematic diagram of the working principle of the laser scanner with the triangulation formed by the laser source, the detector and the point on the clay surface where the laser is reflected from. In three dimensions, the point on the surface would be a line. (b) Schematic view of the laser scanner projecting a line laser and sweeping across the clay surface at a constant velocity. (c) Coordinates of points collected during scanning can be exported as XYZ point cloud and can be visualized in a 3D modeling software (GoCAD). (d) Final virtual surface of the clay recreated from the point cloud.

Figure 1.8. Profile of clay models showing two stages of development from a symmetrical graben (a) to an asymmetrical half-graben (b). Primary synthetic, primary antithetic, secondary synthetic and secondary antithetic faults are denoted as PS, PA, SS and SA respectively.

Figure 1.9. Profiles of clay models showing the development of a master fault by coalescence of a number of fault segments. After the master fault is formed, most of the displacement is accommodated by it.

Figure 1.10. Laser-scanned three-dimensional model showing the evolution of the structure in a Divergent Normal Offset transfer zone, and the formation of the regional (R) and counter-regional (CR) faults.

Figure 1.11. Structure contours (in millimeters) obtained from laser-scanned models showing the evolution of structural highs and lows in a divergent transfer zone.

Figure 1.12.a. Location of three profile sections through a Divergent transfer zone. (b) Profiles AA', BB' and CC' showing the maximum reliefs along the main faults and within the transfer zones.

Figure 1.13. Fault patterns and orientations in the final stages of Divergent setups of (a) Approaching, (b) Normal Offset and (c) Overlapping faults. (d-e) Changes in orientations of synthetic and antithetic faults in a divergent transfer zone.

Figure 1.14. Density maps at different stages of displacement in the Divergent Normal Offset experiment. (a) 1.04 cm, (b) 2.1 cm and (c) 3.24 cm displacement. Density units are in cm/sq. cm.

Figure 1.15. Connectivity clusters at stages of increasing displacement in the Divergent Normal Offset setup. (a) 1.04 cm, (b) 2.1 cm and (c) 3.24 cm displacement.

Figure 16. Connectivity clusters at the final stages of Divergent (a) Overlapping setup and (b) Approaching setup.

Figure 1.17. Laser-scanned three-dimensional model showing the evolution of the structure in a Convergent Normal Offset transfer zone, and the formation of the regional (R) and counter-regional (CR) faults.

Figure 1.18. Structure contours (in millimeters) showing the evolution of structural highs and lows in a convergent transfer zone.

Figure 1.19.a. Location of three profile sections through a Convergent transfer zone. (b) Profiles AA', BB' and CC' showing the maximum reliefs along the main faults and within the transfer zones.

Figure 1.20. Fault patterns and orientations in the final stages of Convergent transfer zone with (a) Approaching, (b) Normal Offset and (c) Overlapping faults. (d-e) Changes in orientations of synthetic and antithetic faults in a convergent transfer zone.

Figure 1.21. Density maps at different stages of displacement in a Convergent Normal Offset experiment. (a) 1.09 cm, (b) 2.14 cm and (c) 3.61 cm displacement. Density units are in cm/sq. cm.

Figure 1.22. Connectivity clusters at stages of increasing displacement in the Convergent Normal Offset setup. (a) 1.09 cm, (b) 2.14 cm and (c) 3.61 cm displacement.

Figure 1.23. Connectivity clusters at the final stages of Convergent (a) Overlapping setup and (b) Approaching setup.

Table 1.1: Summary of observations of fault pattern, density and connectivity for the six experimental setups of Divergent and Convergent transfer zones.

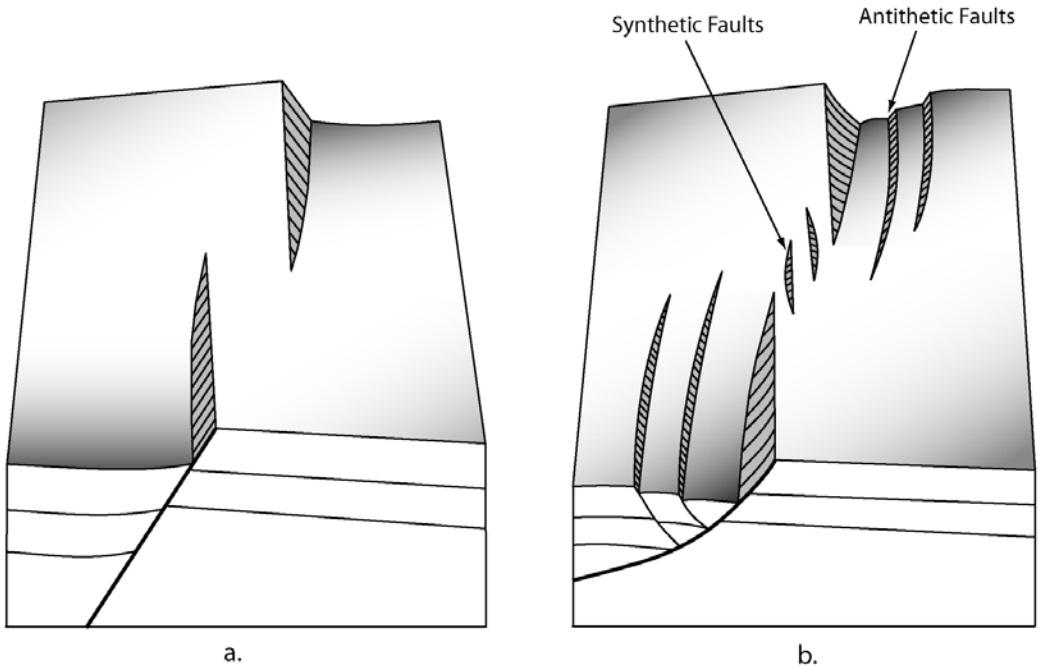

Figure 1.1: Differences in the geometry of transfer zones associated with (a) Planar normal faults and (b) Listric normal faults.

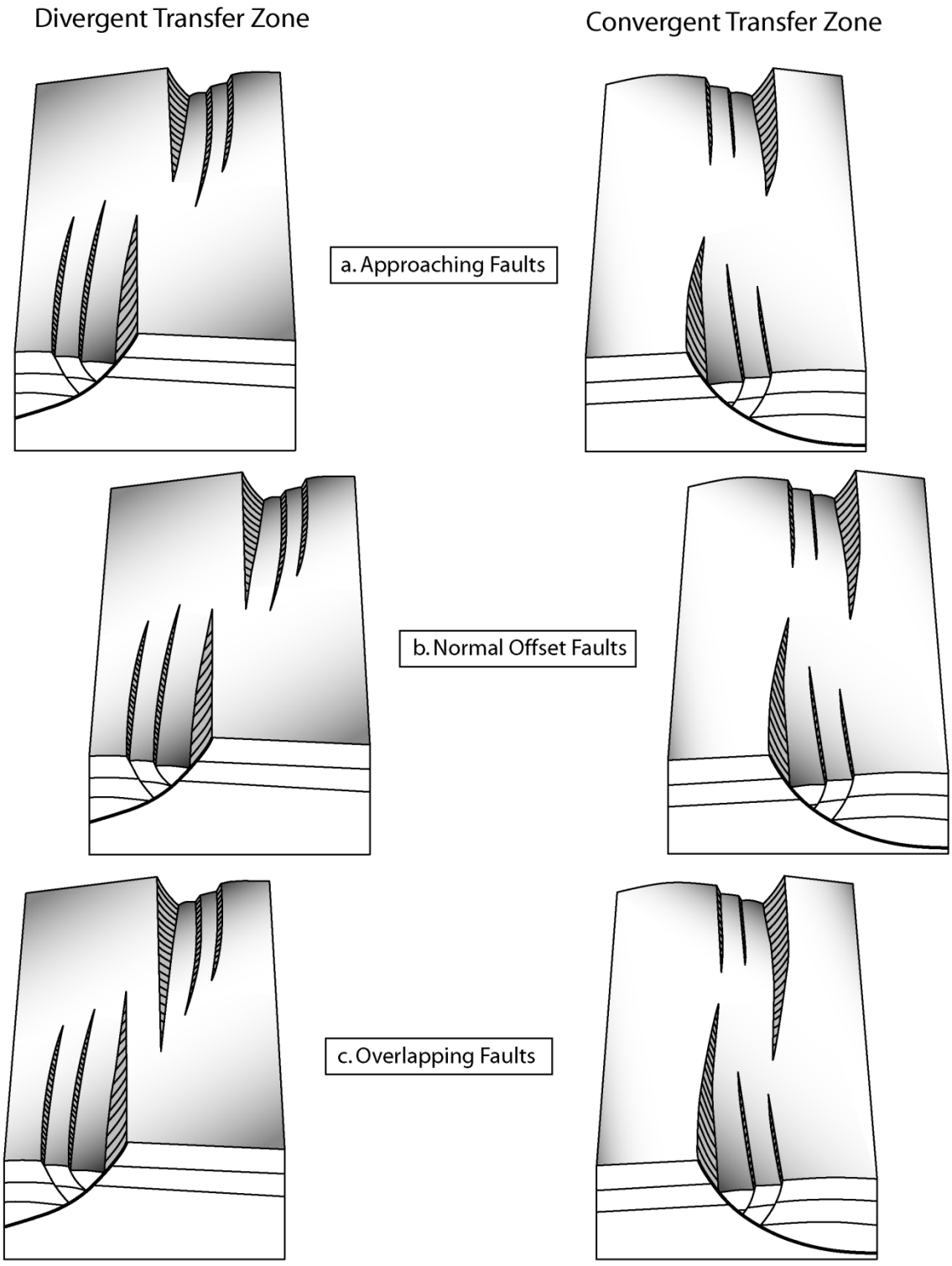

Figure 1.2: Types of Divergent and Convergent transfer zones in listric fault systems: (a) Approaching, with the two faults approaching each other and separated by a gap, (b) Normal Offset, with the two faults showing a 90 degree offset and (c) Overlapping, with an overlapping zone between the two faults.

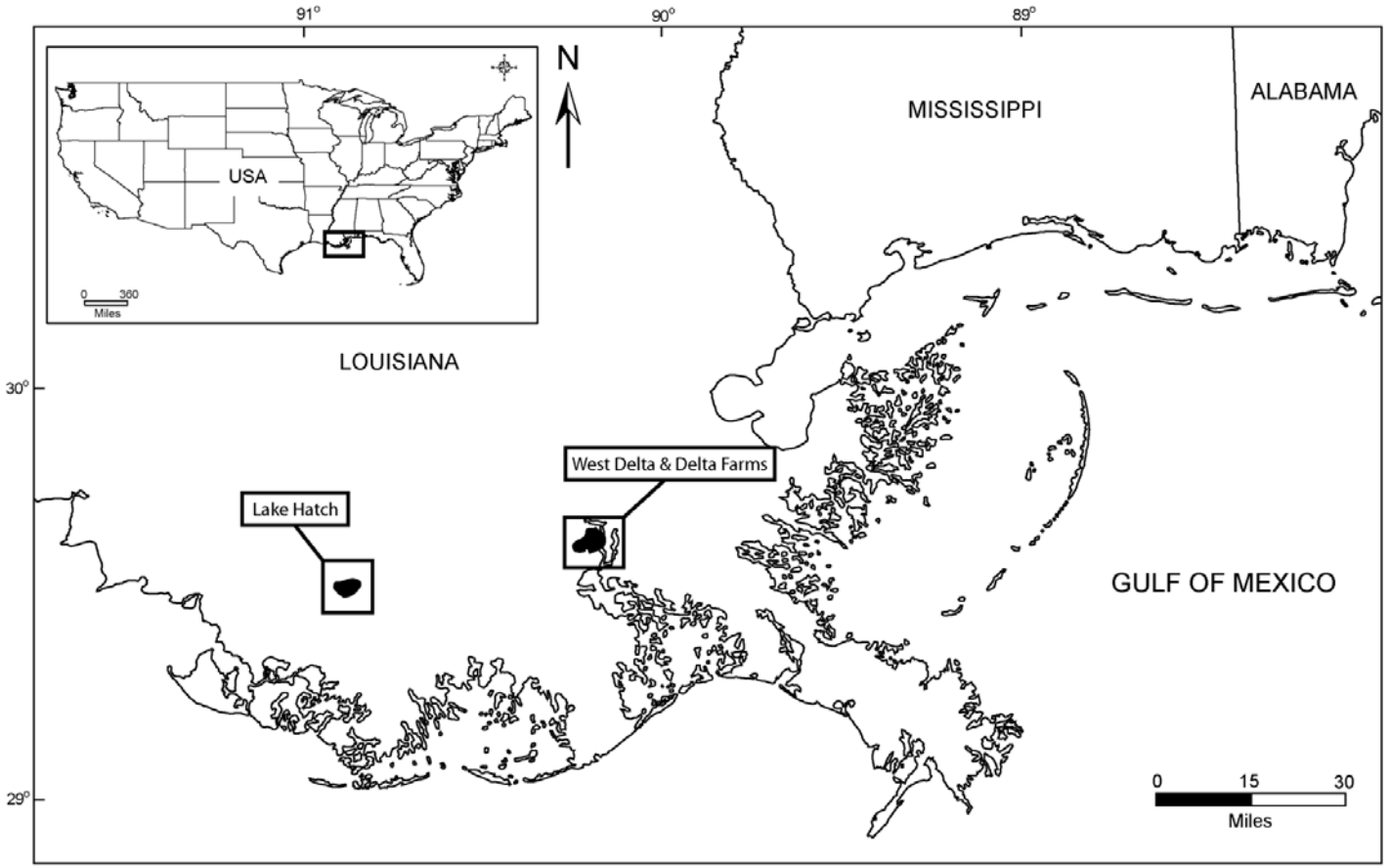

Figure 1.3: Location map of West Delta and Delta Farms fields and the Lake Hatch field in offshore Louisiana in the Northern Gulf of Mexico.

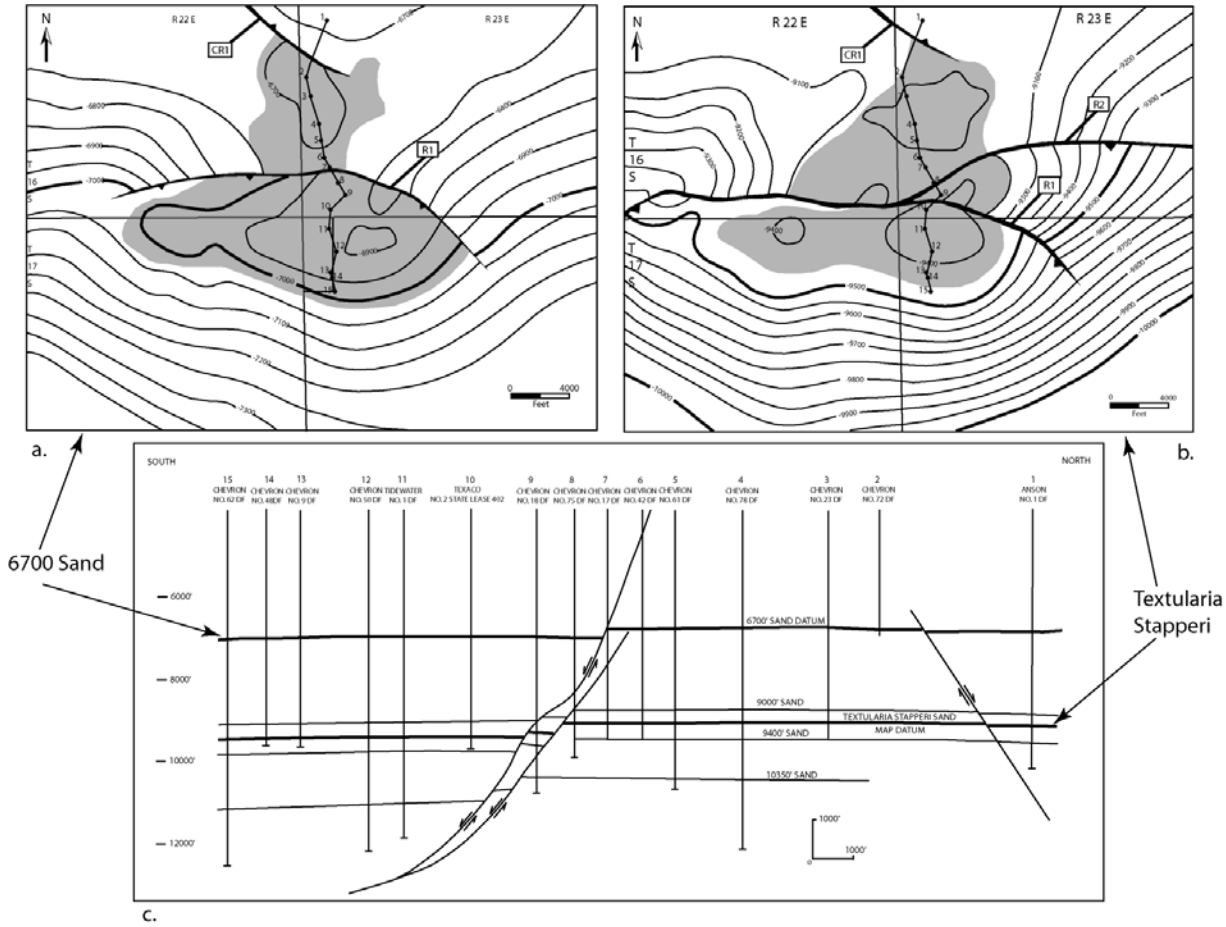

Figure 1.4: Subsurface structure maps of (a) 6700 Sand and (b) Textularia Stapperi horizon in the West Delta and Delta Farms field, offshore Louisiana. (c) A well log section running North-South through the middle of the field, marked in (a), showing the structure and stratigraphic position of the two mapped horizons (modified from Bausfield, 1983). The oil-water contact is marked as the shaded region in the maps.

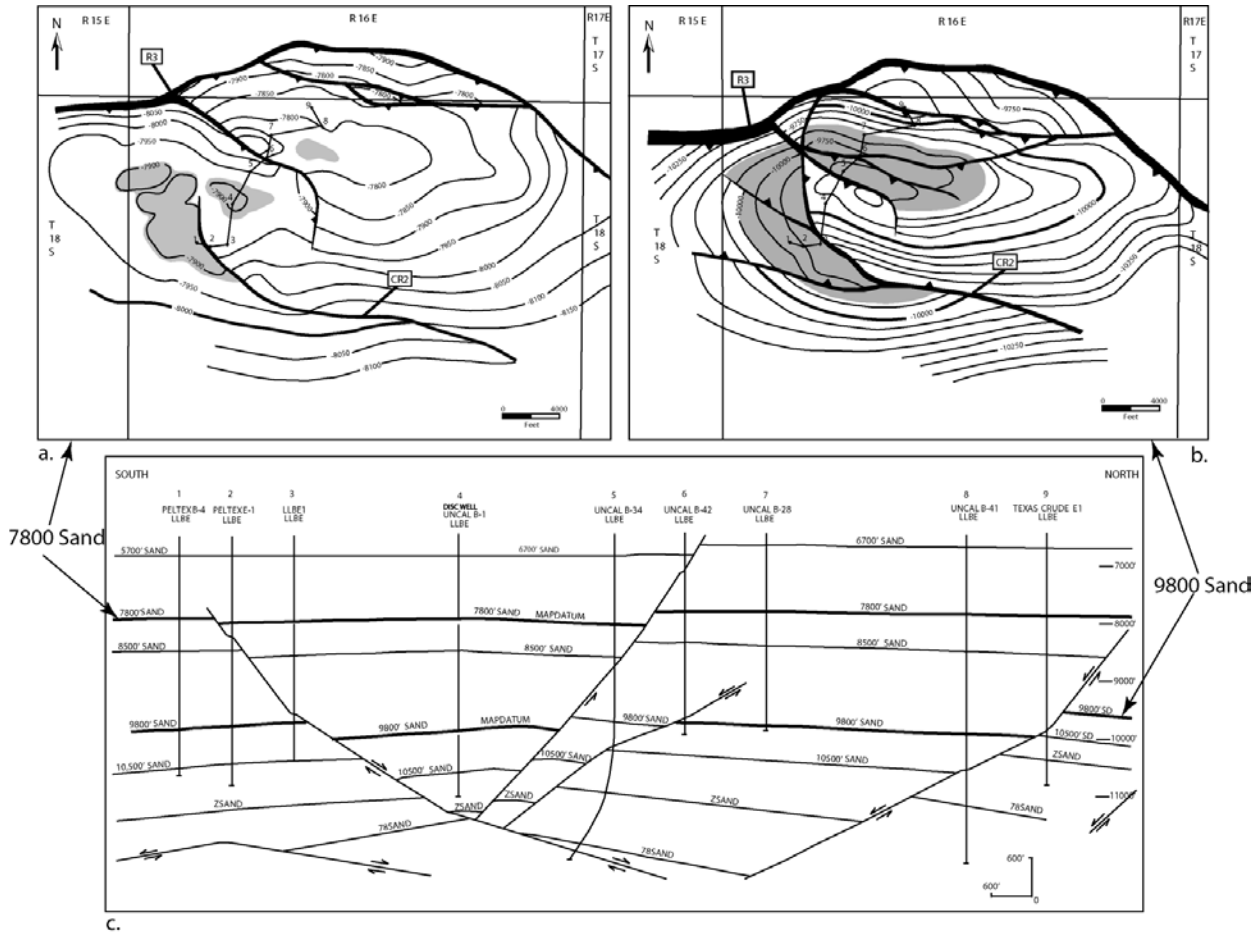

Figure 1.5: Subsurface structure maps of (a) 7800 Sand and (b) 9800 Sand in the Lake Hatch field, offshore Louisiana. (c) A well log section running approximately Northeast-Southwest through the middle of the field showing the structure and stratigraphic position of the two mapped horizons (modified from Conatser, 1983). The oil-water contact is marked as shaded region in the maps.

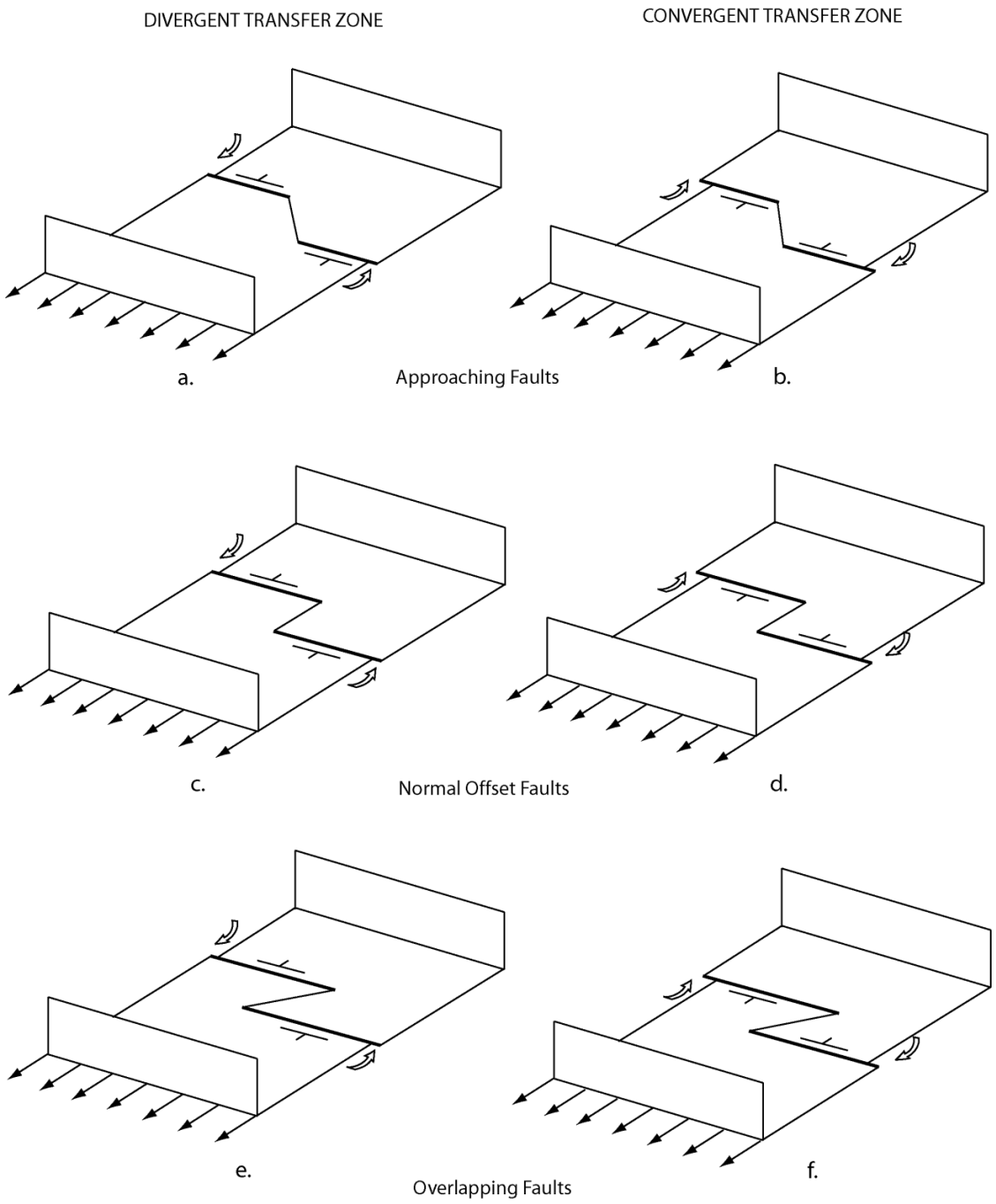

Figure 1.6: Experimental setups for the modeling of Divergent and Convergent transfer zones. Three setups were constructed for each of the transfer zone types to model (a & b) Approaching faults, (c & d) Normal Offset faults and (e & f) Overlapping faults, for a total of six experiments. Arrows indicate the direction of extension and the dip directions of the master faults formed are shown on the base plates. The curved arrows indicate the portions of the plates that have been overlain by the opposite plate.

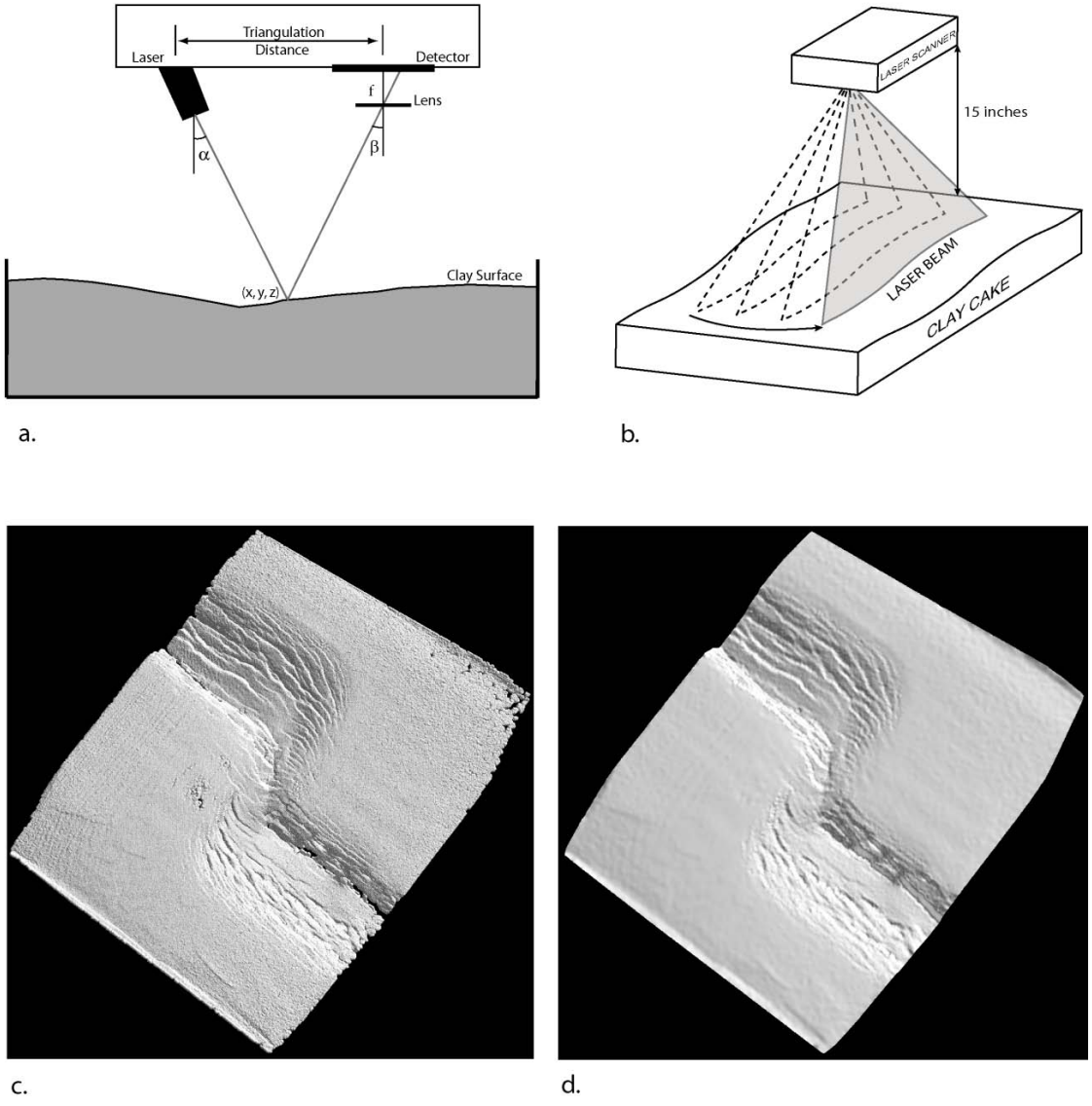

Figure 1.7: (a) Schematic diagram of the working principle of the laser scanner with the triangulation formed by the laser source, the detector and the point on the clay surface where the laser is reflected from. In three dimensions, the point on the surface would be a line. (b) Schematic view of the laser scanner projecting a line laser and sweeping across the clay surface at a constant velocity. (c) Coordinates of points collected during scanning can be exported as XYZ point cloud and can be visualized in a 3D modeling software (GoCAD). (d) Final virtual surface of the clay recreated from the point cloud.

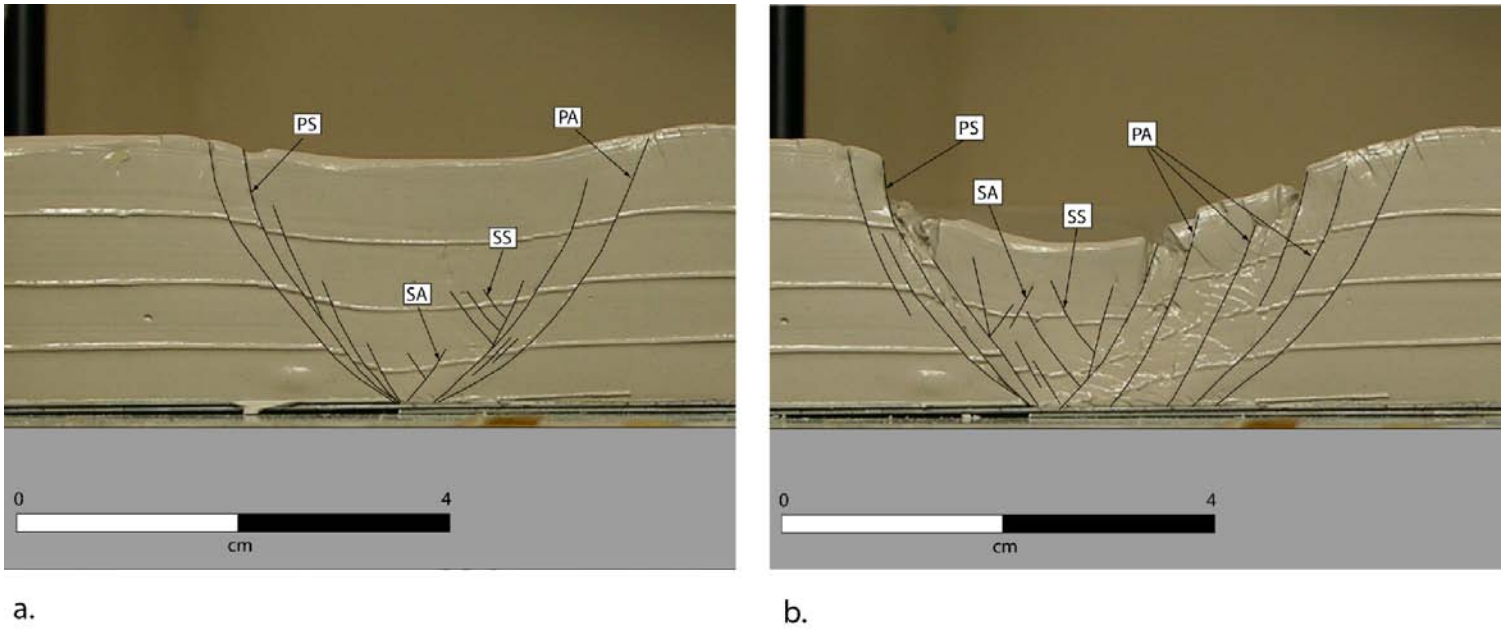

Figure 1.8: Profile of clay models showing two stages of development from a symmetrical graben (a) to an asymmetrical half-graben (b). Primary synthetic, primary antithetic, secondary synthetic and secondary antithetic faults are denoted as PS, PA, SS and SA respectively.

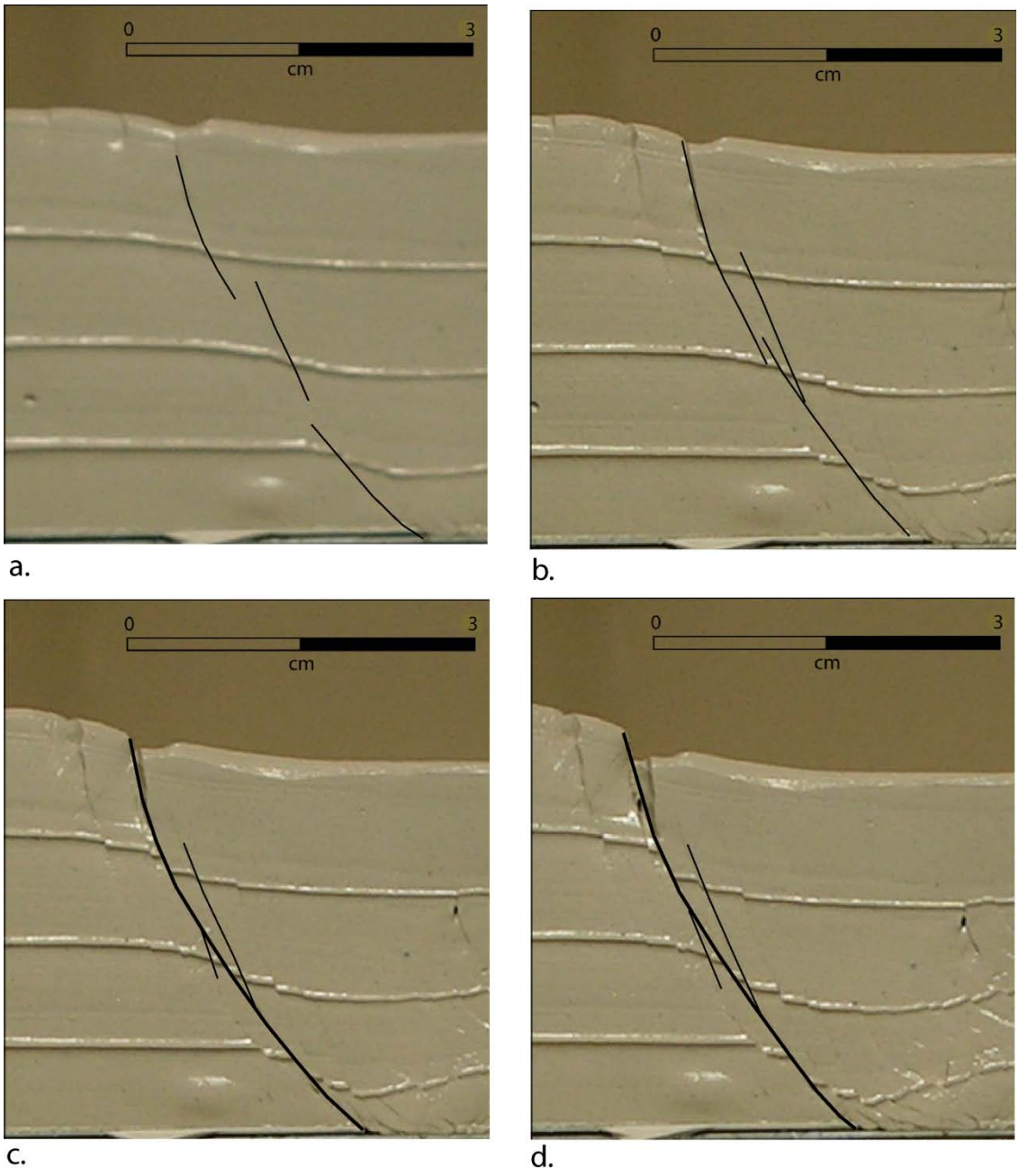

Figure 1.9: Profiles of clay models showing the development of a master fault by coalescence of a number of fault segments. After the master fault is formed, most of the displacement is accommodated by it.

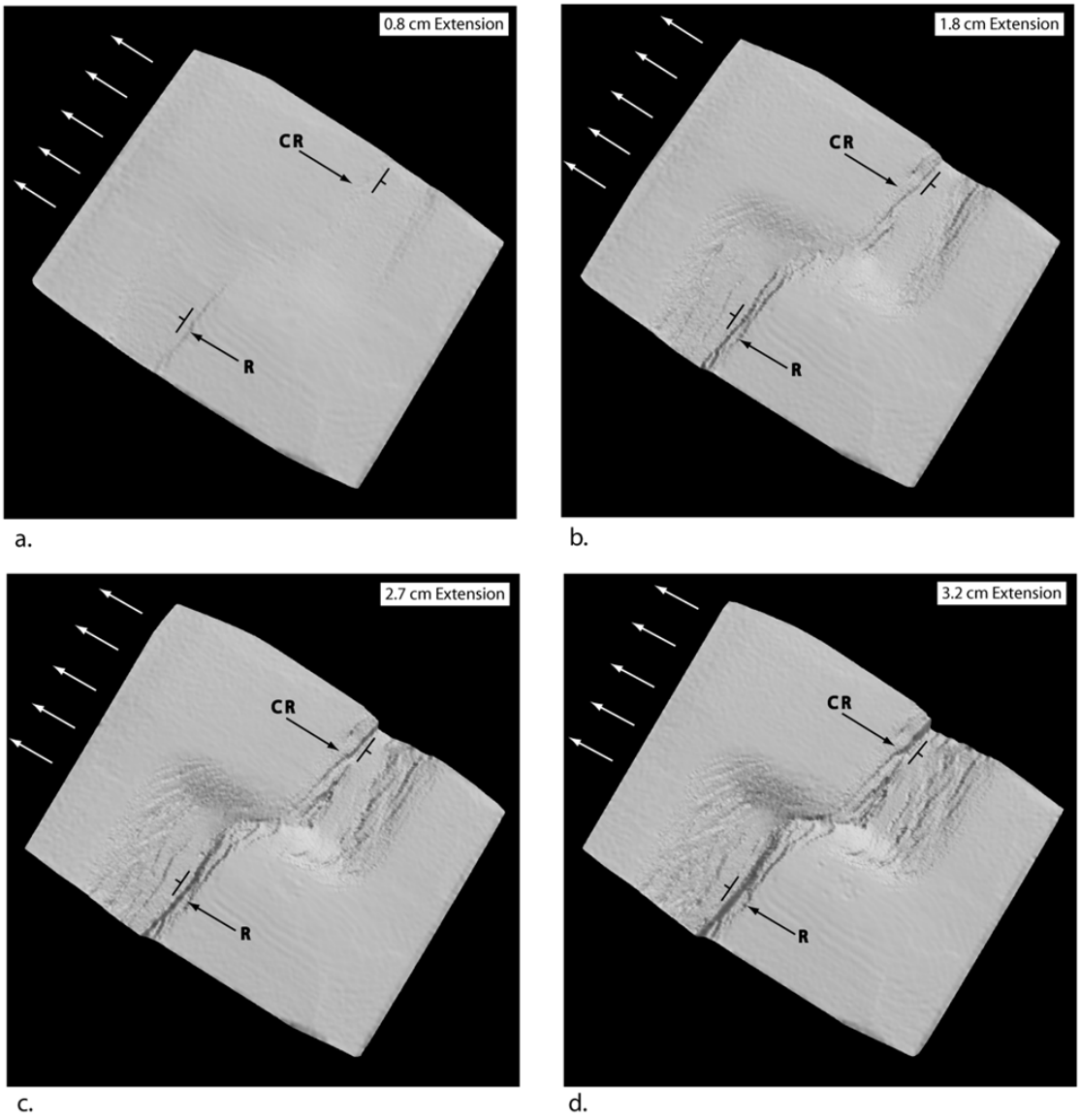

Figure 1.10: Laser-scanned three-dimensional model showing the evolution of the structure in a Divergent Normal Offset transfer zone, and the formation of the regional (R) and counter-regional (CR) faults.

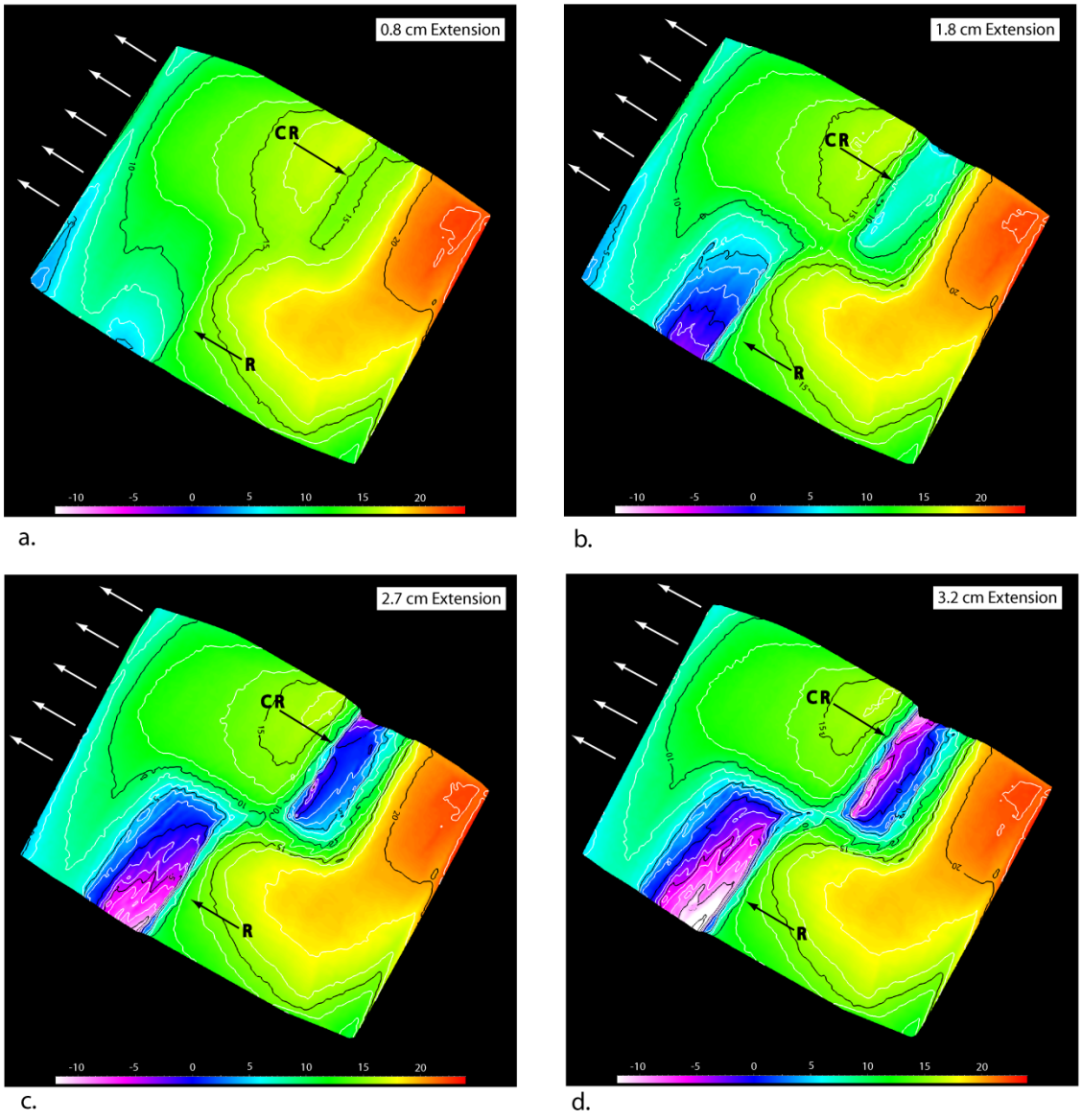

Figure 1.11: Structure contours (in millimeters) obtained from laser-scanned models showing the evolution of structural highs and lows in a divergent transfer zone.

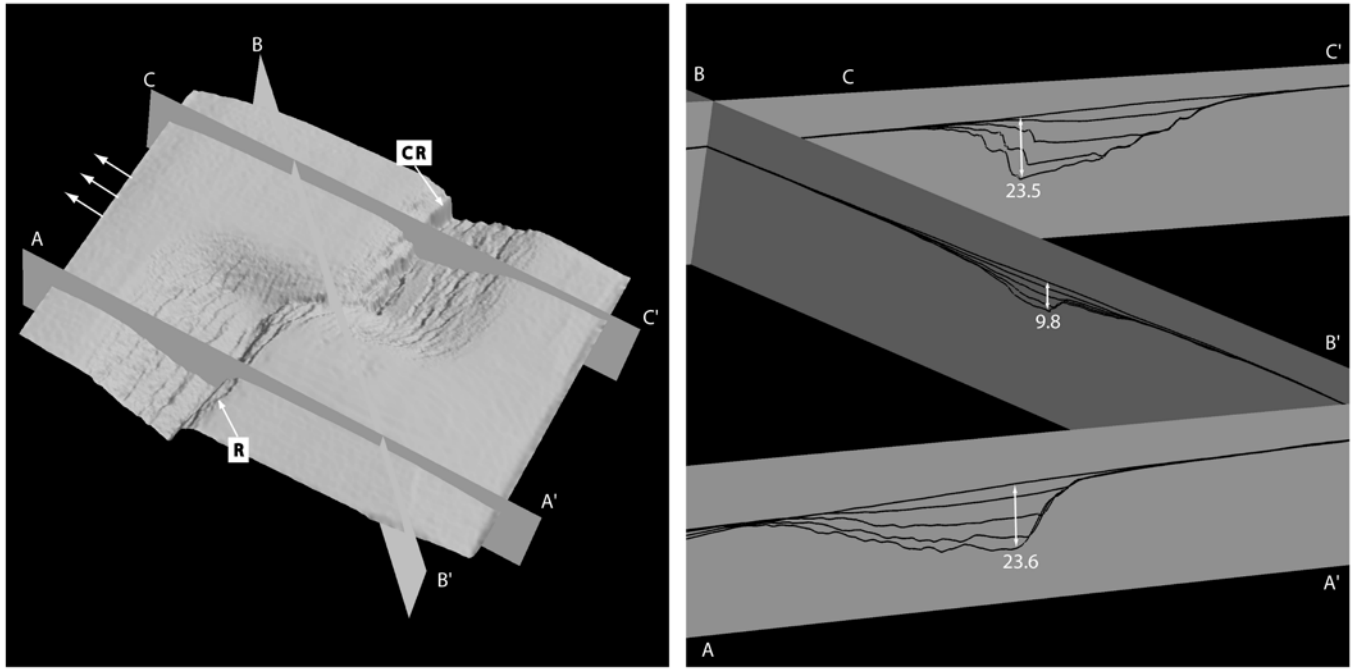

Figure 1.12: Location of three profile sections through a Divergent transfer zone. (b) Profiles AA', BB' and CC' showing the maximum reliefs along the main faults and within the transfer zones.

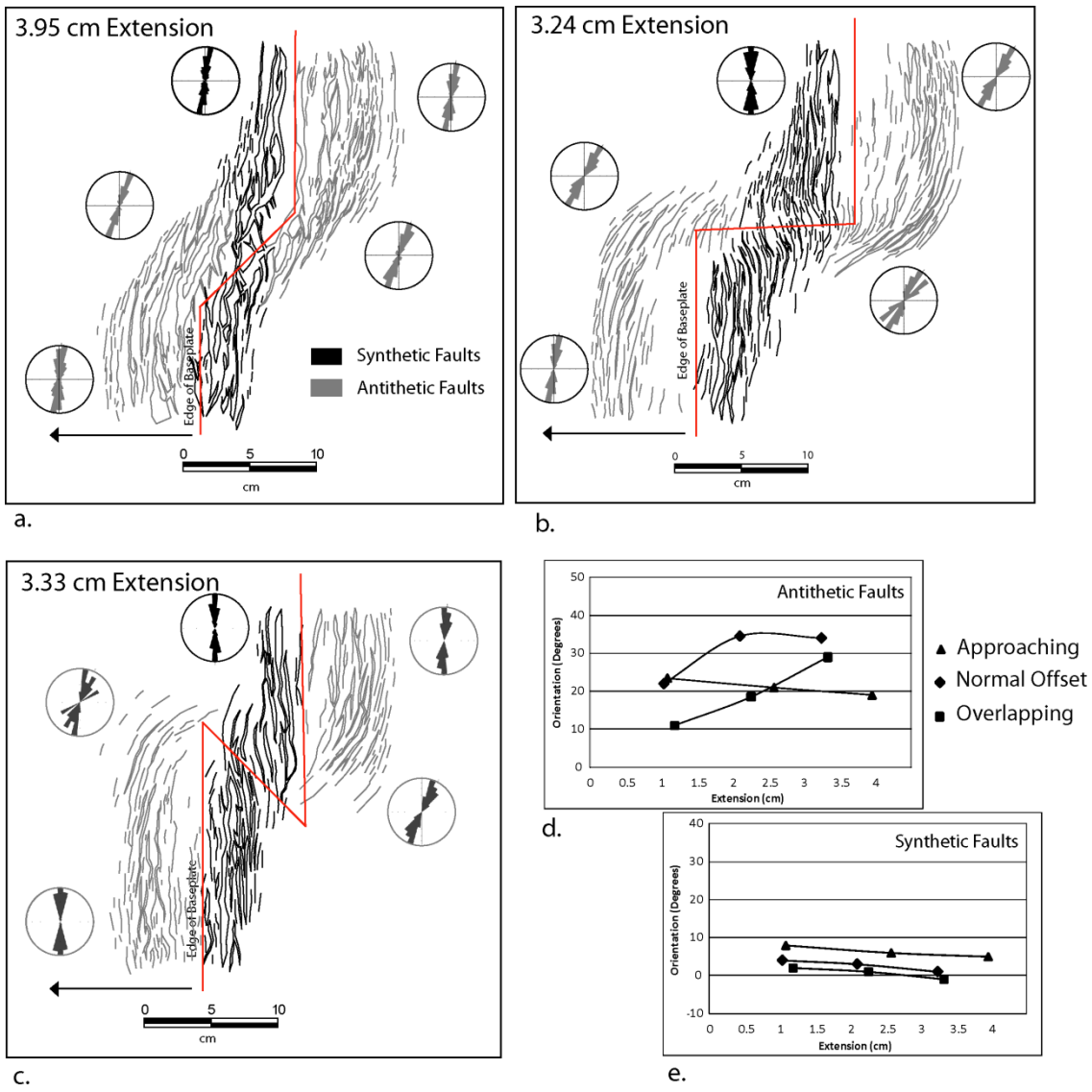

Figure 1.13: Fault patterns and orientations in the final stages of Divergent setups of (a) Approaching, (b) Normal Offset and (c) Overlapping faults. (d-e) Changes in orientations of synthetic and antithetic faults in a divergent transfer zone.

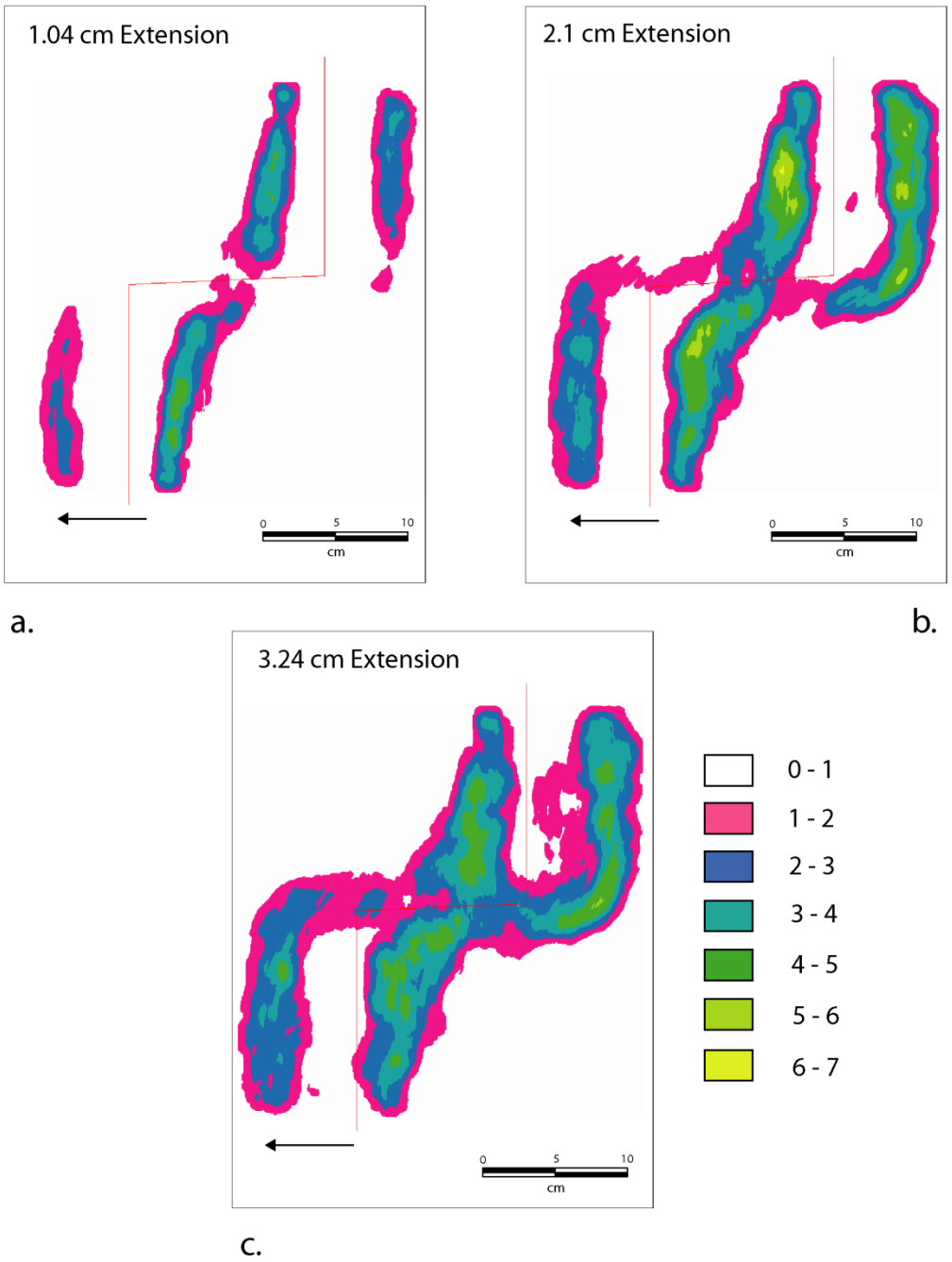

Figure 1.14: Density maps at different stages of displacement in the Divergent Normal Offset experiment. (a) 1.04 cm, (b) 2.1 cm and (c) 3.24 cm displacement. Density units are in cm/sq. cm.

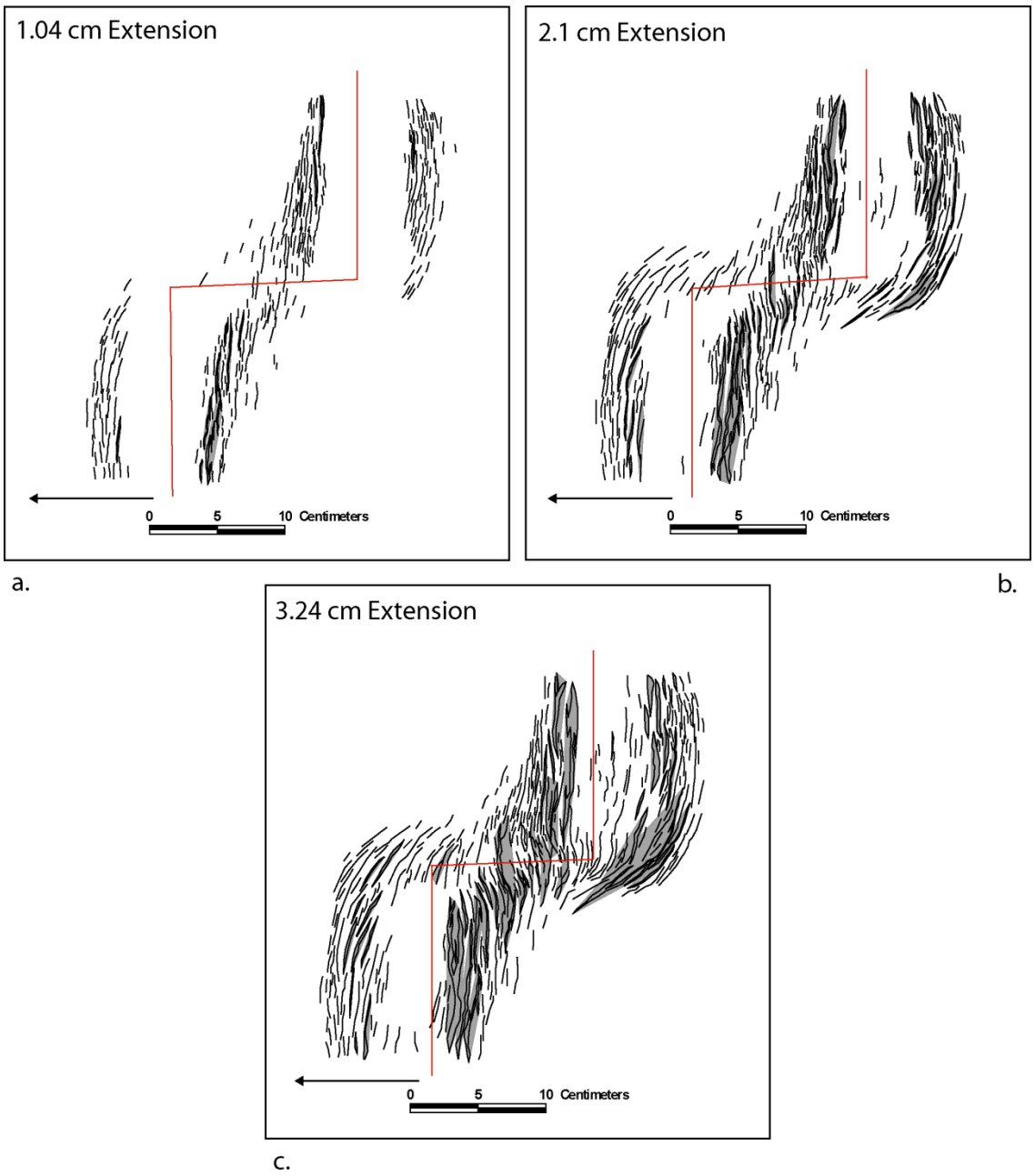

Figure 1.15: Connectivity clusters at stages of increasing displacement in the Divergent Normal Offset setup. (a) 1.04 cm, (b) 2.1 cm and (c) 3.24 cm displacement.

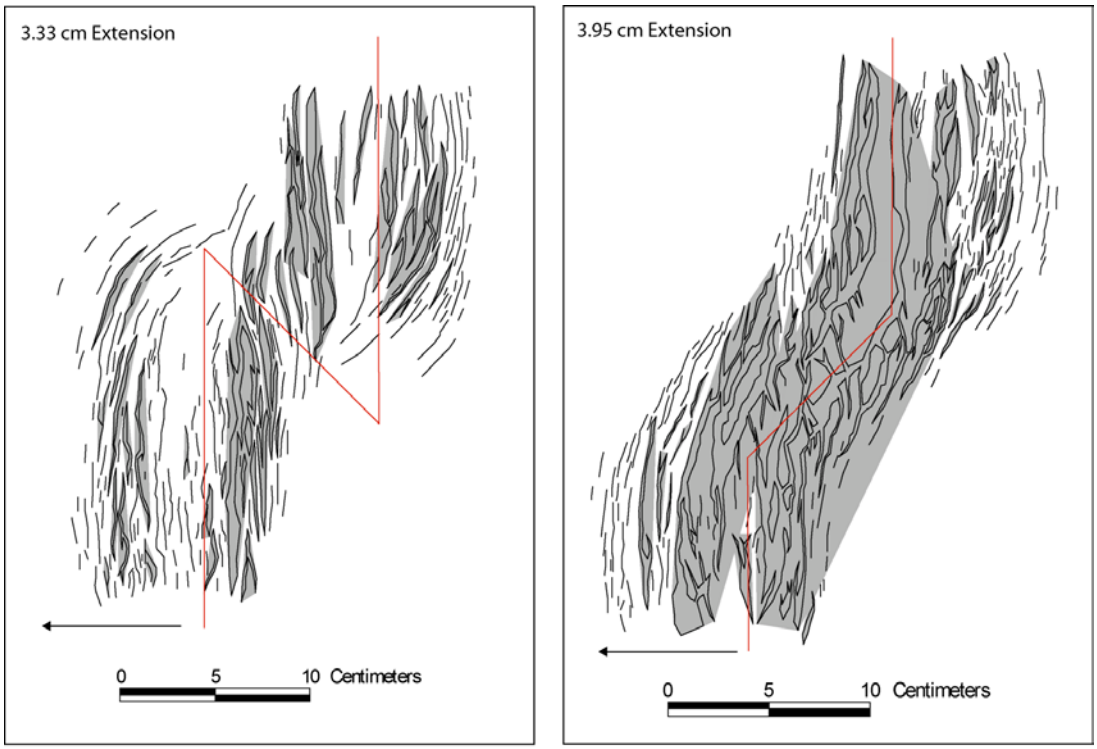

Figure 1.16: Connectivity clusters at the final stages of Divergent (a) Overlapping setup and (b) Approaching setup.

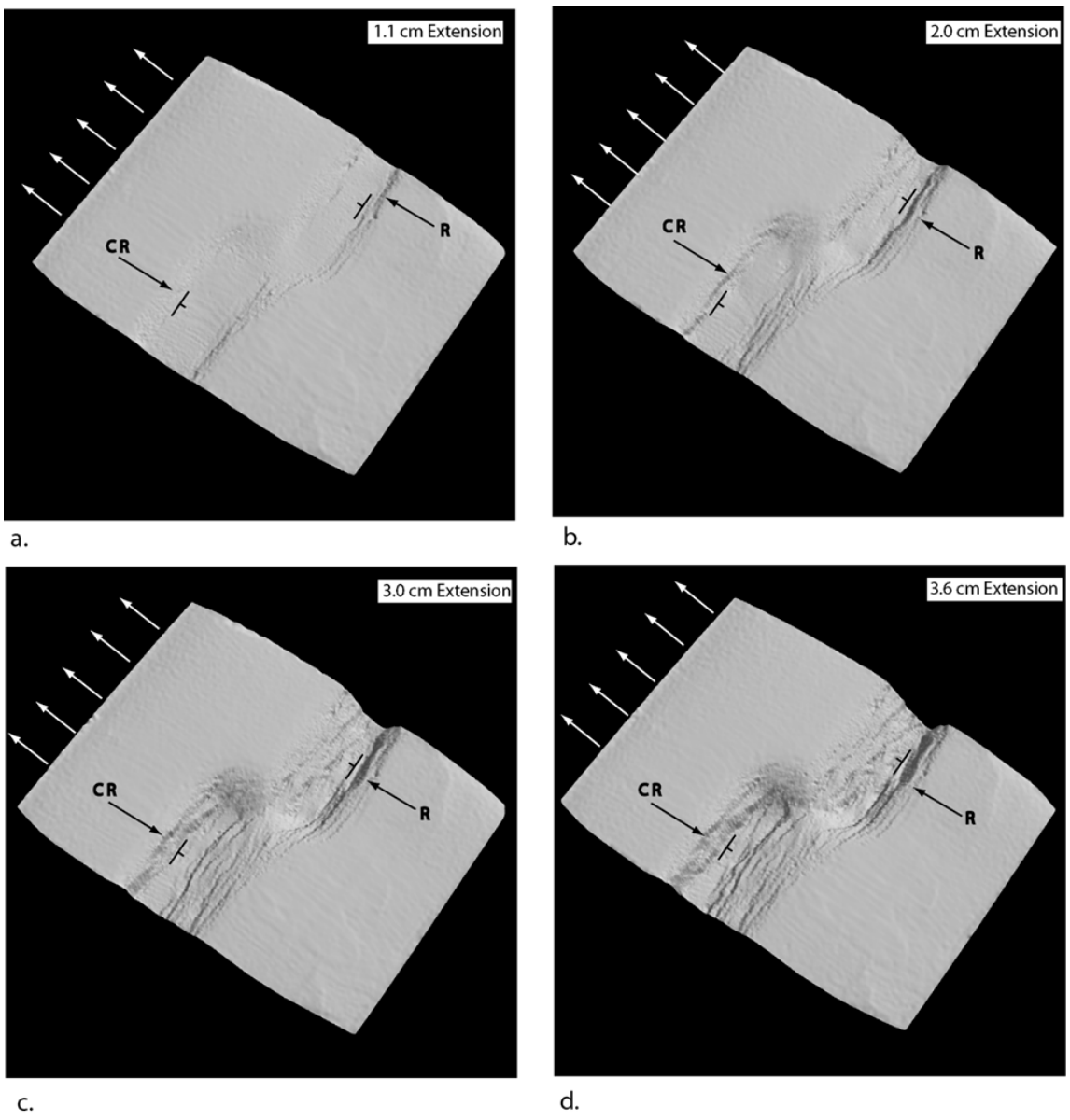

Figure 1.17: Laser-scanned three-dimensional model showing the evolution of the structure in a Convergent Normal Offset transfer zone, and the formation of the regional (R) and counter-regional (CR) faults.

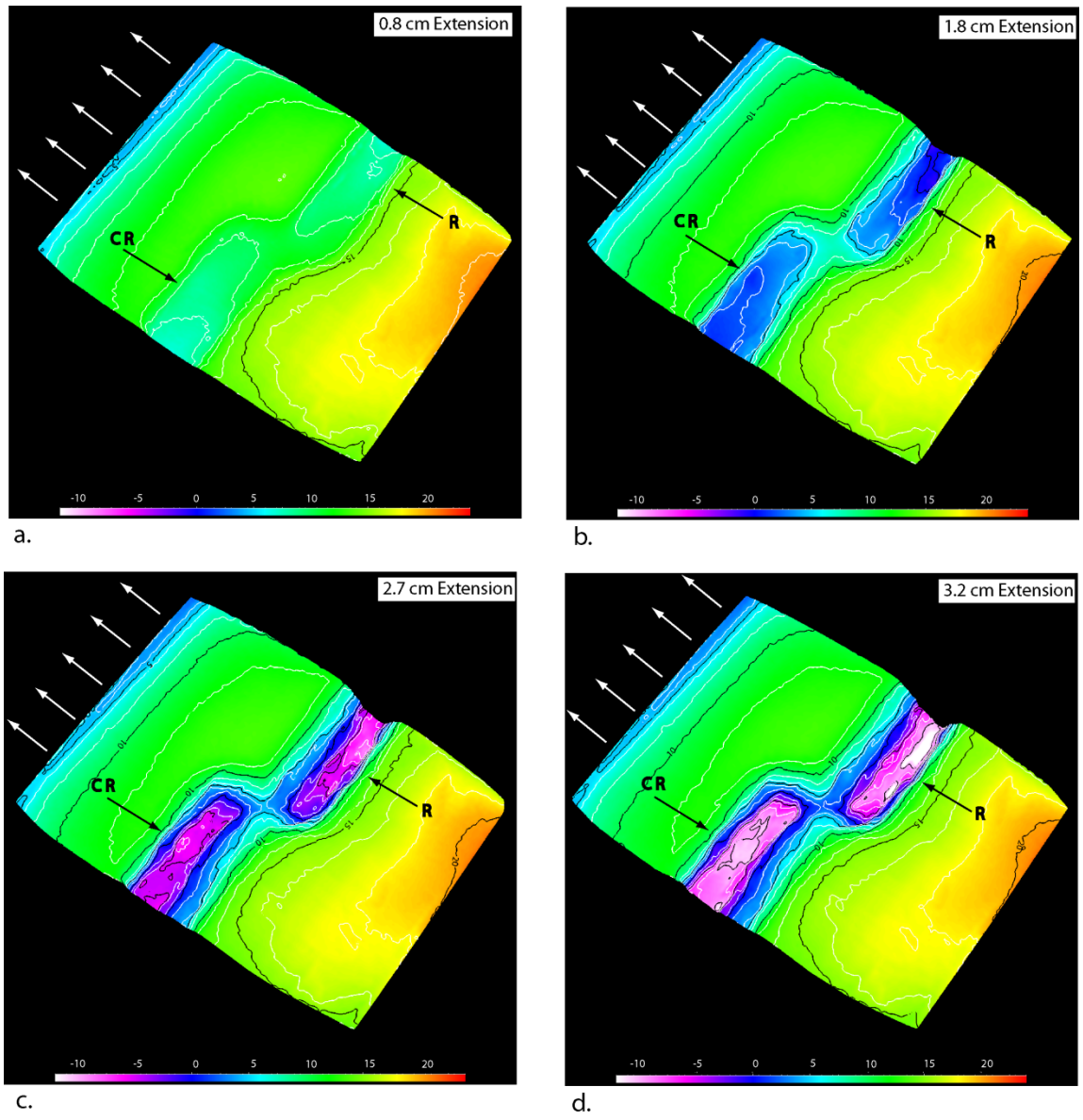

Figure 1.18: Structure contours (in millimeters) showing the evolution of structural highs and lows in a convergent transfer zone.

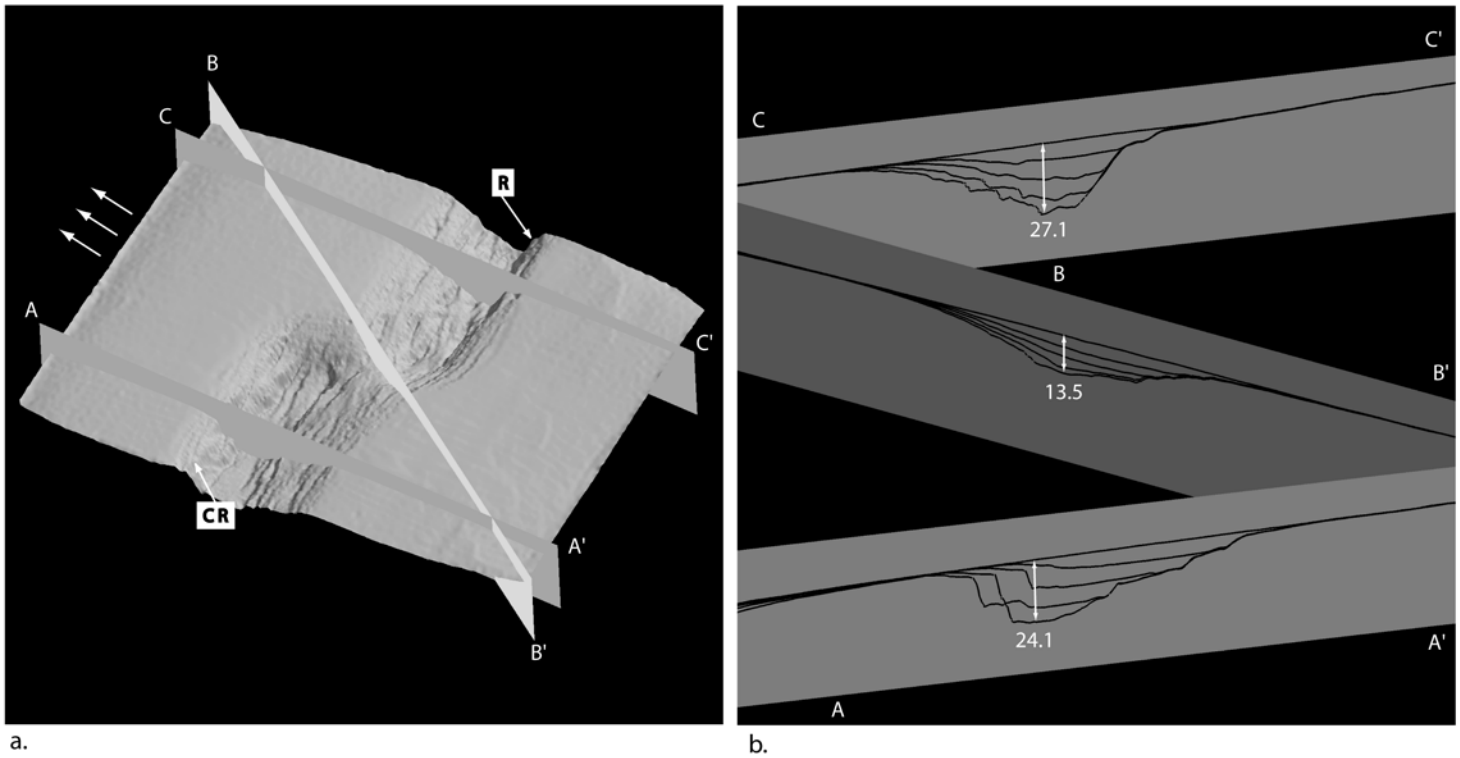

Figure 1.19: a. Location of three profile sections through a Convergent transfer zone. (b) Profiles AA', BB' and CC' showing the maximum reliefs along the main faults and within the transfer zones.

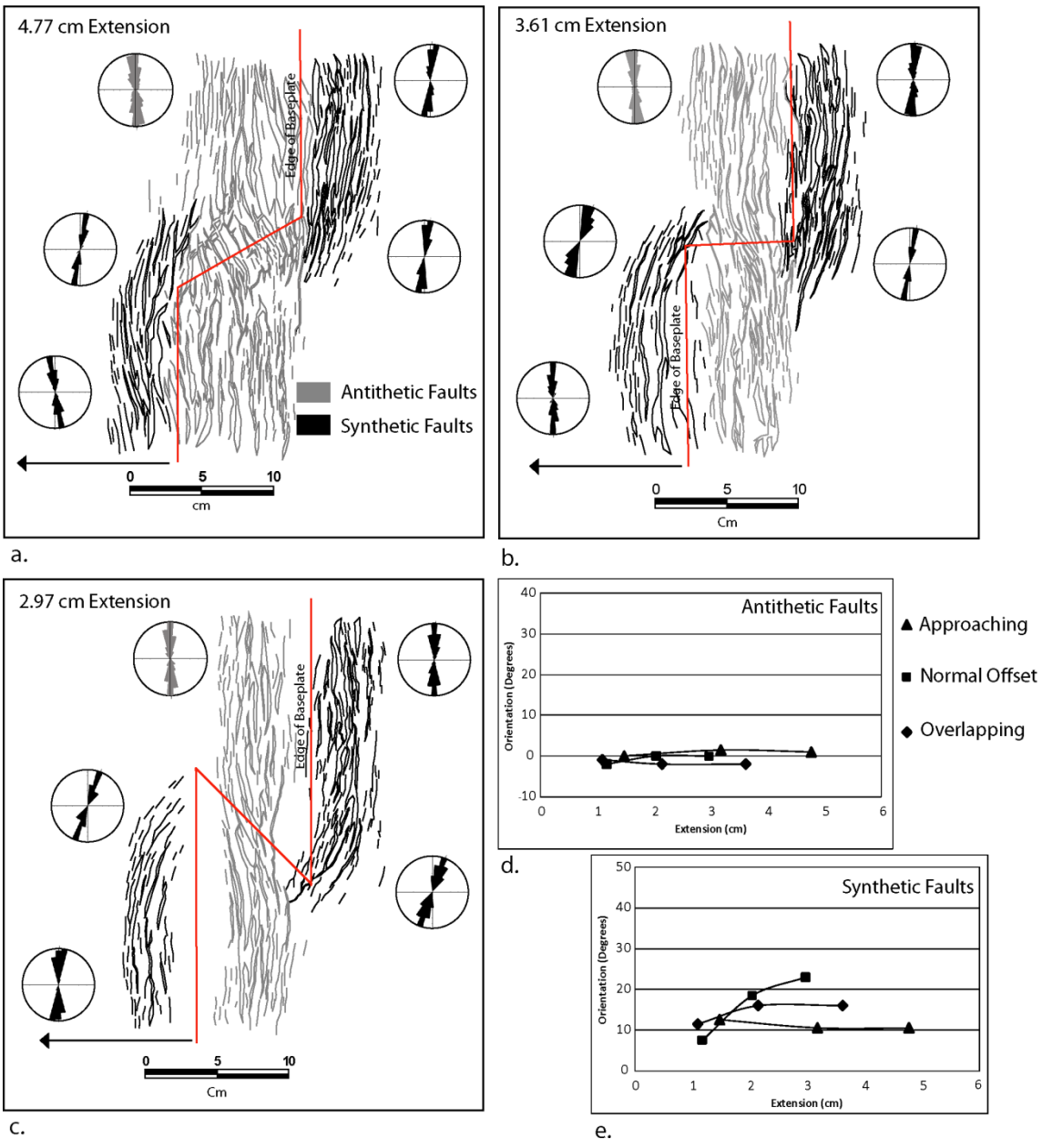

Figure 1.20: Fault patterns and orientations in the final stages of Convergent transfer zone with (a) Approaching, (b) Normal Offset and (c) Overlapping faults. (d-e) Changes in orientations of synthetic and antithetic faults in a convergent transfer zone.

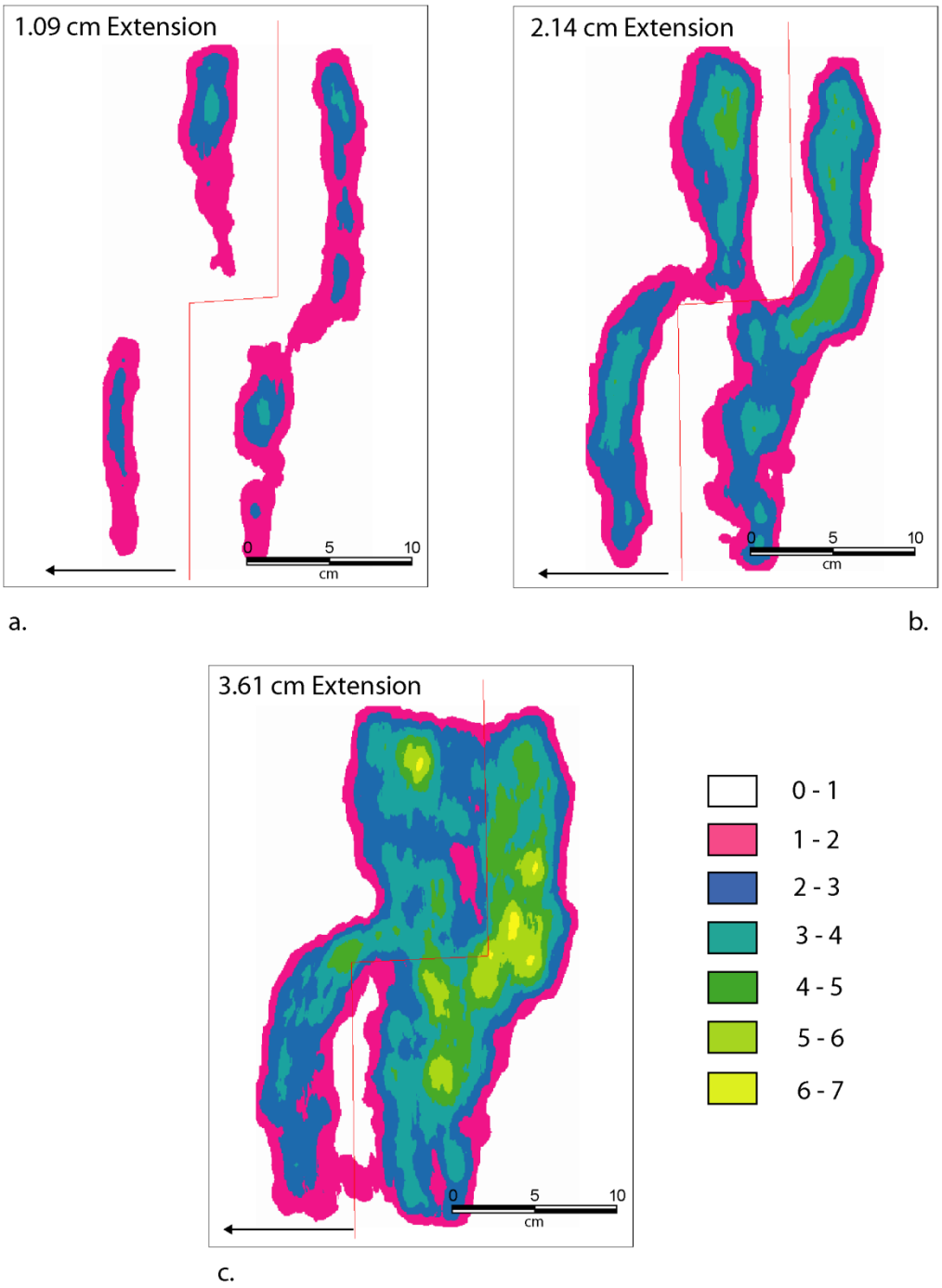

Figure 1.21: Density maps at different stages of displacement in a Convergent Normal Offset experiment. (a) 1.09 cm, (b) 2.14 cm and (c) 3.61 cm displacement. Density units are in cm/sq. cm.

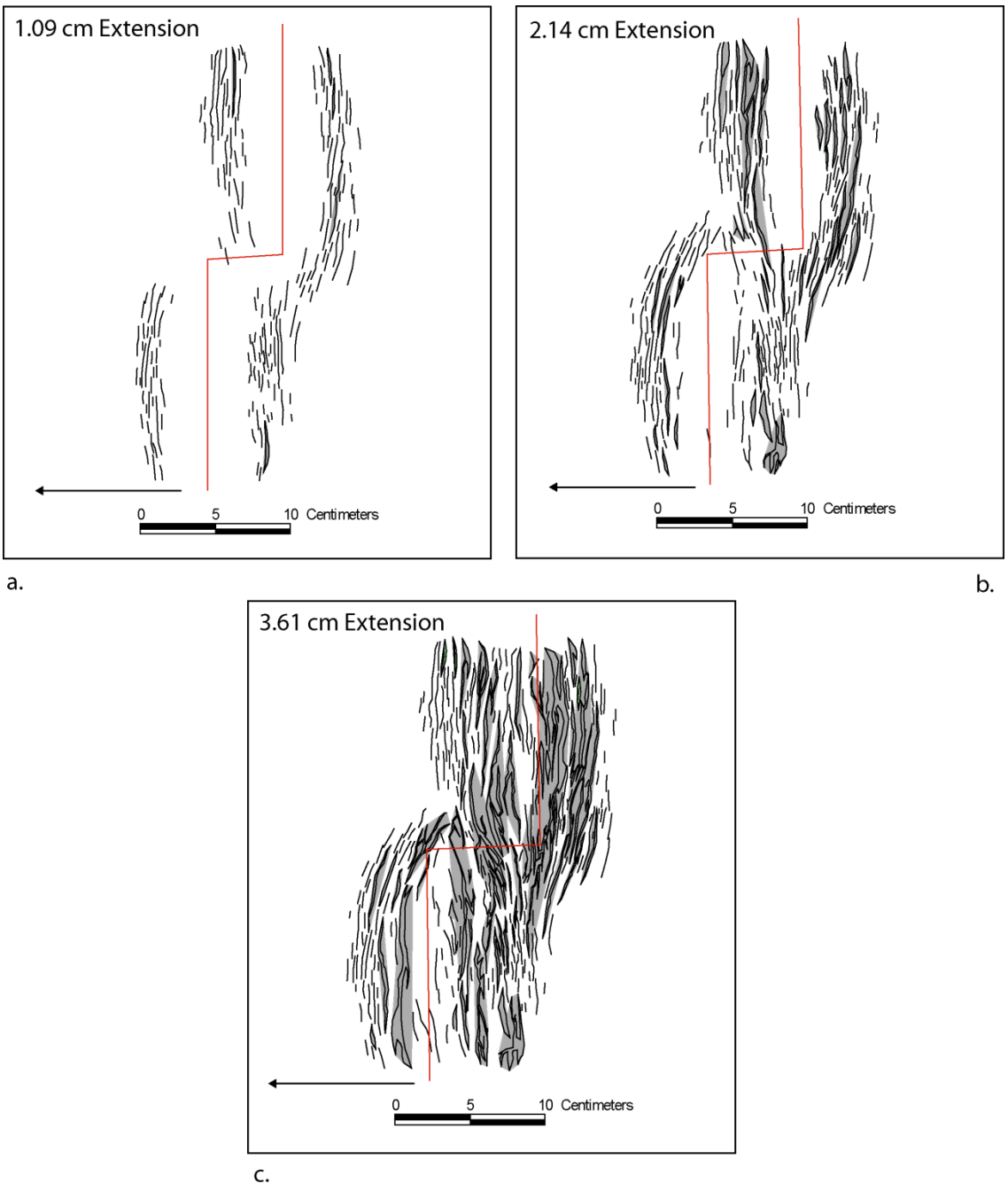

Figure 1.22: Connectivity clusters at stages of increasing displacement in the Convergent Normal Offset setup. (a) 1.09 cm, (b) 2.14 cm and (c) 3.61 cm displacement.

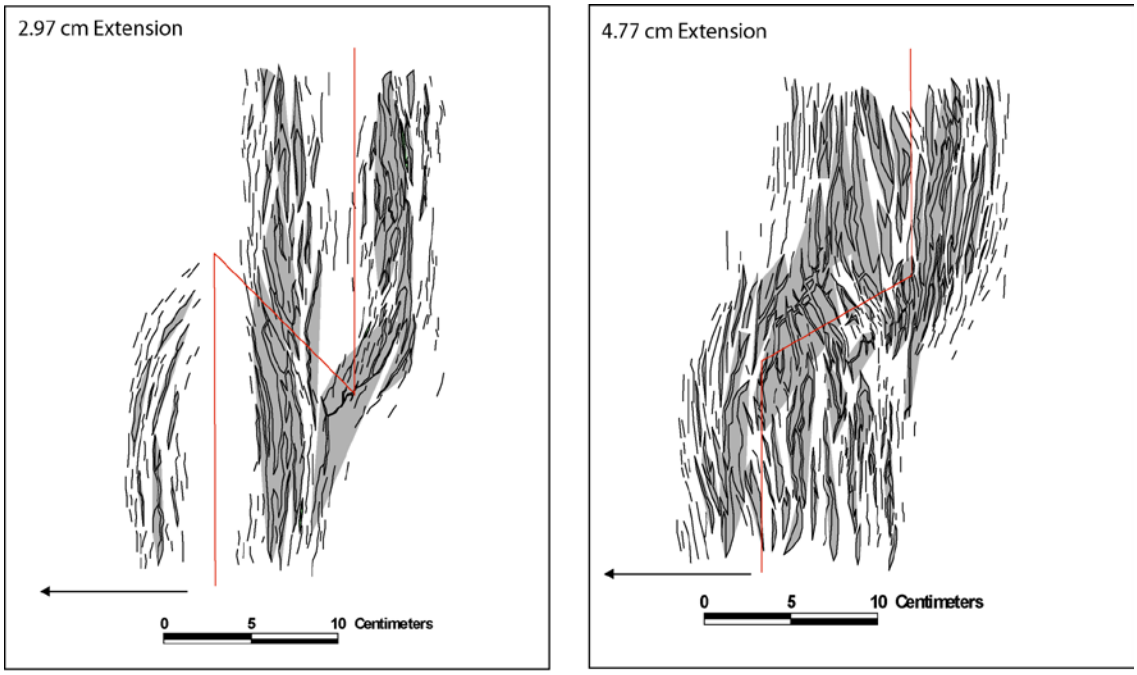

Figure 1.23: Connectivity clusters at the final stages of Convergent (a) Overlapping setup and (b) Approaching setup.

Model Configuration		Fault Orientation in Transfer Zone	Density	Connectivity
Divergent	Approaching	Antithetic Faults = Continuously decrease from 23.5° to 19° Synthetic Faults = Constant at ~ 6.33°	Higher density along antithetic faults near transfer zone	Large clusters containing connected synthetic and antithetic faults
	Normal Offset	Antithetic Faults = Increase from 22° to 34.5° and remain constant thereafter Synthetic Faults = Constant at ~ 2.67°	Higher density along straight segments of the synthetic faults	Isolated clusters along antithetic fault zone; synthetic faults are well connected.
	Overlapping	Antithetic Faults = Continuously increase from 11° to 29° Synthetic Faults = Constant at ~ 0.67°	Higher density along straight segments of the synthetic faults	Isolated clusters along antithetic fault zones; synthetic faults are well connected.
Convergent	Approaching	Antithetic Faults = Constant at ~ -0.83° Synthetic Faults = Decrease from 12.5° to 10.5° and remain constant thereafter	Higher density along synthetic zone of regional faults near transfer zone	Large clusters containing synthetic and antithetic faults
	Normal Offset	Antithetic Faults = Constant at ~ 1.67° Synthetic Faults = Increase from 11.5° to 16° and remain constant thereafter	Higher density along synthetic zone of regional faults and antithetic zone of counter-regional faults within transfer zone	Isolated clusters in synthetic fault zones; large clusters develop along antithetic faults.
	Overlapping	Antithetic Faults = Constant at ~ 0.69° Synthetic Faults = Continuously increase from 7.5° to 23°	Higher density in the straight segment along synthetic zone of regional faults	Isolated clusters in synthetic fault zones; large clusters in antithetic faults.

Table 1.1: Summary of observations of fault pattern, density and connectivity for the six experimental setups of Divergent and Convergent transfer zones.

CHAPTER 2

THREE DIMENSIONAL STRUCTURAL ANALYSIS OF A SALT CORED CONVERGENT TRANSFER ZONE IN THE SOUTH TIMBALIER BLOCK 54, OFFSHORE GULF OF MEXICO

Abstract

The Louisiana style of faulting is characterized by short, arcuate regional and counter-regional growth fault systems that commonly form complex transfer zones above shallow, Miocene level salt bodies. South Timbalier Block 54 (ST 54) constitutes one such area where a basin-ward dipping regional and a landward dipping counter-regional growth fault form a convergent transfer zone. 3D seismic and well data have been used to interpret the structure of four offshore blocks adjacent to ST 54. The interpretation reveals that the eastern and western flanks of the structure contain salt in the footwalls of the main regional and counter-regional faults; the salt rises to a much shallower stratigraphic level in the central part the transfer zone, thus forming a collapsed crest structure. Secondary antithetic and synthetic faults adjacent to the two main faults and also extending into the transfer zone, are responsible for accommodating slip between the main faults. Kinematic restorations of a series of north-south trending cross sections across the structure show that up slope evacuation of salt is a result of sediment loading and growth fault movement and the location of the transfer zone is controlled by the initial geometry of the allochthonous salt. A 3D structural model using depth converted horizons, balanced cross sections and well tops has been constructed to accurately represent the subsurface structure. A clay experimental model, equipped with a 3D laser scanning system, helped in gathering insights on the movement of salt and formation of structures under gravity. Understanding the evolution of the structure in ST 54 provides insight on similar structures in other areas of offshore Louisiana and aides in establishing the relationship between salt evacuation and transfer zone development.

2.1 Introduction

Allochthonous salt in the Gulf of Mexico plays an important role in controlling the structural style and sediment distribution, and the formation of structural traps for hydrocarbon accumulation. The style of growth faulting in offshore differs from that of most of offshore Texas style, and consists of short arcuate regional and counterregional faults due to the shallow allochthonous salt (Worrall and Snelson, 1989). The Louisiana growth faults therefore form complex salt related divergent and convergent transfer zones that accommodate deformation between the fault terminations. The terms convergent and divergent have been applied mostly to rift systems and have been based on the mutual dip of the two faults forming the transfer zone (Morley et al., 1990; Faulds and Verga, 1998). The transfer zones are common along the entire Louisiana shelf, although little is known about the factors controlling the location and kinematic history of their formation. The listric shapes of the growth faults cause rollover folds and secondary antithetic and synthetic faults to form in the hanging wall. These, along with the syngrowth sediments and evacuation of salt present challenges in deciphering the evolutionary history of the structures.

Figure 2.1 displays the present tectono-stratigraphic provinces in the northern Gulf of Mexico indicating that most of the structures in the shelf, offshore Louisiana are controlled by salt (Diegel et al, 1995). In the shallow shelf to deeper slope region, the autochthonous Jurassic evaporites, commonly referred to as the Louann Salt, rose to the sea floor and spread out as salt sheets in the Paleogene due to its lower density than the overlying sediments. This allochthonous salt not only acted as a detachment to the growth

faulting of the sediments above, but is thought to have subsequently migrated to the Plio-Pliestocene level in the outer shelf area (Diegel et al., 1995).

The South Timbalier Block 54 (ST 54) is an area where an allochthonous salt cored convergent transfer zone has formed between a regional and a counter regional fault system. ST 54 is located in the shelf region offshore Louisiana, approximately 90 miles south of New Orleans (Fig 2.1). The South Timbalier field located in ST54 was discovered in 1955 and has since been operated and leased by Exxon. In this study, the geometry of the fault system and the relationship between the faults and the allochthonous salt are analyzed along with the use of analog clay experimental models, in order to develop a model explaining a possible evolution of the structure.

2.2 Objectives and Approach

The Louisiana shelf areas in South Timbalier, Ship Shoal, Eugene Island, South Marsh Island, Vermillion, East Cameron and parts of West Cameron are abundant in salt cored transfer zones between adjacent growth faults that formed a linked system connecting isolated salt bodies (Fig 2.2). Although a number of models have been proposed for the formation of the regional faults (also termed the Roho system) and the counter-regional fault systems (Diegel et al., 1995; Schuster, 1995; Rowan et al., 1999; Hudec and Jackson, 2006), the interaction between these end member salt related fault families have rarely been discussed. The presence of salt highs within the transfer zones are common in most of the offshore Louisiana growth fault structures but the exact temporal relationship between sedimentation, growth faulting and salt evacuation at the transfer zones have not been understood.

This paper will address the relationships between salt tectonics and the evolution of a convergent transfer zone by developing an integrated structural model using the ST 54 block as an example.

The approaches used to develop the structural model include (1) interpretation of prominent horizons and faults, using a 3D seismic volume integrated with well data in the ST 54 block; (2) construction and kinematic restoration of a series of depth structural cross sections parallel to primary transport direction to understand the structural evolution; (3) construction of a 3D structural model of the ST54 area by integrating depth converted time surfaces, well data, and balanced cross sections for an accurate representation of the subsurface geometry; and (4) using experimental clay model to understand the movement of salt and development of fault patterns under gravity.

2.3 Previous Studies

Shallow structures in offshore Louisiana are commonly a result of growth faulting and/or salt evacuation. Schuster (1995) and Diegel et al. (1995) have suggested that in addition to the basinward dipping Roho system, there occurs a separate system of faults that dip landward, referred to as the Stepped Counterregional System, since they are connected to a deeper counter-regional fault system in a stepped manner (Fig 2.3). These two systems are thought to form by different mechanisms leading to different geometries (Schuster, 1995; Diegel et al., 1995; Bartsch, 1997; Rowan et al., 1999; Hudec and Jackson, 2006). The Roho system is believed to be driven primarily by extension along basinward dipping growth faults that detach at the shallow allochthonous salt. The salt is evacuated by the growth fault movement until they form a weld. Due to the extensions

updip, compressional salt cored structures form downdip from the Roho fault system. Authors have explained the cause of the Stepped Counterregional System to developing principally by salt evacuation as a result of sediment loading. The salt weld formed due to the “pseudo extension” does not form a detachment surface and no compressional features are observed updip from the counterregional system. Most of the naturally occurring examples are theorized to form as a combination of the two mechanisms (Hudec and Jackson, 2006).

The ST 54 area contains a major regional and a counterregional fault, but the geometries and evolutionary history do not quite follow the traditional mechanisms of formation of the Roho and the Stepped Counterregional System. Authors, although, have tried to explain the structure using the previous concepts. Bartsch (1999) used the ST 54 3D seismic volume, along with additional 2D lines to propose that ST 54 is an area where the two above-mentioned fault systems interact to form a convergent transfer zone. The first published work on the ST 54 area (Stude, 1978) was at a very early stage of development of the oil field and was based only on well data. It therefore did not provide much detail on the evolution of the structure or the relationship between the salt movement and faulting. Moreover, 3D seismic data and new concepts on growth faulting above allochthonous salt sheets have advanced the insight on such structures. The allochthonous salt within the transfer zone of ST 54 has also been inferred as a shallow salt dome above a deeper residual salt pillow (Apotria and Hudec, 1997). According to their interpretation, the initial structural high in the allochthonous salt controlled the location of the transfer zone.

Clay experimental models have been successfully used in the past to model fault patterns and geometries of listric normal fault systems (Cloos, 1968; Bose and Mitra, 2009, 2010) and using silicone polymer underneath wet clay as an analog for salt has also been performed (Withjack and Callaway, 2000; Ballahsen et al., 2003). Most of these studies either used flat base plate setups to induce basal extension or rigid blocks for basal subsidence, except some work by Cloos (1968) where he allowed wet clay to deform under gravity. This study used clay experiments as a mean to explore basic principles of salt movement and sediment deformation under gravity by under laying silicone polymer below wet clay and allowing the setup to deform under gravity.

2.4 Methodology

Three dimensional structural analysis of the ST 54 area is based primarily on a 3D seismic volume and well tops donated by ExxonMobil Corporation. The seismic survey was shot in the late 1980s and spans four offshore blocks viz. 54, 55, 66 and 67, covering an area of approximately 62 square miles. Well deviations for some wells were obtained from the Mineral Management Services, whereas others were derived from the coordinates of the closely spaced well tops. ExxonMobil also provided checkshot data from five wells and velocity-depth plots based on the data. Seismic interpretations were initially performed in time with the aid of well tops. The time surfaces were converted to depth and used for 2D structural restorations and subsurface 3D modeling. The tops of Sands A, C, D, E, F, G, H, I-80, I-120 and the salt shown in the stratigraphic column (Figure 3.4) were interpreted. A unit X was introduced between I-120 and the salt and stratigraphically lies in the lower Miocene between Sands H and J. The faults and tops of

each horizon were interpreted and mapped at an interval of every 10 in lines and cross lines, although larger displacement faults were additionally interpreted on a number of oblique sections in order to provide a better control on the geometry. Variance maps at different time slices were used to constrain the exact locations and terminations of the faults (Fig 2.5).

Six serial north-south trending cross sections (Inlines 32, 82, 102, 132, 152 and 192), parallel to the transportation direction were selected which were subsequently converted to depth to be used in kinematic restoration and 3D modeling (Fig 2.6). ExxonMobil donated the time-depth plots constructed from all the checkshot data in the ST 54 area (Fig 2.7). The time-velocity plot was obtained from the time-depth data and a velocity function was calculated which was used to convert the sections to depth. A constant velocity of 1850 ft/sec was assigned for salt and adjustments were made to fit all horizons to the well tops (Fig 2.8).

For the 3D structural model, the time surfaces of the horizons and faults were converted to depth using a velocity cube constructed from the checkshot data for all the five wells in the ST 54 area. Using the depth converted surfaces, cross sections and well tops, a 3D subsurface model was built in GoCAD to visualize the 3D geometry of the structure. The depth horizons were fitted to the well tops and cross section traces and were cut with all the interpreted fault surfaces in order to provide accurate representations and estimations of the structural relief and fault displacements.

The six chosen sections were then restored while decompacting in order to obtain a kinematic evolutionary history of the structure. Decompaction is an important operation that is applied to all the sections since syn-sedimentary layers undergo a substantial

amount of thickness change as the structure evolves. Decompaction is applied after the overlying layers are stripped off sequentially at each stage of restoration (Rowan, 1993). For the current decompaction process, a sand-shale ratio of 1:1 was considered for all the sedimentary units, while salt, which does not undergo any compaction, was assigned a solidity of 1. Isostatic adjustments due to the comparatively thin overburden were considered to be negligible in the current scenario.

Factors that are needed to be considered for balancing cross sections in extensional terrains (Gibbs, 1983) are quite different than those used for restoration of compressional structures (Dahlstrom, 1968). At the same time, the techniques used for restoration of sections involving salt assumes a number of additional factors and has been discussed in various literatures (Worrall and Snelson, 1989; Schultz-Ela, 1992, 1991; Rowan, 1993; Diegel et al., 1995). The principal argument being that due to the ductile behavior of salt, there would occur a large amount of out of plane motion. Therefore the area of salt cannot not be balanced, although the other sedimentary units in the supra-salt and sub-salt levels should be area balanced. Since the area of the units in each stage of restoration changed due to the application of decompaction, the only method by which balancing could be achieved was to maintain the area between any deformed decompacted stage and the next restored decompacted stage. Salt was the only unit that did not undergo any change in area during decompaction and therefore for the purpose of this study, it was maintained at constant area throughout the entire restoration process. This provided an additional constraint to the possible evolution of the salt structure. An inclined shear mechanism of deformation was assumed for all fault blocks and the antithetic shear angle was varied to fit the fault blocks with minimum gaps and overlaps.

A clay experimental model has been used in this study to gather insights on the deformation mechanism of salt underlain sediments under the influence of gravity. The details of the setup and the concepts behind the use of the model have been discussed in a later section for a matter of coherency since it is important for the reader to visualize the structural geometry and its evolution before delving into the details of the experiment.

2.5 Structure

The structural geometry of the area will be described with respect to the six depth converted inlines mentioned in the previous section and the 3D structural model. All the sections (Fig 2.9) showed a significant dip of the sediments towards south and the salt was interpreted to form welds away from the transfer zone both in the footwalls and hanging walls of the main regional and counterregional faults. In addition, sedimentary units thickened away from the transfer zone towards east. For the entire area, the geometry of the base of the salt displays a high angled slope to the south which gently slopes towards north forming an east-west trending basal hinge along the central region.

The eastern and western sections (Inlines 32 and 192) show the main counterregional and regional faults dipping towards north and south respectively, that form a simple rollover or half-graben geometry with salt wedges in the footwall (Fig 2.9 a & f). Both the main faults detach at the base of the unit X but at different depths due to the basal geometry of the salt. The presence of salt in the footwalls is indicated by the deformed sediments adjacent to the main faults. Secondary antithetic and synthetic faults are present in the hanging wall block in both the sections, although there are fewer faults adjacent to the counterregional fault than there are to the regional fault. Towards the

center of the transfer zone (Inline 82, 102 and 132), the salt rises to a shallower stratigraphic level forming a collapsed crest above the salt (Fig 2.9 b, c & d). The two separate salt highs that develop near the transfer zone at shallower depths (Inline 132) continue towards east at deeper levels as observed in Inline 152 (Fig 2.9 e).

The overall 3D geometry reveals a regional and a counterregional fault dipping towards each other forming a convergent transfer zone. The 3D models for the top of C-Sand and F-Sand show that the main faults curve towards each other from an orientation of east- to a trend of northwest-southeast towards the center of the transfer zone (Fig 2.10). The displacements along these two faults also decrease as they approach the transfer zone. The amounts of fault gaps for the main faults also increase from C-Sand to F-Sand and therefore indicate increasing displacement with depth. A number of secondary antithetic and synthetic faults that accommodate the displacement (Apotria, 1998) are present at the transfer and trend parallel to the local orientation of the main faults. Figure 2.11 a shows the 3D structure of the top of the salt and its relationship to the regional and counterregional faults. The two faults detach at deeper levels to the west and east but terminate above the salt within the transfer zone. Salt welds form underneath the main faults in the southwest and northeast and rise to much higher level within the transfer zone. The high terminations of the salt against the two faults in the footwall blocks have also been modeled. The diapirism of the salt results in a structural high in the deeper sedimentary units within the transfer zone (Fig 2.11 b) and is evident in the structural contours of the F-Sand surface (Fig 2.10 b).

2.6 Structural Restorations

2.6.1 Assumptions

The geometry of the restored sections and timing of salt movement vary with other methodologies of restoration, although the restoration results are unique for the particular technique and assumptions that have been applied. Two major factors impacted the outcome of the restoration process:

1. Constant salt area throughout the process of restoration as opposed to variable salt area.
2. Thickness variation of sedimentary units that have been pierced by the salt in the central part of the structure.

Restoration of Inline 82 has been used to illustrate the justification for these two assumptions.

Figure 2.12 shows the restoration of Inline 82 assuming downbuilding of sediments as the mechanism of molding of the salt structure. This technique of restoration, as outlined by Rowan (1993), restores top of the sedimentary layers to the paleo sea floor while maintaining the baseline of the section at constant depth. Therefore, the areas created at each stage of restoration between the supra-salt and subsalt sediments are assumed to be occupied by salt, implying that the area of salt would no longer be constant during the entire restoration process. This phenomenon is attributed to the large amount of out of place movement of salt. The area of salt started to decrease from the initial Stage 1, when X Sand was deposited on the northern and southern slopes and continued to do so with more sedimentation. The salt tapered against the sediments in Stages 1, 2 and 3 due to the greater rate of overburden growth than the rate of structural

relief of salt (Talbot, 1995). H Sand and the younger sediments deposited thereafter (Stage 4 onwards) halted the rise of salt and caused it to mostly evacuate out of the section, ultimately resulting in the salt weld on either side of the basal hinge.

In this model of downbuilding sediments, more than 6 times of the salt area moved out of the section during the evolution of this structure, in a direction perpendicular to the plane of the section. Therefore it is difficult to account for the lost volume of salt and the present lateral position occupied by it. During the process of decompaction, the only lithological unit that conserved area was that of the salt due to its incompressibility. The fundamental assumption of a variable area of salt would then be unjustified. During the restoration process, balancing the area of salt provides an additional constraint to the salt geometry during the evolutionary process. Therefore the model of downbuilding as a process of kinematic evolution of this structure is discarded for the purpose of the present study.

One of the liberties taken during the restoration of Inline 82 along with Inlines 102, 132 and 152, is the adjustment of areas of the sedimentary units where the salt has pierced through. As the salt begins to pierce through the sedimentary layers above, the areas of the pierced units have to be adjusted within that fault block in order to balance the areas that are now occupied by salt. For example, between Stages 3 through 8 (Fig 2.13) in the center of the section, the salt begins to pierce the X, I-120, I-80 and H Sand, thereby taking up their area. For balancing the areas of these units, their thicknesses were increased within that fault block. In order to accommodate such a minor area, the changes in the thicknesses were less than even 1%. This adjustment is applied to all the pierced units in Inlines 102, 132 and 152.

2.6.2 Structural Evolution

The evolution of the ST 54 structure has been deciphered with the help of restoration of the six dip sections that are representative of the entire area. The evolutionary process can be subdivided into three zones viz. the western, eastern and central zones due to the different geometries, although the process of deformation has been kinematically consistent throughout the area.

1. Western Zone: Inline 32 is representative of the western zone and cuts across the regional fault. The structure reveals that the regional fault dips towards the south and detaches at a deeper level along the southern slope and continues out of the section (Fig 2.9 a). There is a general slope of the sediments to the south with significant thickness change across the regional fault and secondary synthetic and antithetic faults occurring in the hanging wall rollover accommodate the deformation. The shallow units on the footwall of the regional fault are undeformed, although the deeper units steepen against the fault due to the deformation of salt. The restoration of this section (Fig 2.14) shows that there was a significantly thick salt present above the southern slope and the regional fault initiated at a very early stage, detaching above the salt and allowing more sediment to be deposited above it (Stage 1). With increasing displacement towards south and sedimentation, the salt was evacuated from the base of the regional fault into the basal hinge area, deforming the sediments on the footwall block. The salt begins to migrate up the slope during the deposition of the I-80 Sand (Stage 3) and gets completely evacuated from the southern slope after the deposition of the D Sand (Stage 8) thus forming a weld.

The weld acts as a lubricating fault surface and allows further displacement while the units D, C and A Sands are deposited.

2. Eastern Zone: The structure in the eastern zone is represented by Inline 192 that shows a northward dipping counterregional fault detaching at the northern slope (Fig 2.9 f). This section indicates a thicker sequence of sediments in the footwall of the main fault that also steepen against the fault indicating the presence of salt in the footwall. Kinematic restoration of the structure (Fig 2.15) shows that the counter-regional fault initiated above the gentle northern slope after deposition of the X-sands and I-120 sands (Stages 1 and 2 respectively), although greater sediment accumulation occurred on the southern slope than the northern slope. This forced the salt to again evacuate towards the central part of the section from both the slopes. Complete evacuation of the salt occurred earlier on the northern slope (by the end of deposition of the C-sands in Stage 7) than that in the southern slope (during deposition of A and B Sands in Stage 9).

3. Central Zone: The central zone of the structure spans through Inlines 82 to 152 and illustrates the transition from the regional fault related half graben structure in the west to the counterregional structure in the east. Kinematic restorations of Inline 82 (Fig 2.16) show that although the final geometry of Inline 82 is a half graben, salt began to pierce through the units X, I-120 and I-80 after deposition of the H-Sand. Salt evacuation from the northern and southern slopes continued very late in the deformation, until welds were formed during the deposition of the D (Stage 8) and A Sands (Stage 9) respectively. The

formation of Regional 1 fault after the deposition of the D Sand resulted in two individual salt highs against the footwalls of the two faults (Stage 8).

The centre of the transfer zone was a collapsed crest structure above the salt high (Inline 102). The structure is not dominated by displacement along any single fault, but by small displacements along a number of faults including the main regional and counterregional faults that terminate above the salt. The restoration of this section (Fig 2.17) shows the early presence of salt on both sides of the basal hinge with initial faulting occurring during Stage 3 in the counter-regional direction after the deposition of X, I-120 and I-80 Sands. With progressive accumulation of the sediments, salt symmetrically flowed to the hinge area from either side and initial faulting gave way to piercement of the units above (up to the level of the H Sand in). Continuing sedimentation forced the salt to further evacuate from the slopes until they formed welds (Stages 8 and 9), at which point the diapirism ceased. Extension occurred simultaneously but by different amounts in the north and south. Since the faults change orientation at the transfer zone and Inline 102 trends north-south, some movement of salt might have taken place oblique to this particular section.

The collapsed crestal structure transitions to the east into a half graben with the counterregional fault taking up most of the displacement (Inlines 132 and 152).
Two distinct salt highs develop due to the large displacement along the antithetic fault to the counterregional (Fig 2.18 & Fig 2.19). Although the general slope and thicknesses of sediments increase towards south due to the counterregional fault, there is considerable little thickness change across the fault inspite of the large displacement. In Inline 132, the shallow salt high initiates piercement at an earlier stage and displaces greater number of

sedimentary layers (X through G-Sand) while in Inline 152, the piercement starts late and remains within the H-Sand. Restoration of Inlines 132 and 152 shows that although the initial geometry in Stage 1 were similar, advent of the large antithetic fault at different times led to different final geometries and piercement histories of the salt.

2.7 Summary

The structural geometry and evolution of the ST 54 area can be summarized as follows:

1. A steeper southward slope and a gentler northern slope existed in the area above which the allochthonous salt had accumulated. Due to sedimentation and growth faulting, the salt evacuated from the slopes into the basal hinge area. The major regional and counterregional faults detached above the top of the salt horizon.
2. The steep southern slope caused much greater accumulation of sediments above it.
3. The initial geometry and the kinematic process of salt evacuation is consistent throughout the entire structure but resulted in different final geometries due to the regional and counterregional faults evolving at different depths and forming the transfer zone between themselves.
4. The gentle northern slope in the east allowed salt to be present and acted as a detachment to the counterregional fault, while its absence in the west allowed only the regional fault to form.

The kinematic restoration of the sections brought out a few key features that need some deeper understanding. First, as faulting and sedimentation occurred above the slopes, the salt migrated up the slopes, accumulated and pierced sediments above the

basal hinge resulting in a greater thickness and higher structural relief at that location. Second, the different final geometries evolved within the area from broadly similar initial geometries although the overall deformation process was consistent. In order to gather insights on these phenomena and their effects, clay experimental model was constructed to illustrate the mechanisms of salt movement under gravity.

2.8 Clay Experimental Model

2.8.1 Experimental Setup

A simple experimental setup was constructed by placing wet clay on top of a thin layer of silicone polymer. Silicone polymer has been successfully used in experimental models as an analog of salt due to similar physical and flow properties (Weijermars et al., 1993; Vendeville, 1987). The base of the setup was a bent plate that sloped on two sides to the right and left by an angle of 5° forming a hinge through the middle of the base plate (Fig 2.20). The double sloping plate was used to match the northern and southern slopes of the ST 54 area, but experimental purposes both slopes were angled by equal amounts. The amount of slope was made higher than other previous studies in order to obtain the results faster otherwise (1) the clay would have started to dry and (2) the silicone polymer would have spread in a radial manner rather than flow down the slope. The thickness of the silicone polymer was kept constant at 1 cm while the overlying clay varied in thickness from the slope (4 cm) to the crest (2 cm) since top of the clay surface was made horizontal. The silicone polymer was not placed on one half of the left slope in order to simulate similar distribution of salt in the ST 54 area. The setup was left for the silicone polymer to respond and flow under gravity.

A 3D laser scanner was placed 35 cm above the top surface of the clay and it scanned at equal increments of time. The laser scanner contains four sets of line lasers that swipe across the clay surface and an optical CMOS sensor that receives these lines. The locations of points on the surface are calculated by a method of triangulation (Petrov et al, 1998; Bose and Mitra, 2010). The laser scanner produces a resolution of 0.03 cm point density which enables an extremely accurate virtual representation of the clay surface once it has been recreated in GoCAD.

2.8.2 Experimental Results

The results of the experiments will be illustrated with the help of the 3D surfaces built from the laser scanned data. Figure 2.21 a, b and c shows the contoured top of the clay surface at three stages of development of the structure and Figures 2.21 d and e show the contoured and isochore surfaces of the top of the silicone polymer. Two different structures develop along the basal hinge of the base plate due to the unequal distribution of the silicone polymer. On the lower half of the experimental setup where the silicone polymer was absent on the left slope, the clay developed a system of faults dipping mostly to the right, with some antithetic faults developing near the surface. These faults were widely spaced and initiated above the up-slope boundary of the silicone polymer. The silicone evacuated from the base of the faults and probably flowed down slope as is suggested from the contoured and isochore surfaces of the top of the silicone polymer. On the other half where the polymer is present on both slopes, the clay formed a collapsed crest structure above the basal hinge with very closely spaced faults dipping towards each other. A schematic diagram showing the fault geometries in cross section is

shown in Figure 2.22 a and b. The silicone polymer not only formed a structural high along the hinge, but also thickened considerably as observed in the isochore surface. This indicated that there occurred some up slope movement of the silicone polymer driven by faulting on the clay. The migration of silicone to the hinge had probably occurred from both the slopes with thinning on either side of the crest (Fig 2.22 c). The isochore surfaces indicate the thinning of the polymer on either side of the crest as well. These two fault systems interacted with each other right at the boundary of the silicone polymer.

The experimental model illustrates the following facts:

1. The silicone polymer can evacuate from slopes and migrate up to the crestal area and not necessarily flow down due to gravity.
2. A collapsed crestal structure can form in the hinge area when a basal hinge is present with slopes in two directions.
3. Two different systems of faults can evolve due to the lateral variation in the distribution of the silicone polymer.

2.8 Conclusions

The three dimensional structural analysis and restoration of the ST 54 field provides a possible kinematic evolutionary process for the current geometry. In the west, the salt evacuated from the base of the fault, up the southern slope to the basal hinge area primarily due to sedimentation and growth faulting, while on the eastern side the salt evacuation occurred from the steep southern slope as well as the gentler northern slope. In the center of the transfer zone, the salt pierced the sedimentary units above to result in a collapsed crest structure above the basal hinge.

Growth faults initiated due to sediment loading at a very early stage throughout the structure but finally formed different geometries due to the presence of the the regional and counterregional faults with a convergent transfer zone forming in between. The controlling factor for the location of the transfer zone can be attributed to the initially varied distribution of salt north of the basal hinge, as also illustrated in the clay experimental model. Boundary of the salt not only acts as a discontinuity and but also allowed major faults to detach at different locations. In this case, the presence of salt in the northern slope on the eastern flank enabled the formation of a counter regional fault, while its absence in the western side allowed the regional fault to form along the southern slope. The greater displacement along the main regional and counterregional faults resulted in more sedimentation and therefore more salt evacuation towards the footwall blocks. The presence of the basal hinge and interaction of the main regional and counterregional faults, along with the secondary antithetic and synthetic faults within the transfer zone caused the salt to form a collapsed crest structure at that location.

The offshore Louisiana shelf region of the Gulf of Mexico is abundant in similar structures where counterregional and regional fault systems form complex salt cored transfer zones. These structures form important hydrocarbon traps in these areas and the kinematic model of the ST 54 area can not only be used to understand their evolutionary history but also provide insights into the hydrocarbon system, their formation and migration.

References

Apotria, T., 1998, Relationship of salt evacuation to growth fault displacement transfer, Gulf of Mexico (abs): Annales Geophysicae, v. 16, p. 75.

Apotria, T. and M. R. Hudec, 1997, Controls on displacement transfer and fault linkage in salt-detached fault systems, Gulf of Mexico (abs.): Geological Society of America Abstracts with Programs, v. 29, p. 199.

Ballahsen, N., J-M. Daniel, L. Bollinger and E. Burov, 2003, Influence of viscous layers on the growth of normal faults: insights from experimental and numerical models: Journal of Structural Geology, v. 25, p. 1471-1485.

Bartsch, E. C., 1999, Evolution and structural interaction of end-member, salt-related fault systems : northern South Timbalier area, offshore Louisiana: M.S Thesis, University of Colorado, Boulder, Colorado.

Bose, S., and S. Mitra, 2009, Deformation along oblique and lateral ramps in listric normal faults: Insights from experimental models: American Association of Petroleum Geologists Bulletin, v. 93, p. 431-451.

Bose, S and S. Mitra, 2010, Analog modeling of divergent and convergent transfer zones in listric normal fault systems: American Association of Petroleum Geologists Bulletin (in press).

Cloos, E., 1968, Experimental analysis of Gulf Coast fracture patterns: American Association of Petroleum Geologists Bulletin, v. 52, p. 420-444.

Dahlstrom, C. D. A., 1968, Balanced cross sections: Canadian Journal of Earth Sciences, v. 6, p. 743-757.

Diegel, F. A., J. F. Karlo, D. C.Schuster, R. C. Shoup, and P. R. Tauvers, 1995, Cenozoic structural evolution and tectono-stratigraphic framework of the northern Gulf Coast continental margin, in M. P. A. Jackson, D. G. Roberts, and S. Snelson, eds., Salt tectonics: A global perspective: American Association of Petroleum Geologists Memoir, v. 65, p. 109–151.

Faulds, J. E., and R. J. Varga, 1998, The role of accommodation zones and transfer zones in the regional segmentation of extended terranes, in J. E. Faulds, and J. H. Stewart, eds., Accommodation zones and transfer zones: The regional segmentation of the Basin and Range province: Geological Society of America Special Paper 323, p. 1-45.

Gibbs, A. D., 1983, Balanced cross-section construction from seismic sections in areas of extensional tectonics: Journal of Structural Geology, v. 5, p. 153-160.

Hudec, M. R. and M.P.A Jackson, 2006, Advance of allochthonous salt sheets in passive margins and orogens: American Association of Petroleum Geologists Bulletin, v. 90, p. 1535-1564.

Morley, C. K., R.A. Nelson, T. L. Patton and S. G. Munn, 1990, Transfer zones in the East African rift system and their relevance to hydrocarbon exploration in rifts: American Association of Petroleum Geologists Bulletin, v. 74, p. 1234-1253.

Petrov, M., A. Talapov, T. Robertson, A. Lebedev, A. Zhilyaev and L. Polonskiy, 1998, Optical 3D digitizers: Bringing life to the virtual world: IEEE Computer Graphics and Applications, v. 18, p. 28-37.

Rowan, M. G., 1993, A systematic technique for the sequential restoration of salt structures: Tectonophysics, v. 228, p. 331-348.

Rowan, M. G., M. P. A. Jackson and B. D. Trudgill, 1999, Salt-related fault families and fault welds in the northern Gulf of Mexico: American Association of Petroleum Geologists Bulletin, v. 83, p. 1454-1484.

Schultz-Ela, D. D., 1991, Practical restoration of extensional cross sections: Geobyte, v. 6, p. 14-23.

Schultz-Ela, D. D., 1992, Restoration of cross-sections to constrain deformation processes of extensional terraines: Marine and Petroleum Geology, v. 9, p. 372-388.

Schuster, D. C., 1995, Deformation of allochthonous salt and evolution of related salt–structural systems, eastern Louisiana Gulf Coast, in M. P. A. Jackson, D. G. Roberts, and S. Snelson, eds., Salt tectonics: a global perspective: American Association of Petroleum Geologists Memoir, v. 65, p. 177-198.

Stude, G. R., 1978, Depositional environments of the Gulf of Mexico South Timbalier Block 54 salt dome and salt dome growth models: Gulf Coast Association of Geological Societies Transactions, v. 28, p. 627-646.

Talbot, C. J., 1995, Molding of salt diapirs by stiff overburden, in M. P. A. Jackson, D. G. Roberts, and S. Snelson, eds., Salt tectonics: a global perspective: American Association of Petroleum Geologists Memoir, v. 65, p. 61-75.

Vendeveille, B., 1987, Champs de failles et tectonique en extension: Modelisation experimentale,Memoires et Documents du Centre d'eude structurale des socles, No. 15, Rennes Cedex, France, 395 p.

Weijermars, R., M. P. A. Jackson, and B. C. Vendeville, 1993, Rheological and tectonic modeling of salt provinces: Tectonophysics, v. 217, p. 143– 174.

Withjack, M.O and S. Callaway, 2000, Active normal faulting beneath a salt layer: An experimental study of deformation pattern in the cover sequence: American Association of Petroleum Geologists Bulletin, v. 84, p. 627-651.

Worrall, D. M., and M. Snelson, 1989, Evolution of the 764 northern Gulf of Mexico, with emphasis on Cenozoic 765 growth faulting and the role of salt, in A. W. Bally and 766 A. R. Palmer, eds., The geology of North America: An overview: Geological Society of America Decade of 768 North American Geology, v. A, p. 97‑138.

Figure Captions

Figure 2.1: Tectono-stratigraphic provinces in the northern Gulf of Mexico and the location of ST 54 with respect to the framework (Modified from Diegel et. al., 1995).

Figure 2.2: Distribution of salt bodies in the shelf region of offshore Louisiana and the linked system of faults connecting the different salt structures (Modified from Lafayette Geological Society Publication, 1973).

Figure 2.3: Schematic diagram of the previous models of evolution of the Roho System and the Stepped Counterregional System from the same precursor salt canopy (Modified from Schuster, 1995).

Figure 2.4: Generalized stratigraphic column of the ST 54 area (Modified from Stude, 1978).

Figure 2.5: Variance time slice with structural smoothening at 2000 ms enabling the display the fault traces and terminations which were used while interpreting faults.

Figure 2.6: Location of the six inlines chosen for restoration that are perpendicular to the major fault trends.

Figure 2.7: Time-Depth plot obtained from 5 checkshots in the ST54 area.

Figure 2.8: Figure shows the velocity model used to convert time sections to depth with a background velocity applied according to the time velocity equation and a constant velocity of 1850 ft/sec applied to the salt body.

Figure 2.9: Interpreted depth converted seismic sections of (a) Inline 32, (b) Inline 82, (c) Inline 102, (d) Inline 132, (e) Inline 152 and (f) Inline 192. Horizons are color coded according to stratigraphy in Figure 2.4 and salt welds are indicated by double dots above and below the weld.

Figure 2.10: Depth surfaces created from depth converted time surfaces fitted to well tops and balanced cross sections for (a) Top of C Sand and (b) Top of F Sand. Fault gaps indicate displacement along normal faults. The surfaces indicate accurate structural variations and fault displacements that increase with depth.

Figure 2.11: (a) Structural relationship and present geometry of the regional and counterregional faults with respect to the salt uplift. The faults lose displacement and terminate above the salt high while towards the north and south, the salt forms welds. (b) Structural position of the salt beneath the F Sand surface indicating the location of the salt beneath the transfer zone.

Figure 2.12: Kinematic restoration of Inline 82 assuming the process of downbuilding. The restoration is shown up to the top of D Sand to essentially demonstrate the large amount of salt moving out of the section. Arrows indicate salt evacuation out of the section.

Figure 2.13: Method for balancing areas in the center of the section that are pierced by salt. On the right, the figure shows the shapes of the pierced fault blocks that have changed due to thinning of units during restoration, although the areas are balanced.

Figure 2.14: Kinematic restoration of Inline 32 by sequential removal of units and application of decompaction. Restored faults are marked in red and direction of salt evacuation is shown right before salt welds have formed.

Figure 2.15: Kinematic restoration of Inline 192 by sequential removal of units and application of decompaction. Restored faults are marked in red and direction of salt evacuation is shown right before salt welds have formed.

Figure 2.16: Kinematic restoration of Inline 82 by sequential removal of units and application of decompaction. Restored faults are marked in red and direction of salt evacuation is shown right before salt welds have formed.

Figure 2.17: Kinematic restoration of Inline 102 by sequential removal of units and application of decompaction. Restored faults are marked in red and direction of salt evacuation is shown right before salt welds have formed.

Figure 2.18: Kinematic restoration of Inline 132 by sequential removal of units and application of decompaction. Restored faults are marked in red and direction of salt evacuation is shown right before salt welds have formed.

Figure 2.19: Kinematic restoration of Inline 152 by sequential removal of units and application of decompaction. Restored faults are marked in red and direction of salt evacuation is shown right before salt welds have formed.

Figure 2.20: Experimental setup for the clay model with the bent base plate dipping by an angle of 5° on two sides. The clay is overlain on top of this setup with the silicone polymer underlying the clay cake and distributed in the shape shown in the figure.

Figure 2.21: 3D model of the top of the clay surface at the (a) initial, (b) middle and (c) final stage. The fault dips are annotated on the clay surface and the orientation of the surface is the same as shown in the setup. Locations of schematic cross sections of next figure are shown in (c). (d) The contoured surface of the top of the silicone polymer indicating structural high above the basal hinge. (e) Isochore surface for the top of the silicone polymer indicating thicker silicone above the basal hinge.

Figure 2.22: (a) Schematic cross section across the clay where silicone polymer is absent on the left slope. The polymer forms highs in the footwall of the faults. (b) Schematic

cross section across the clay model where silicone polymer is present on both slopes. The polymer forms a high above the basal hinge. Locations of cross sections are shown in Figure 2.21 c. (c) Possible evolutionary process of the collapsed crestal structure. Dotted line indicates the original geometry of the top of the silicone polymer and as the structure evolves, the silicone from the two slopes migrate towards the basal hinge to form a structural high while lows form in areas immediately adjacent to the hinge.

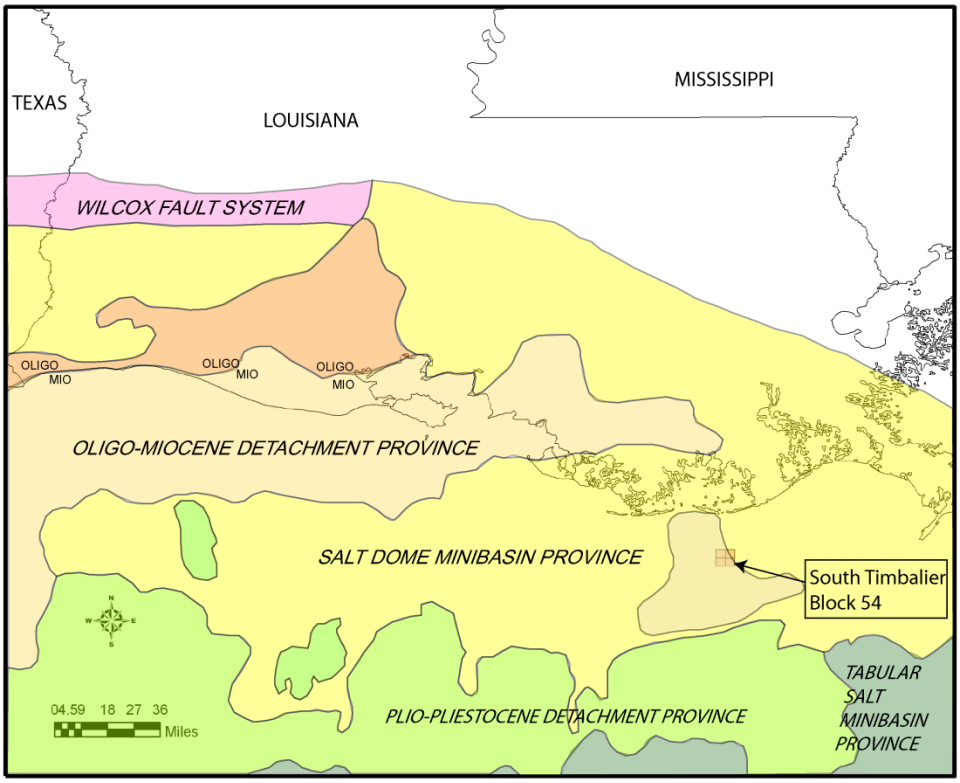

Figure 2.1: Tectono-stratigraphic provinces in the northern Gulf of Mexico and the location of ST 54 with respect to the framework (Modified from Diegel et. al., 1995).

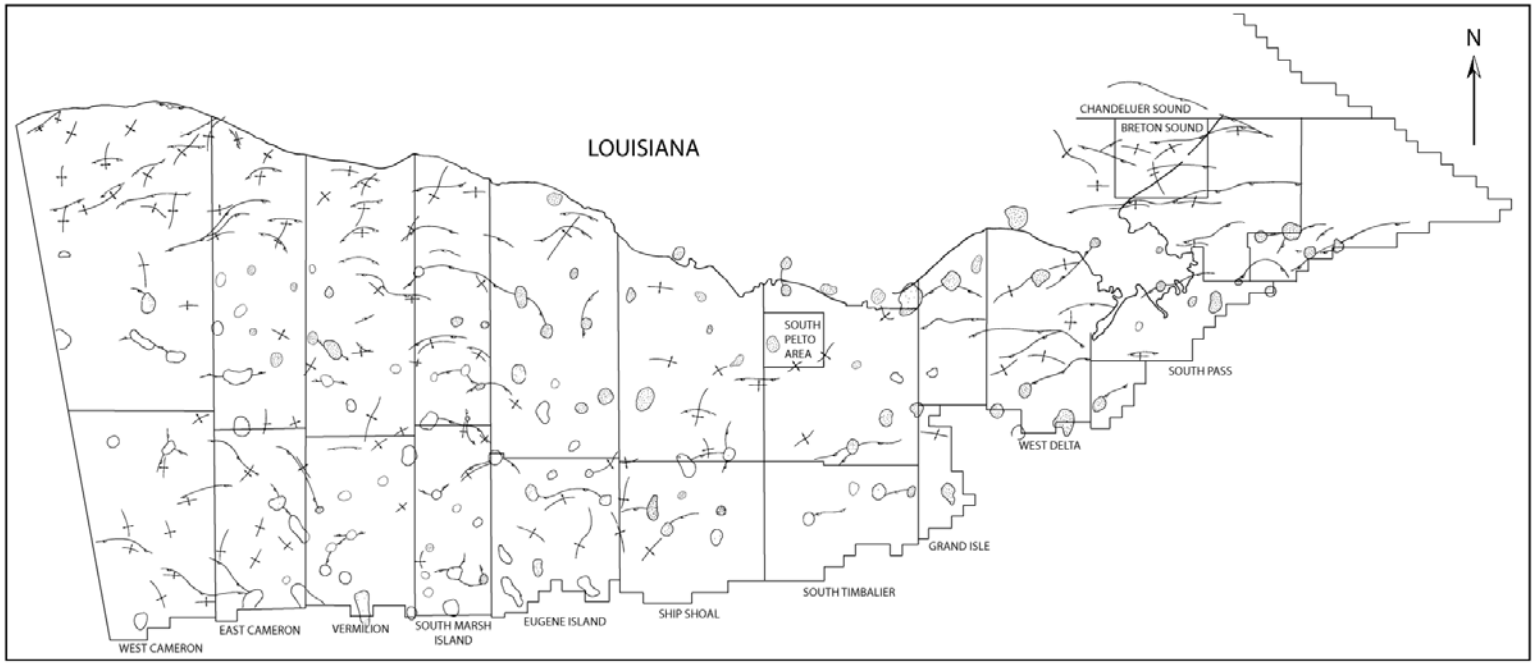

Figure 2.2: Distribution of salt bodies in the shelf region of offshore Louisiana and the linked system of faults connecting the different salt structures (Modified from Lafayette Geological Society Publication, 1973).

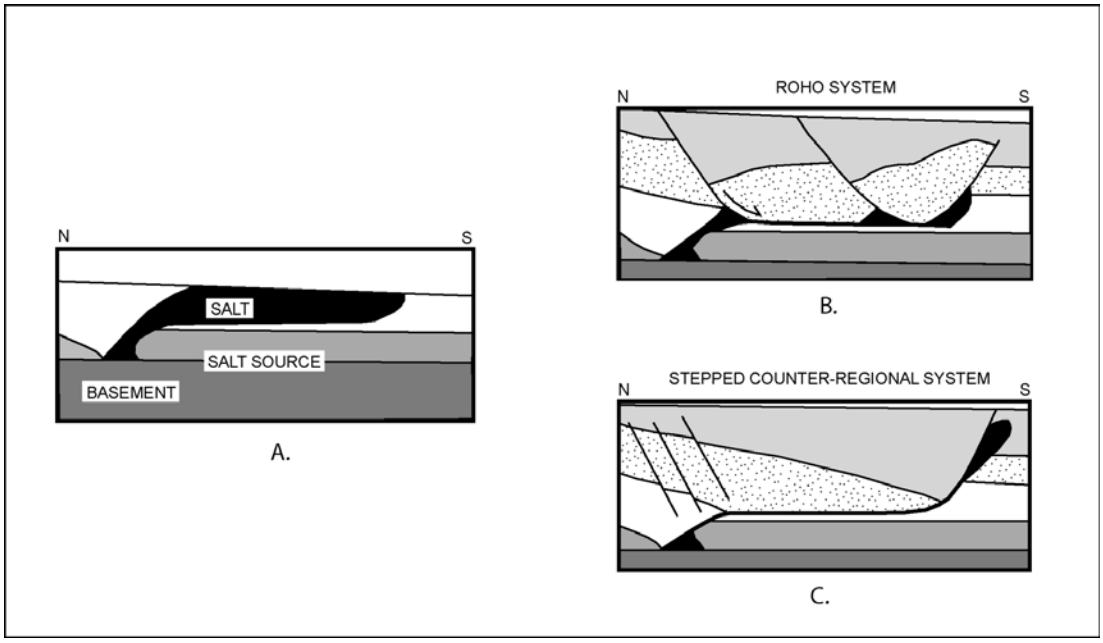

Figure 2.3: Schematic diagram of the previous models of evolution of the Roho System and the Stepped Counterregional System from the same precursor salt canopy (Modified from Schuster, 1995).

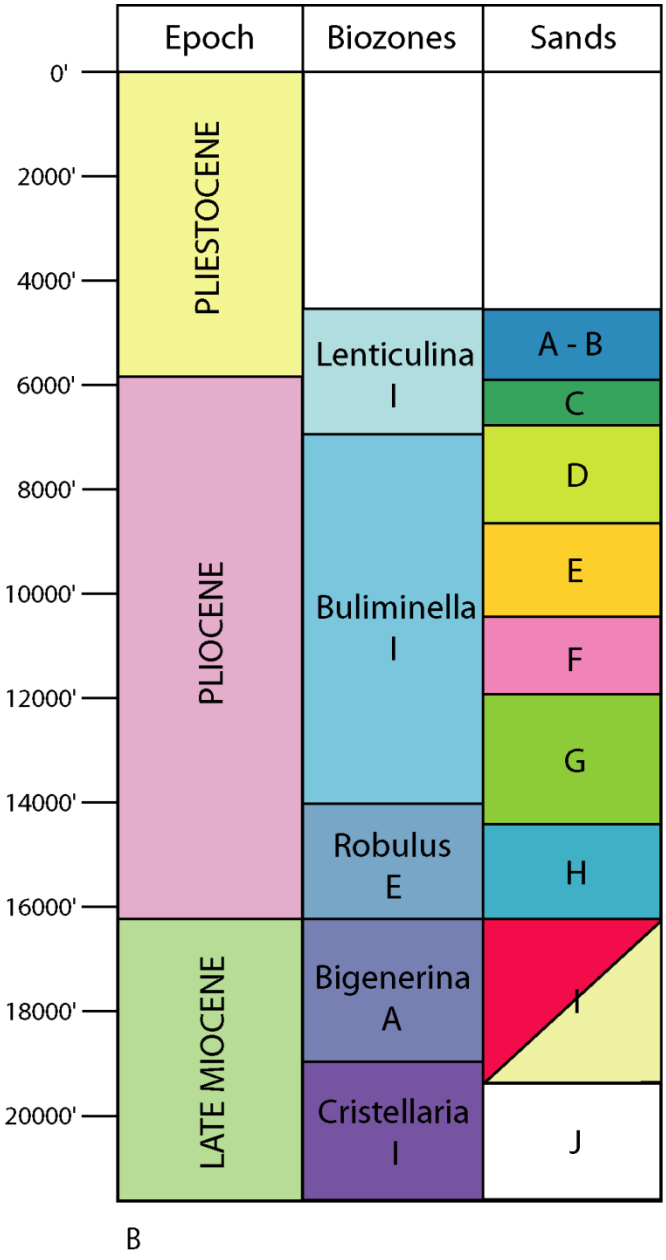

Figure 2.4: Generalized stratigraphic column of the ST 54 area (Modified from Stude, 1978).

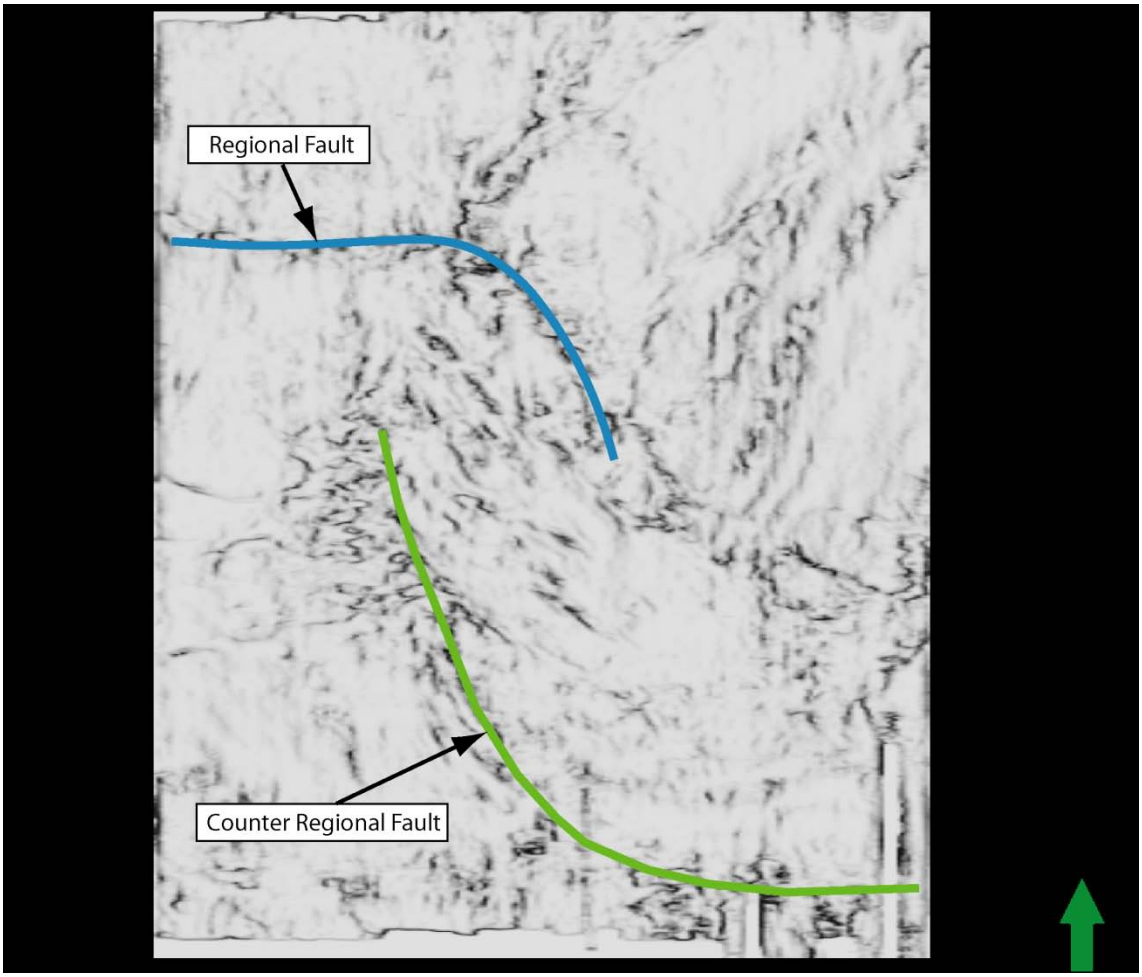

Figure 2.5: Variance time slice with structural smoothening at 2000 ms enabling the display the fault traces and terminations which were used while interpreting faults.

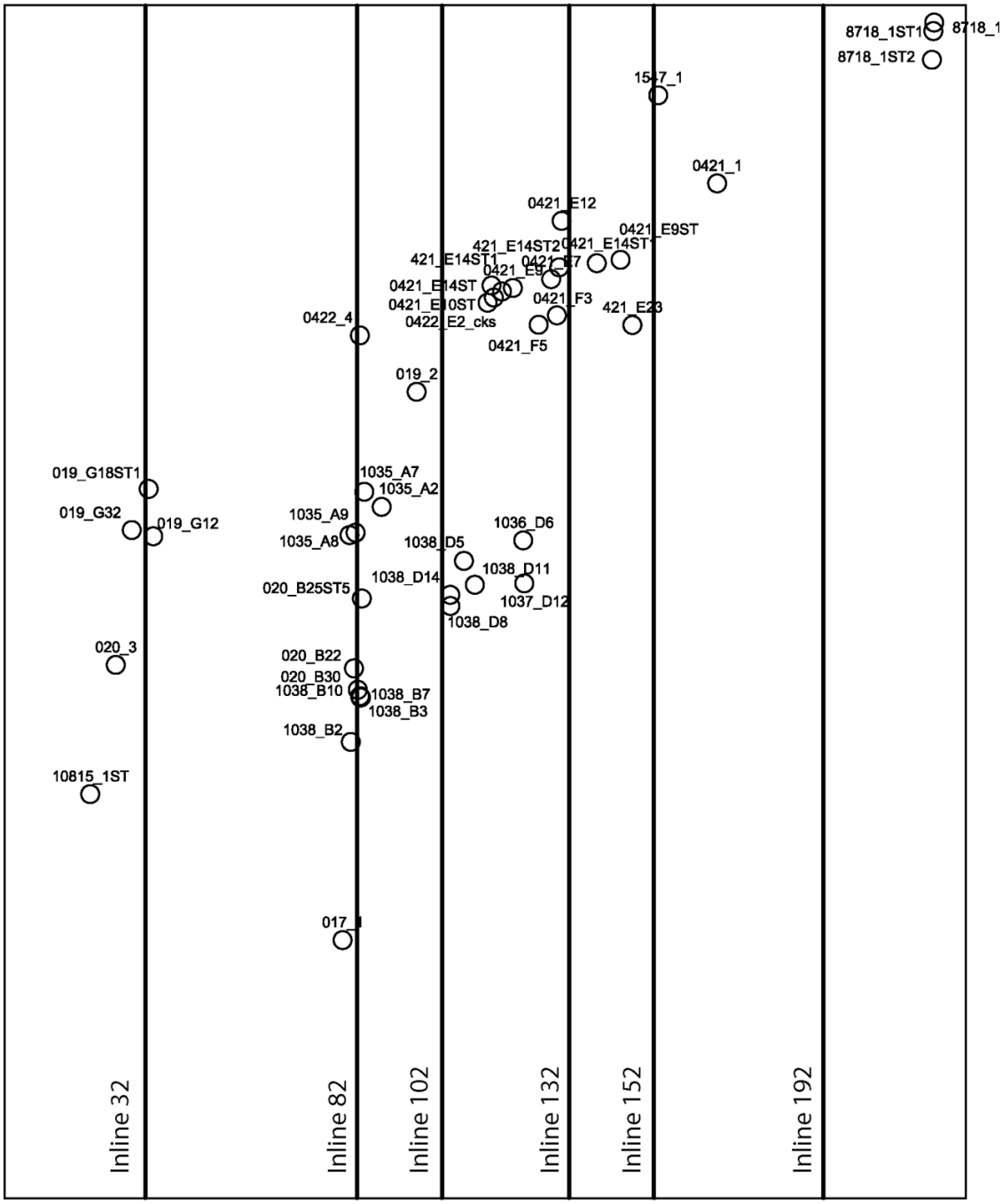

Figure 2.6: Location of the six inlines chosen for restoration that are perpendicular to the major fault trends.

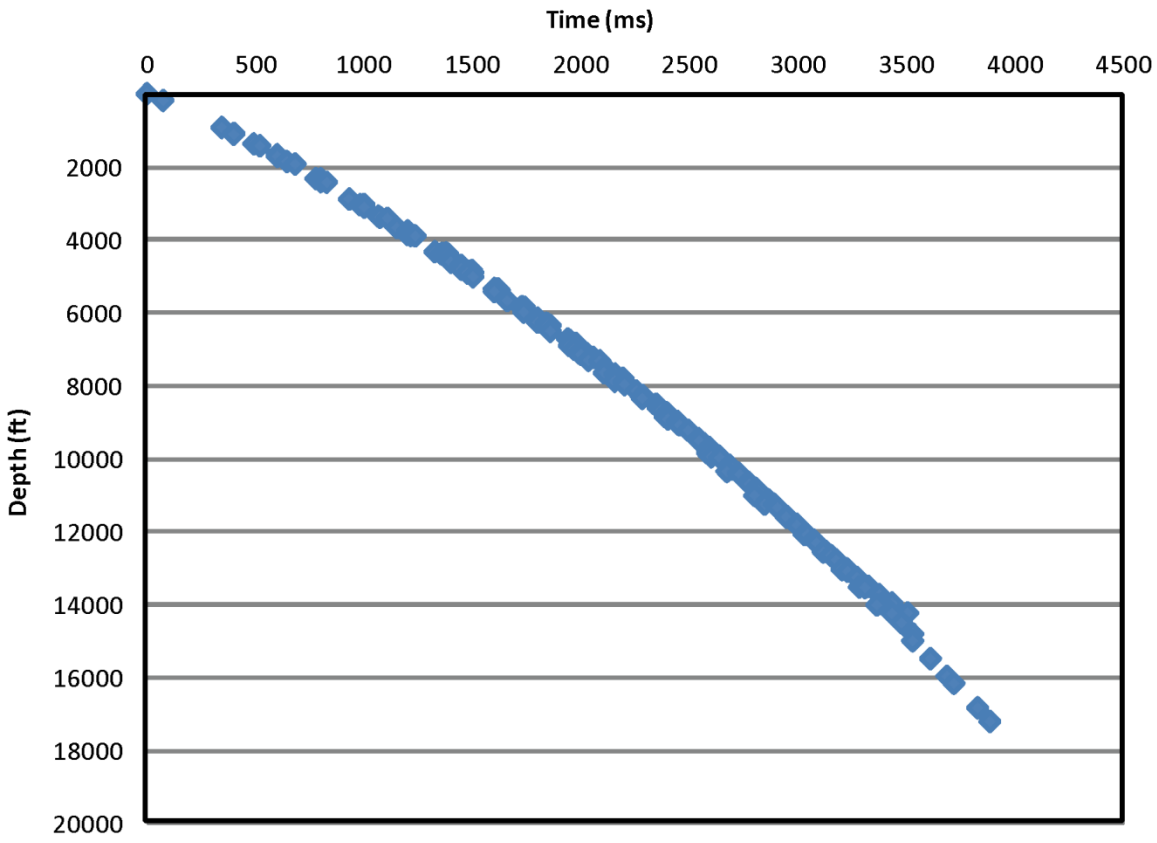

Figure 2.7: Time-Depth plot obtained from 5 checkshots in the ST54 area.

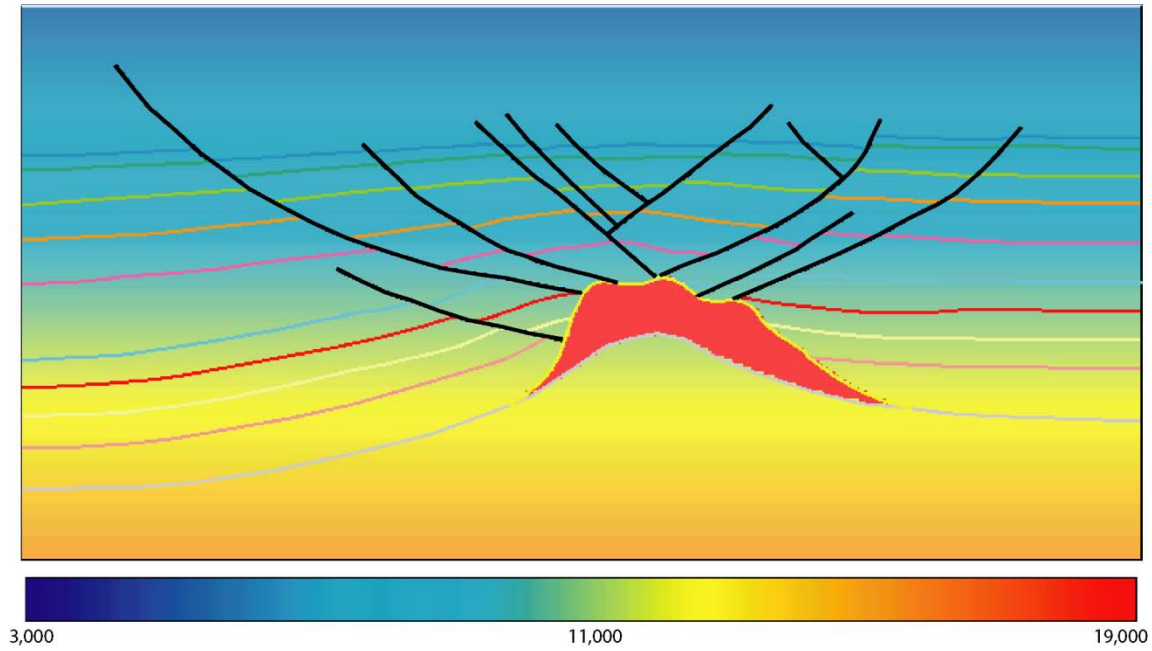

Figure 2.8: Figure shows the velocity model used to convert time sections to depth with a background velocity applied according to the time velocity equation and a constant velocity of 1850 ft/sec applied to the salt body.

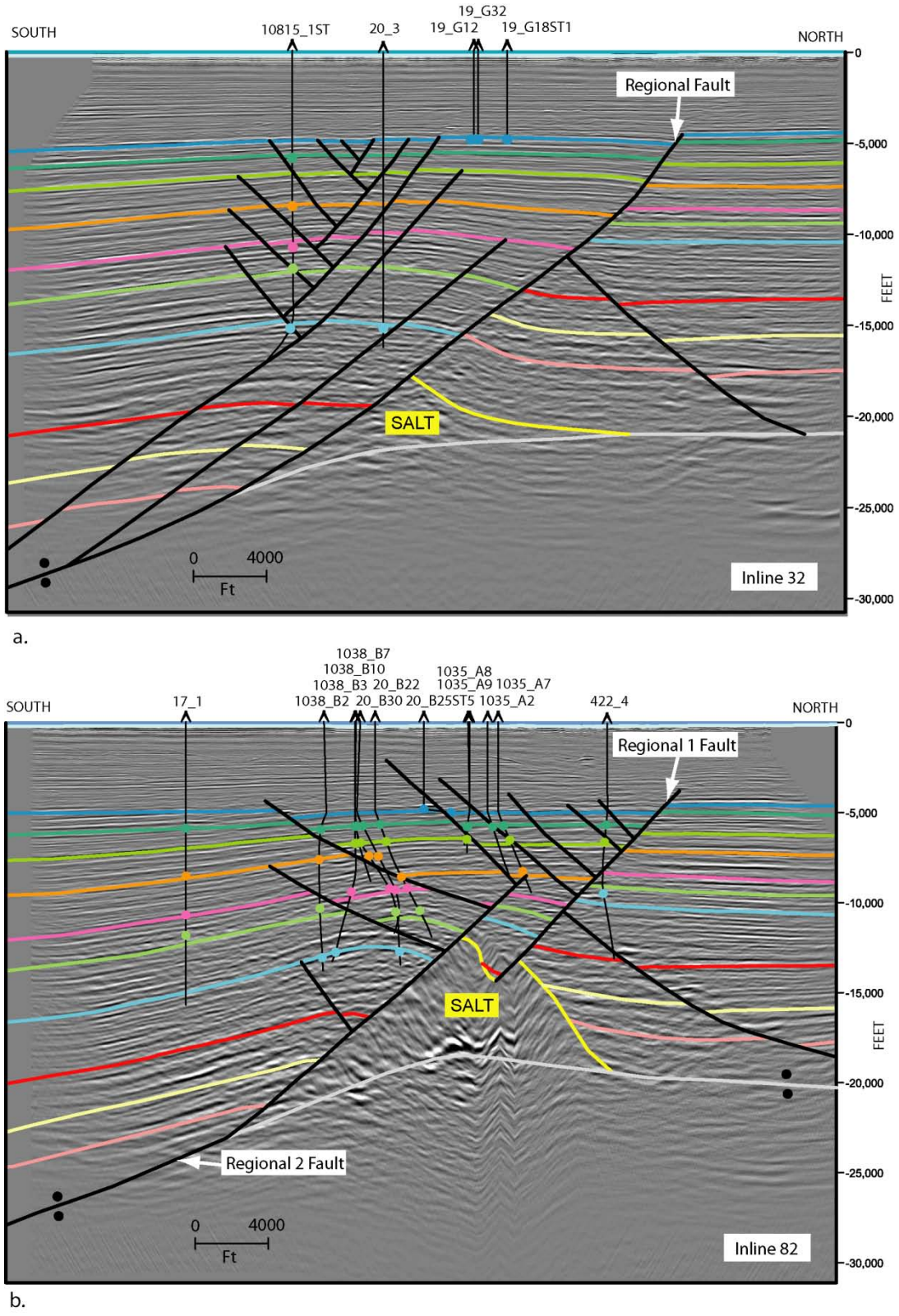

Figure 2.9: Interpreted depth converted seismic sections of (a) Inline 32, (b) Inline 82, (c) Inline 102, (d) Inline 132, (e) Inline 152 and (f) Inline 192. Horizons are color coded according to stratigraphy in Figure 2.4 and salt welds are indicated by double dots above and below the weld.

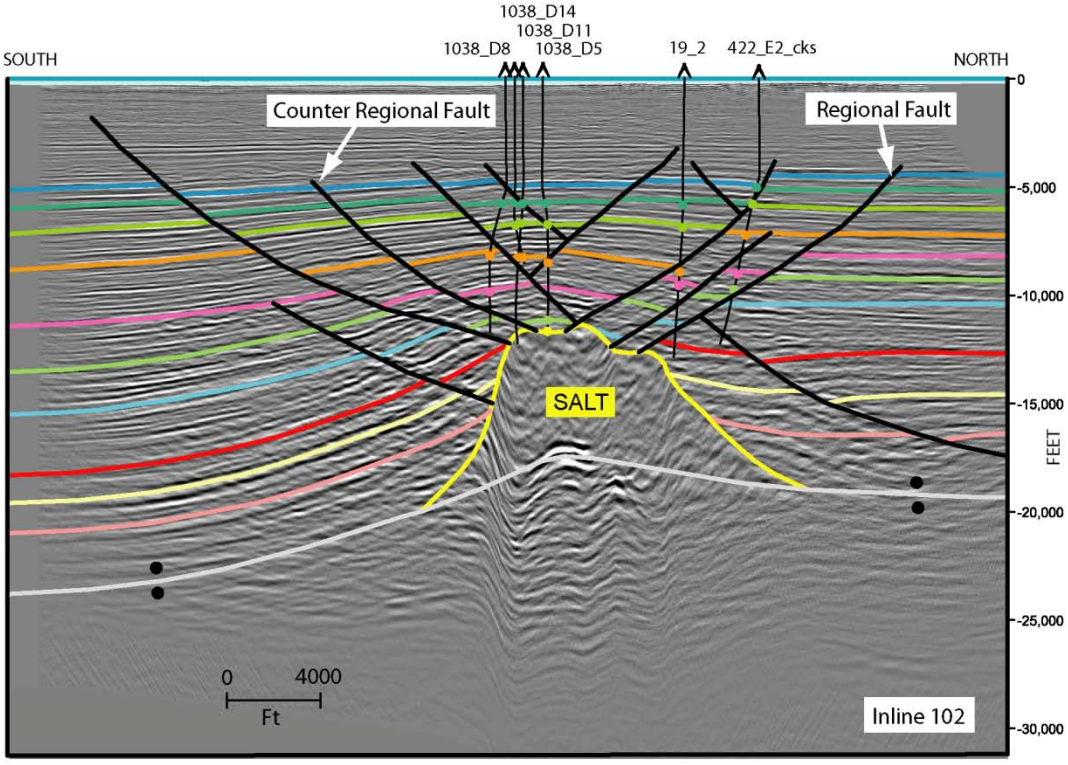

c.

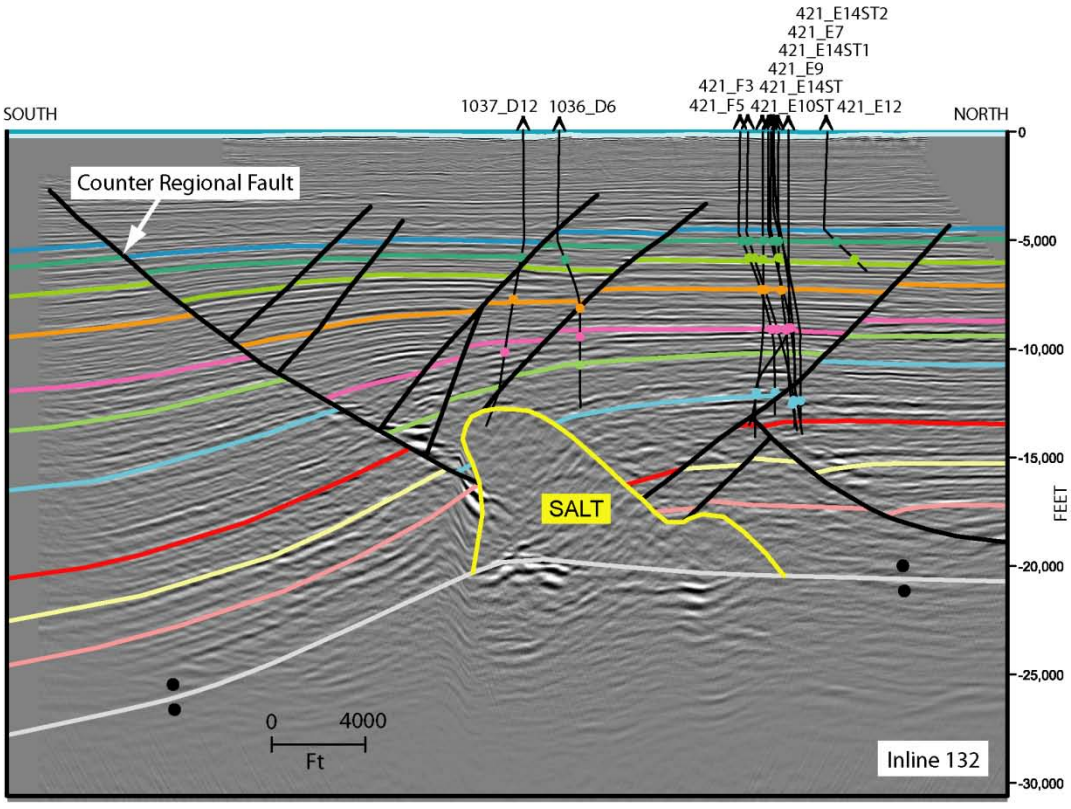

d.

Figure 2.9 (*Continued*)

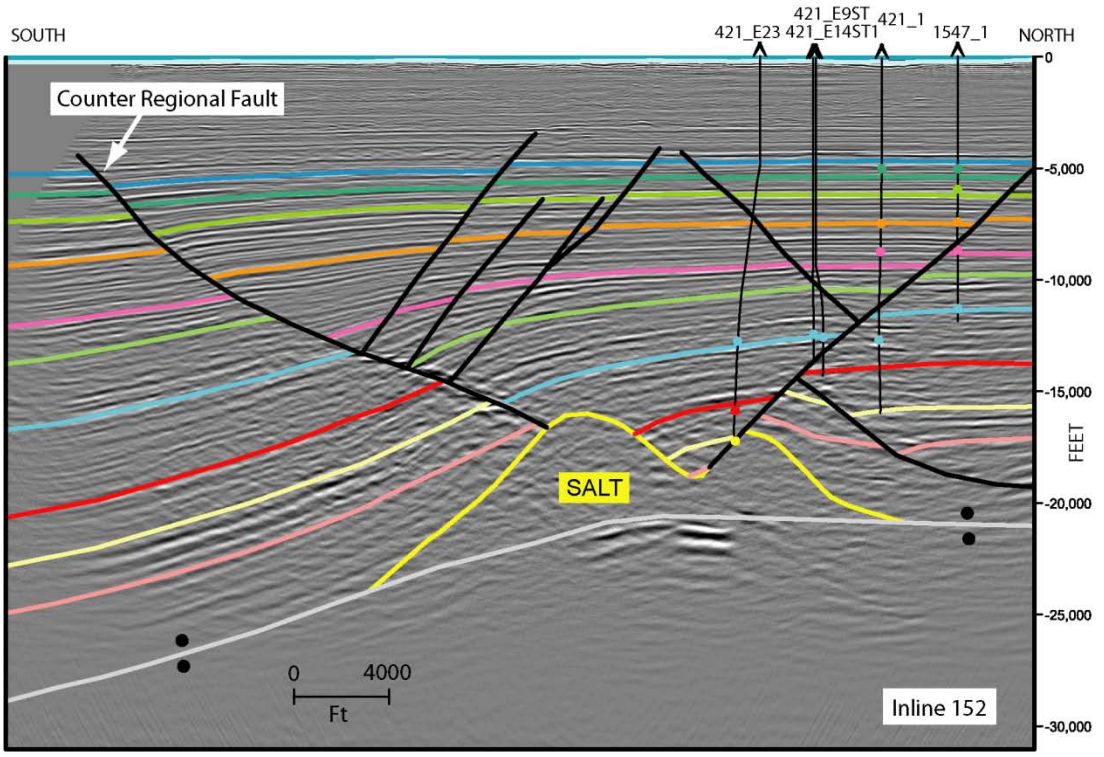

e.

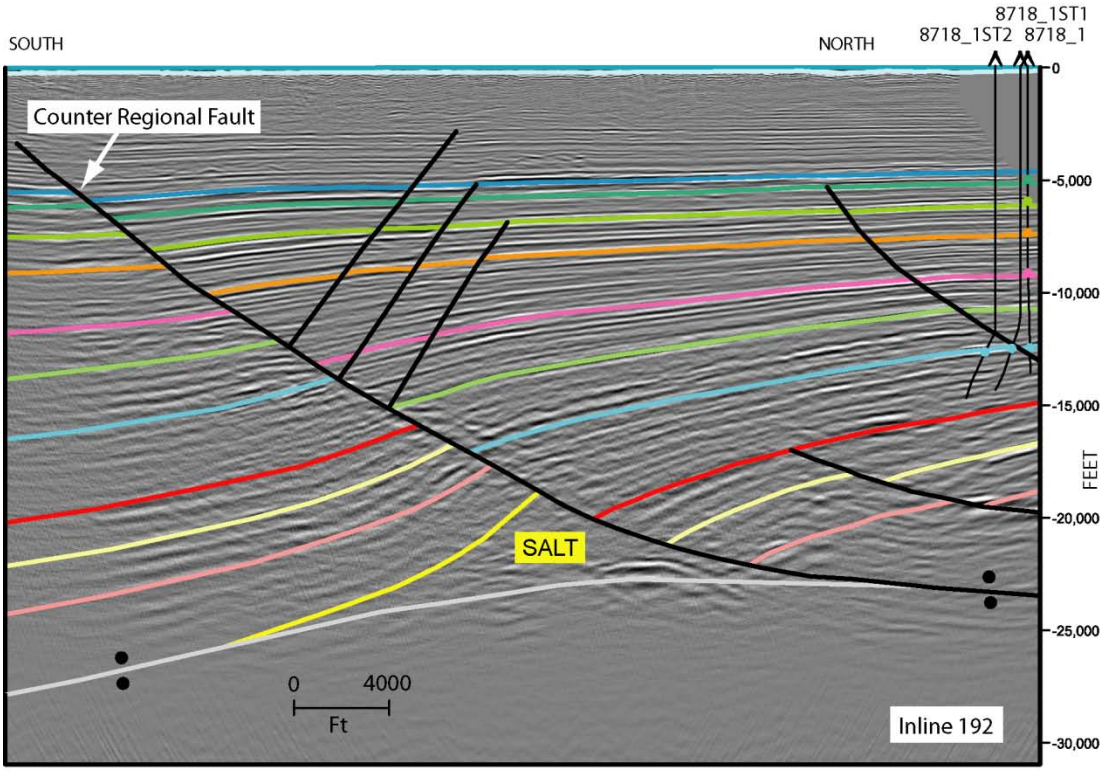

f.

Figure 2.9 (*Continued*)

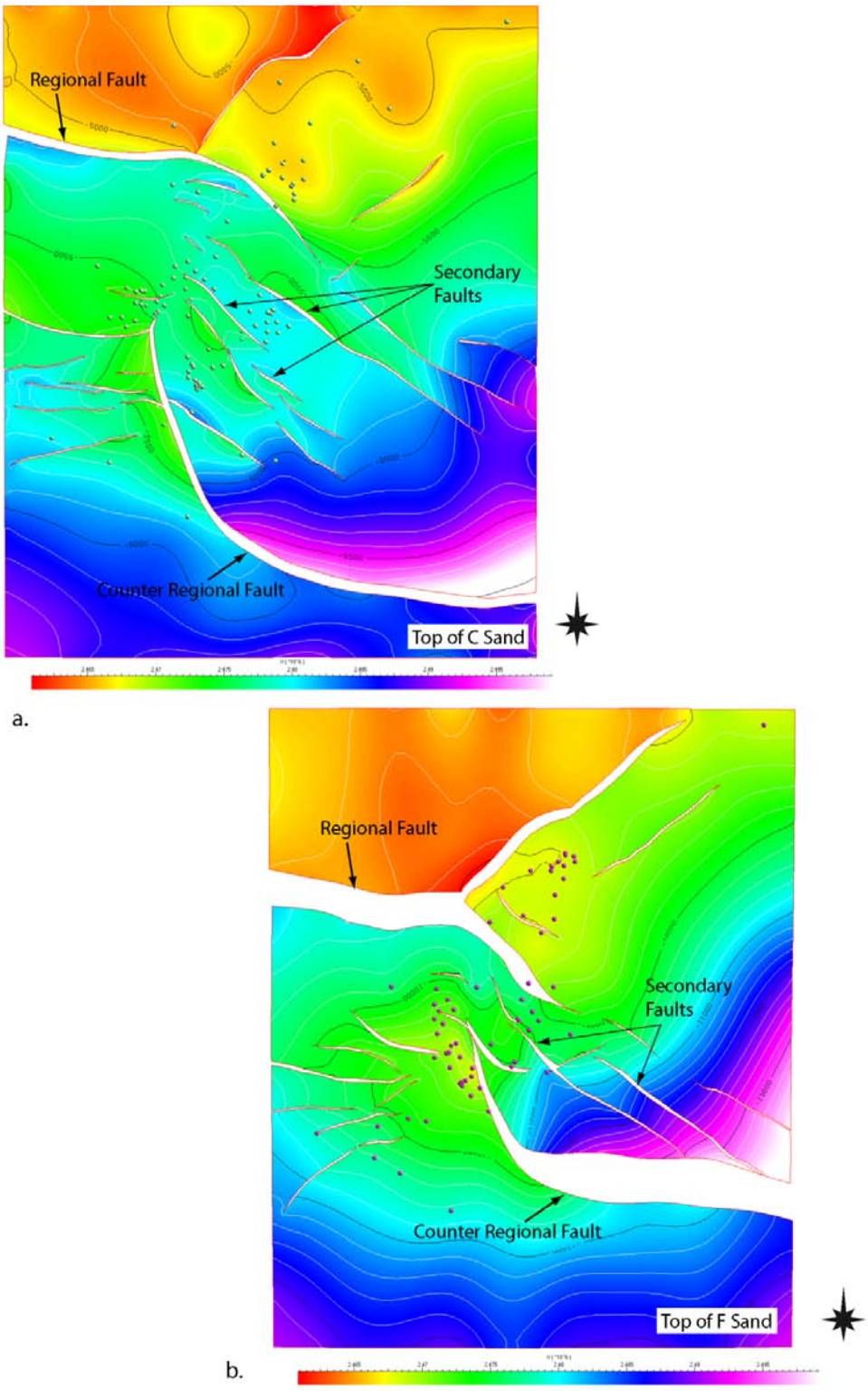

Figure 2.10: Depth surfaces created from depth converted time surfaces fitted to well tops and balanced cross sections for (a) Top of C Sand and (b) Top of F Sand. Fault gaps indicate displacement along normal faults. The surfaces indicate accurate structural variations and fault displacements that increase with depth.

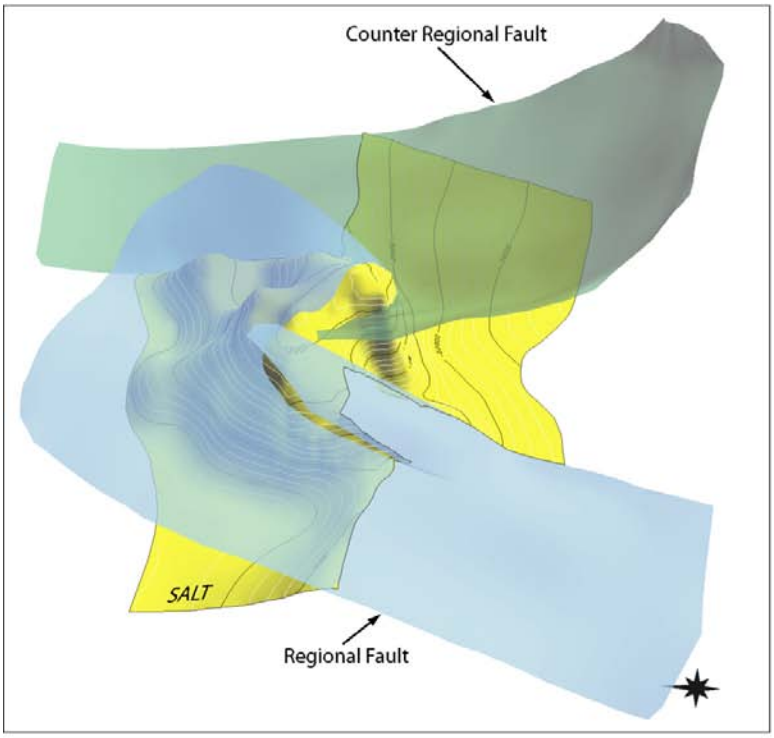

a.

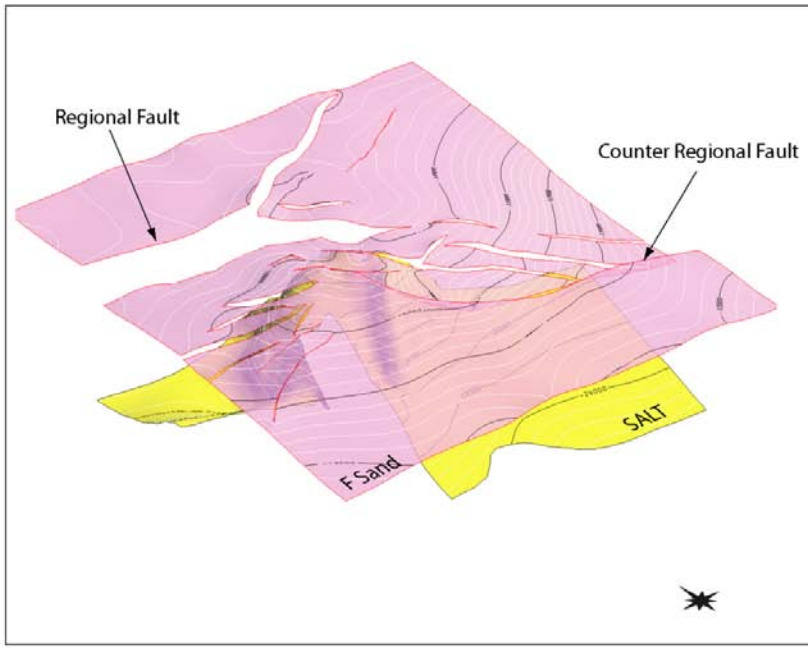

b.

Figure 2.11: (a) Structural relationship and present geometry of the regional and counterregional faults with respect to the salt uplift. The faults lose displacement and terminate above the salt high while towards the north and south, the salt forms welds. (b) Structural position of the salt beneath the F Sand surface indicating the location of the salt beneath the transfer zone.

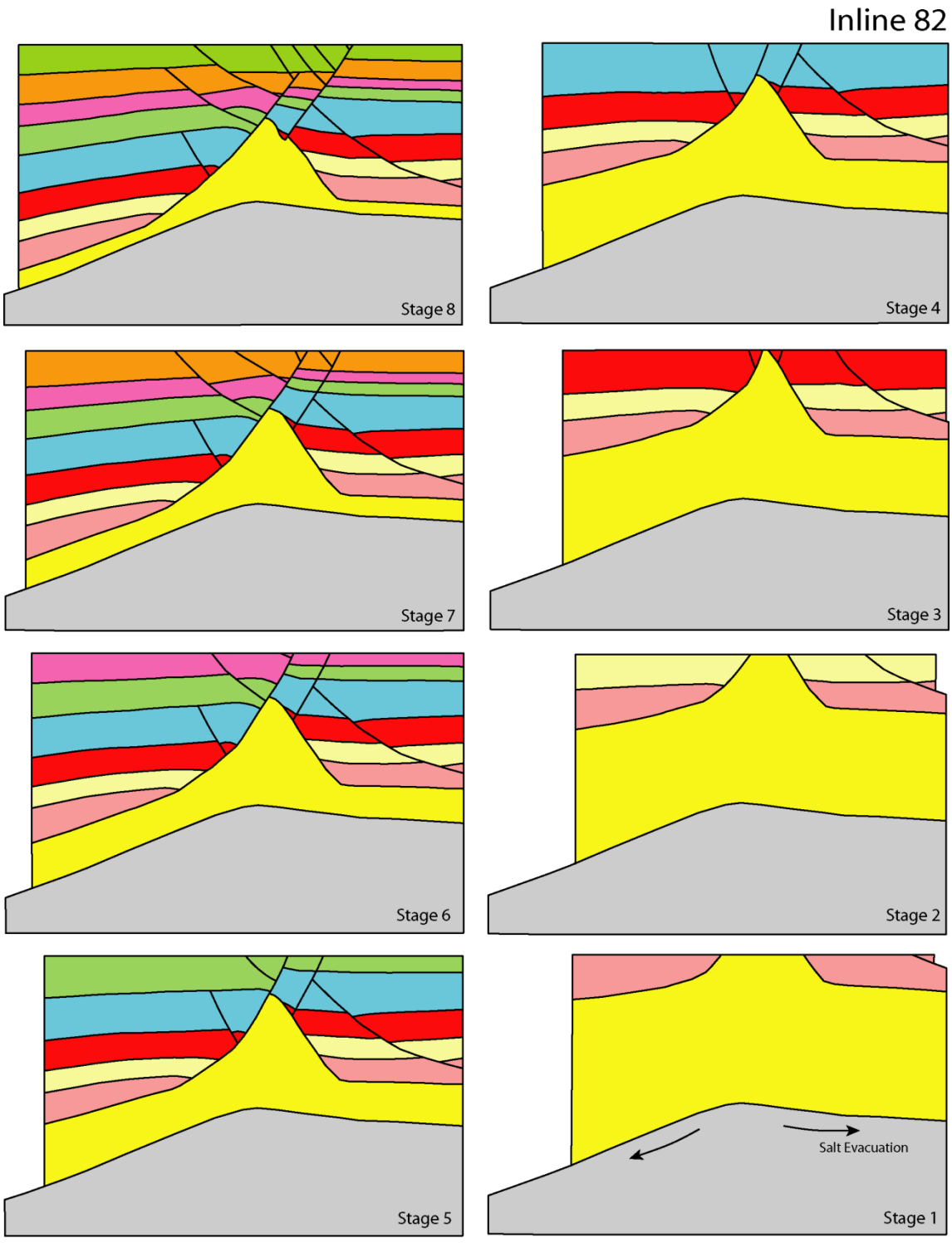

Figure 2.12: Kinematic restoration of Inline 82 assuming the process of downbuilding. The restoration is shown up to the top of D Sand to essentially demonstrate the large amount of salt moving out of the section. Arrows indicate salt evacuation out of the section.

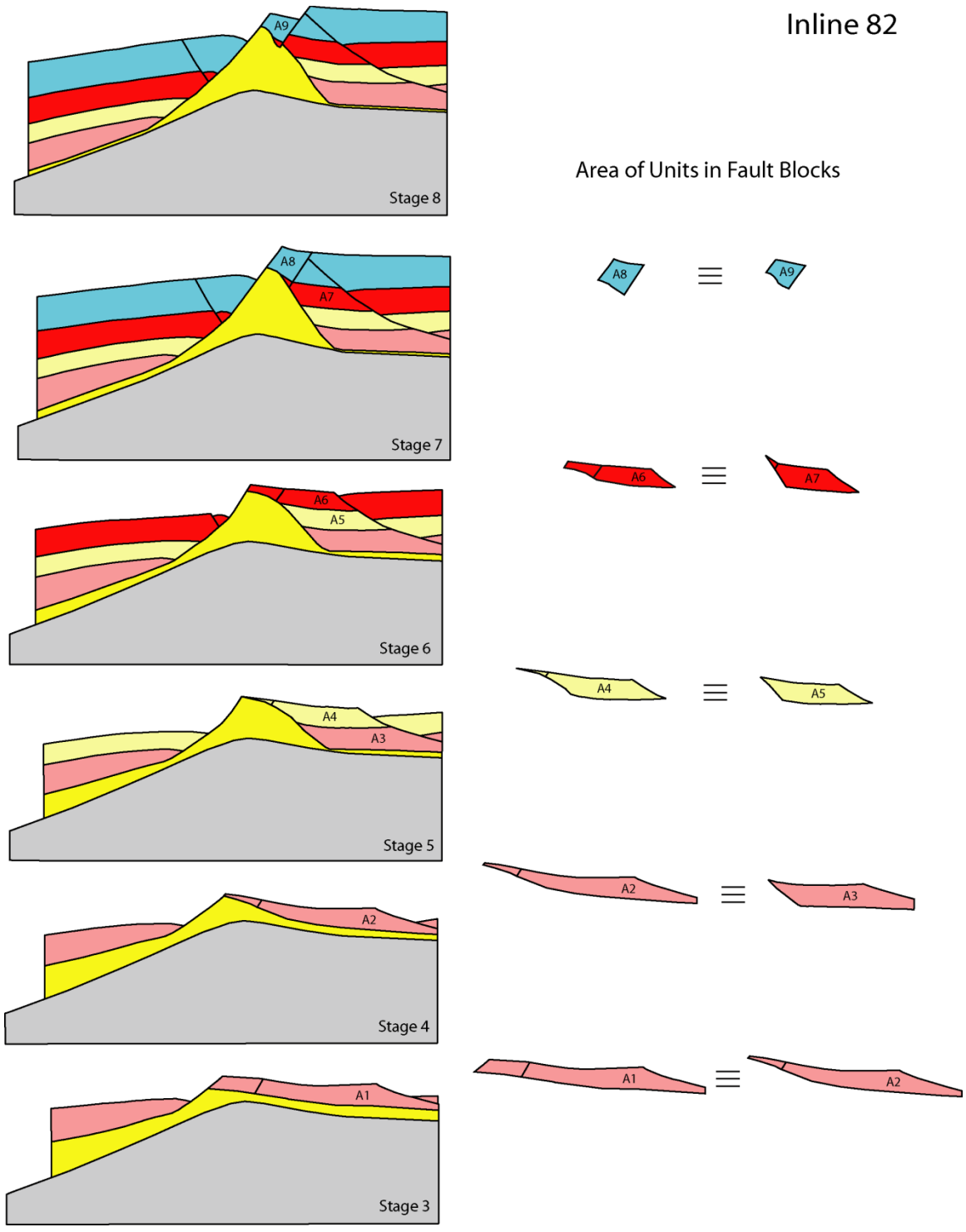

Figure 2.13: Method for balancing areas in the center of the section that are pierced by salt. On the right, the figure shows the shapes of the pierced fault blocks that have changed due to thinning of units during restoration, although the areas are balanced.

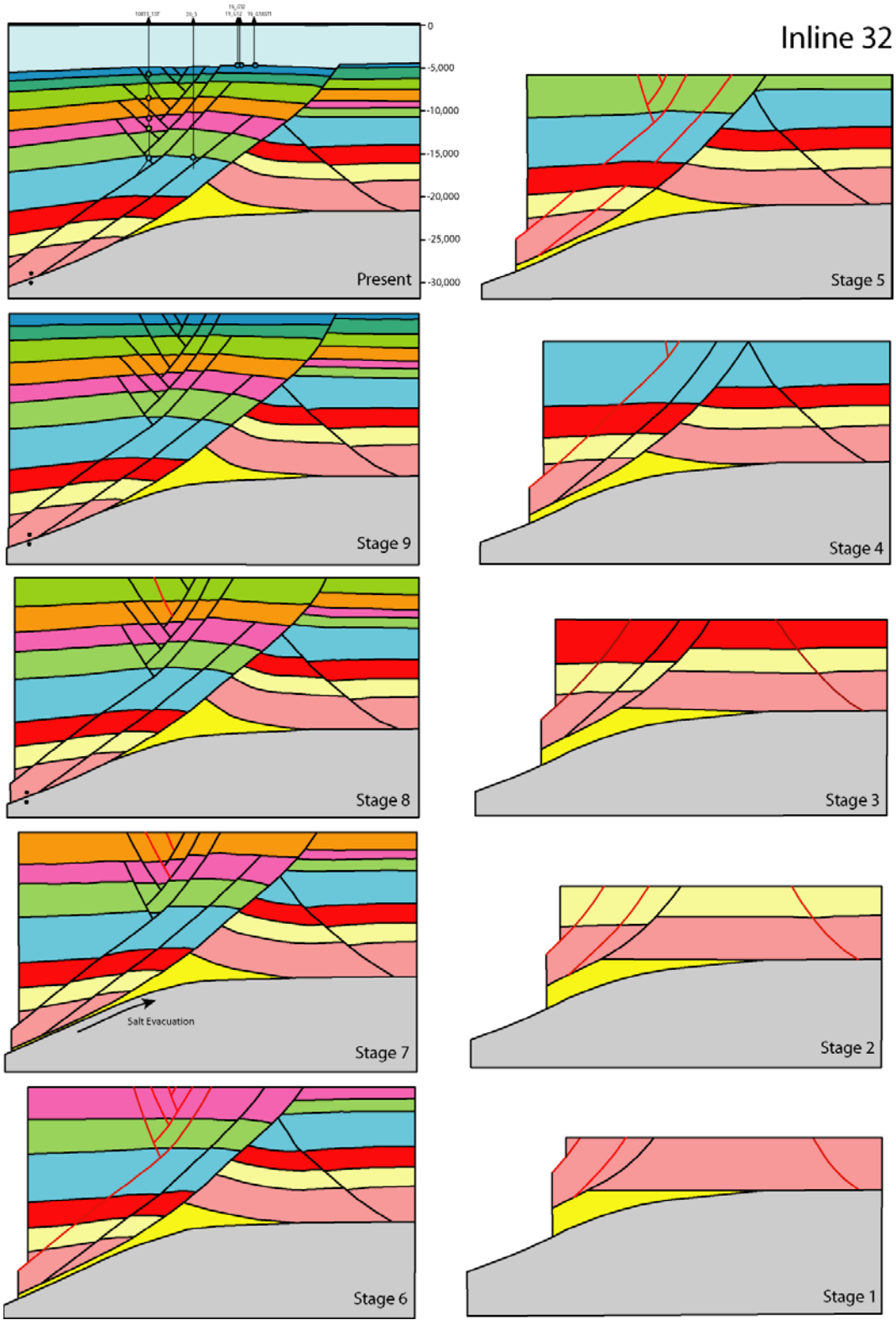

Figure 2.14: Kinematic restoration of Inline 32 by sequential removal of units and application of decompaction. Restored faults are marked in red and direction of salt evacuation is shown right before salt welds have formed.

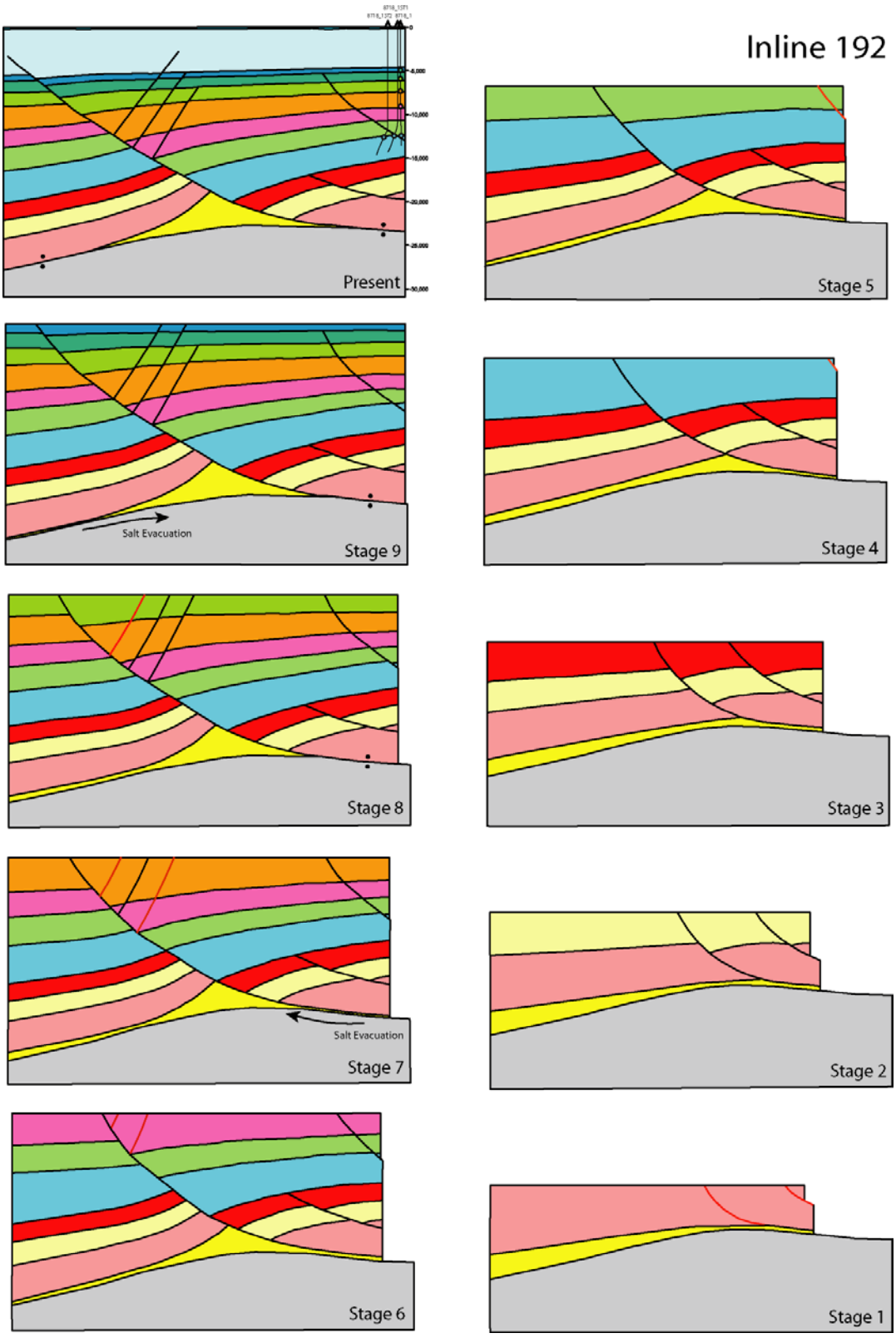

Figure 2.15: Kinematic restoration of Inline 192 by sequential removal of units and application of decompaction. Restored faults are marked in red and direction of salt evacuation is shown right before salt welds have formed.

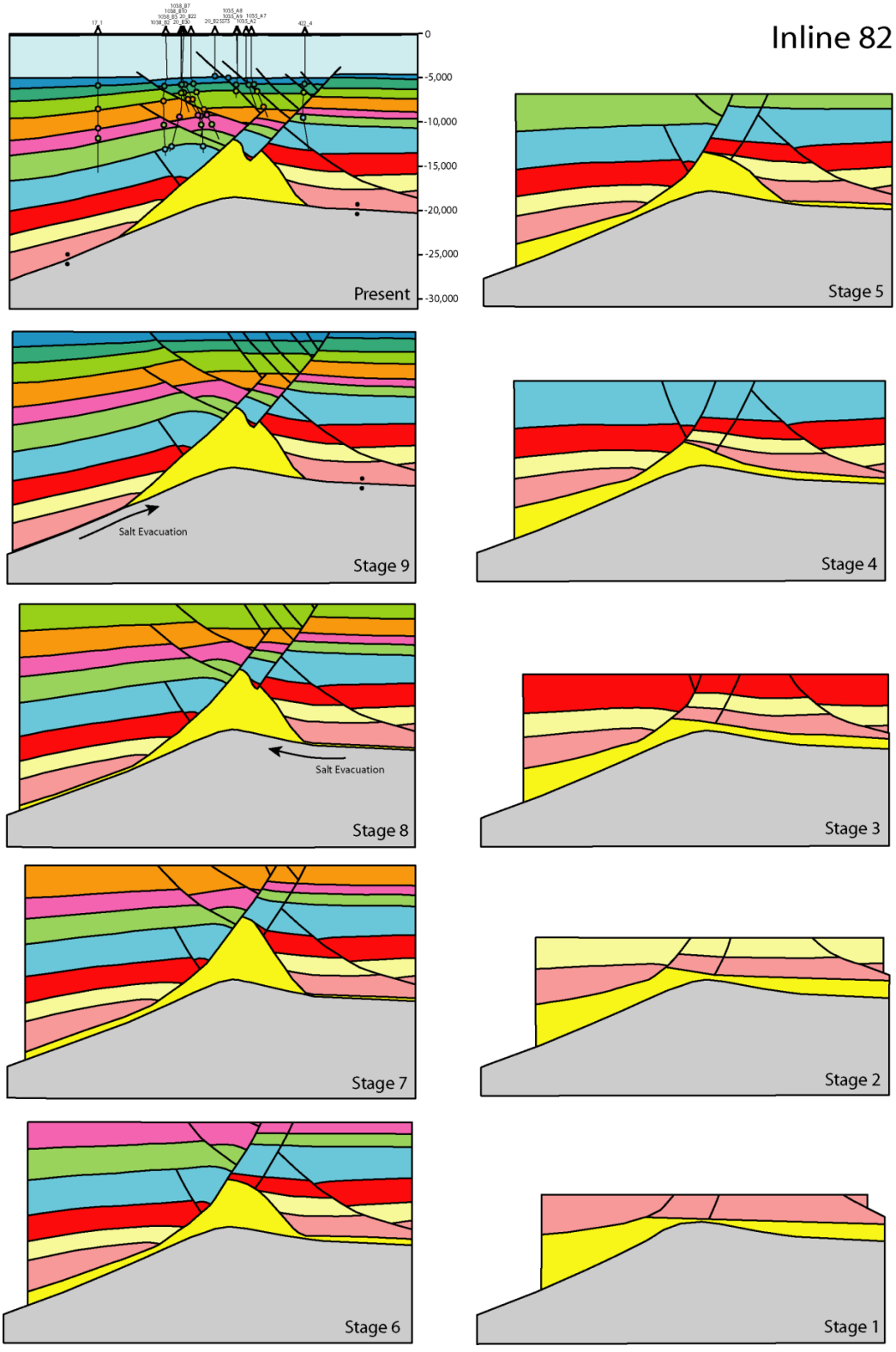

Figure 2.16: Kinematic restoration of Inline 82 by sequential removal of units and application of decompaction. Restored faults are marked in red and direction of salt evacuation is shown right before salt welds have formed.

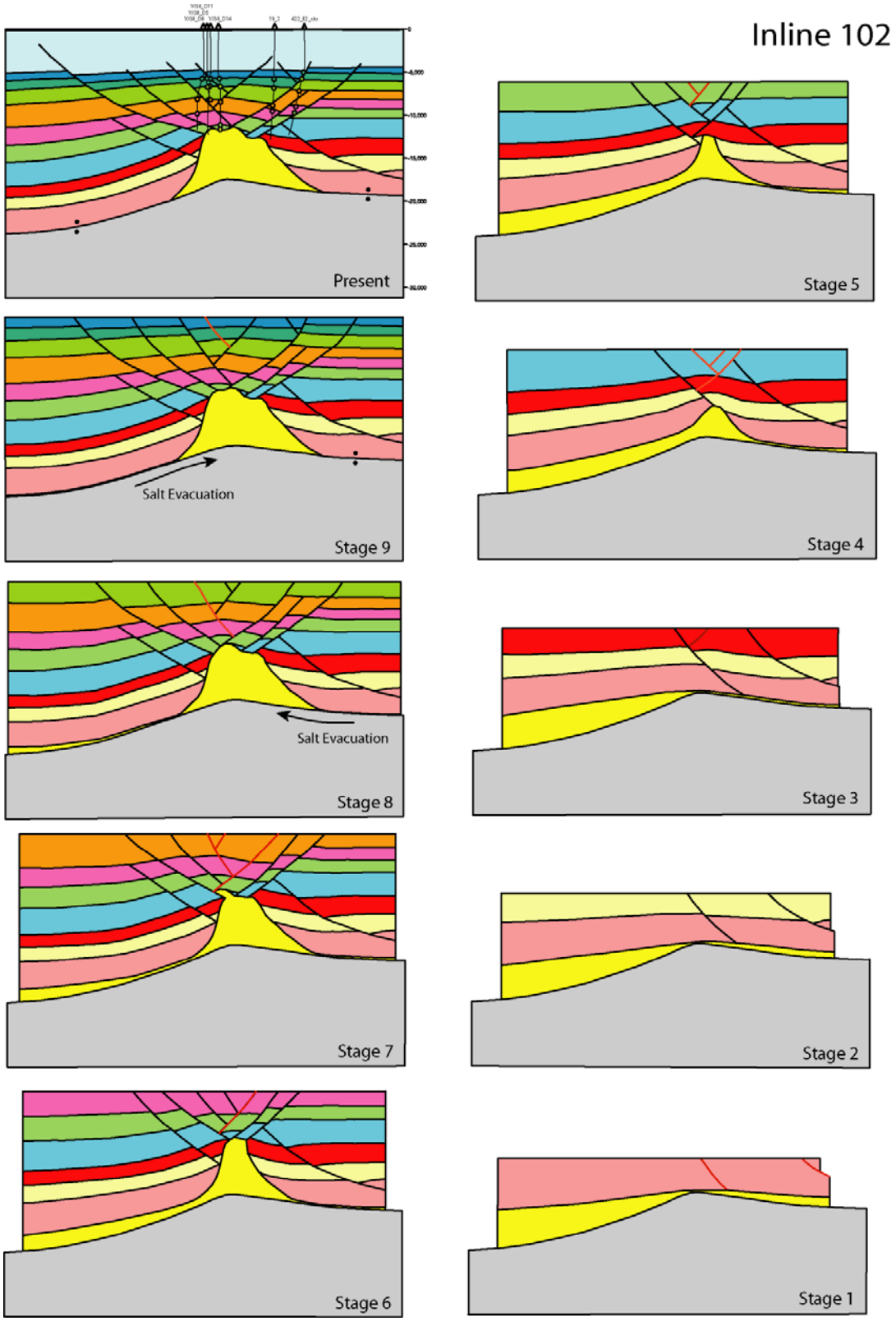

Figure 2.17: Kinematic restoration of Inline 102 by sequential removal of units and application of decompaction. Restored faults are marked in red and direction of salt evacuation is shown right before salt welds have formed.

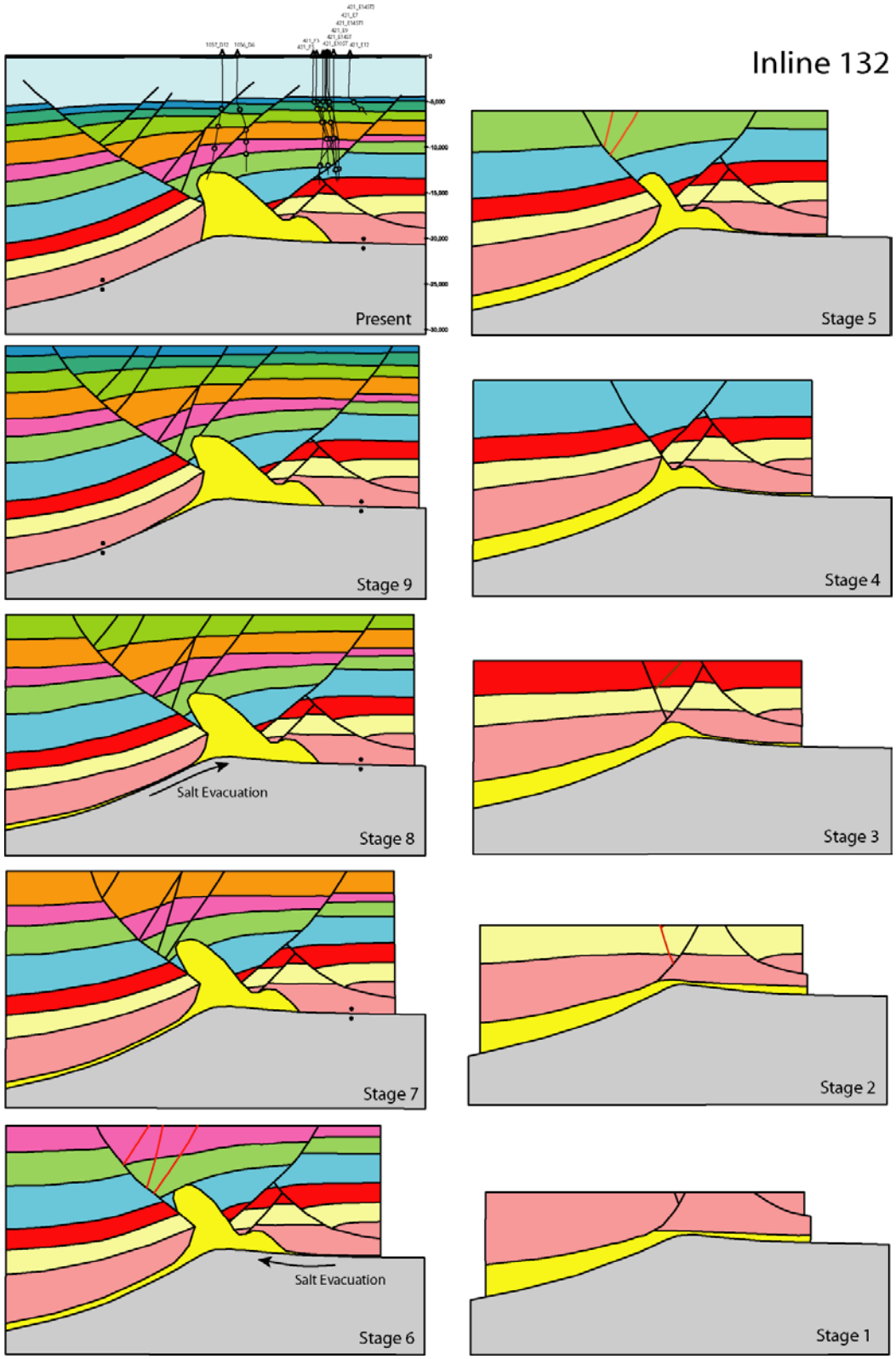

Figure 2.18: Kinematic restoration of Inline 132 by sequential removal of units and application of decompaction. Restored faults are marked in red and direction of salt evacuation is shown right before salt welds have formed.

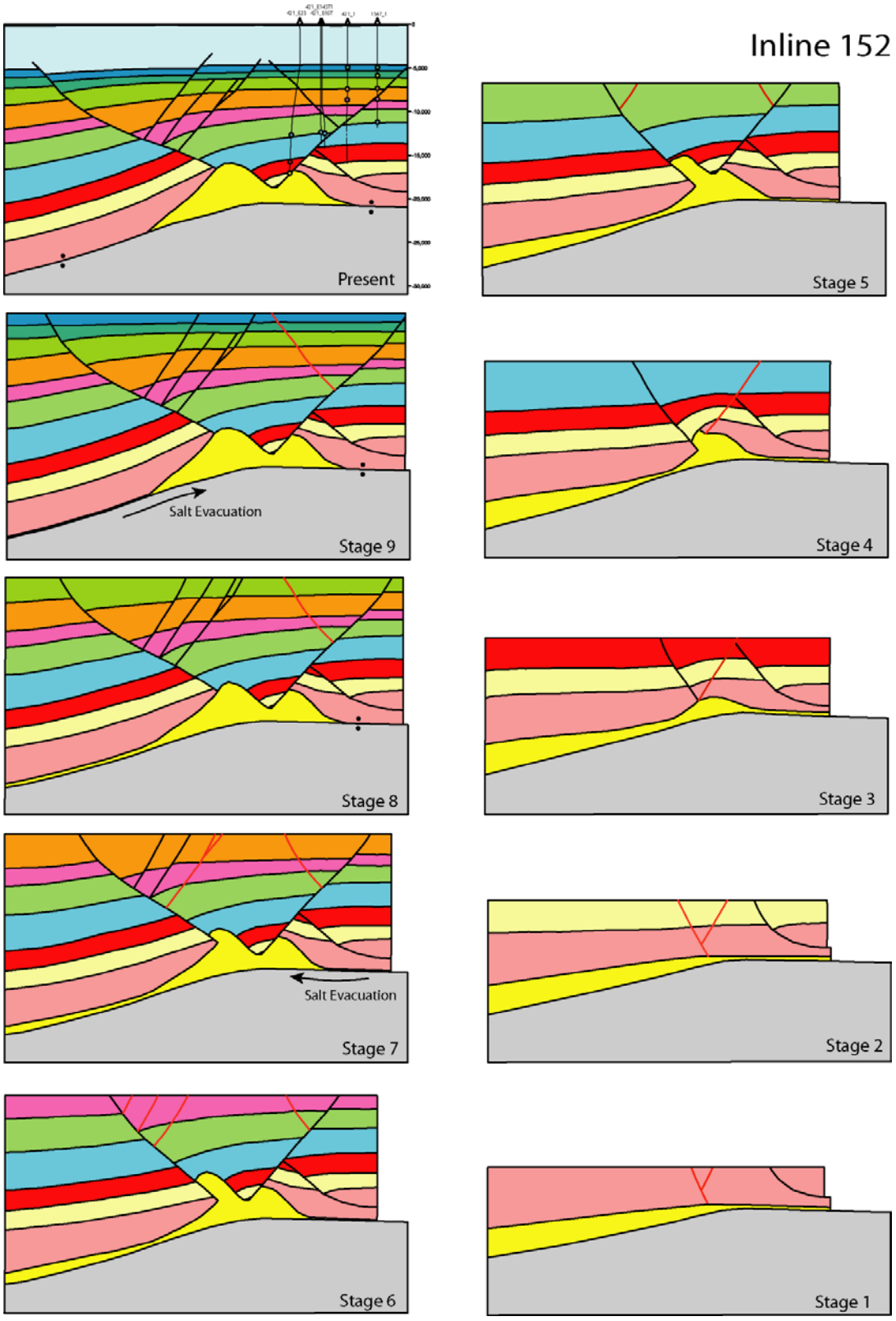

Figure 2.19: Kinematic restoration of Inline 152 by sequential removal of units and application of decompaction. Restored faults are marked in red and direction of salt evacuation is shown right before salt welds have formed.

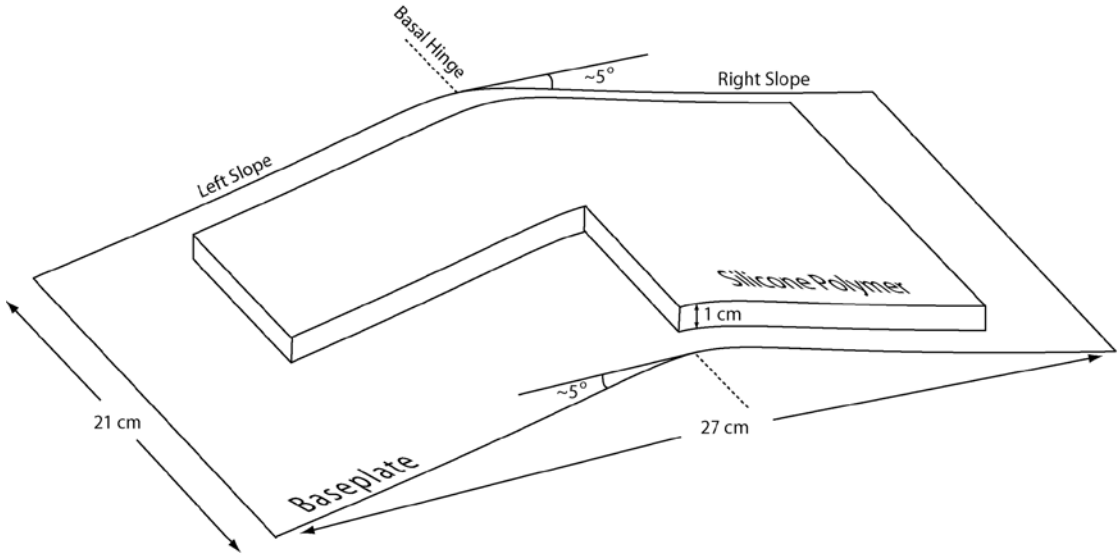

Figure 2.20: Experimental setup for the clay model with the bent base plate dipping by an angle of 5° on two sides. The clay is overlain on top of this setup with the silicone polymer underlying the clay cake and distributed in the shape shown in the figure.

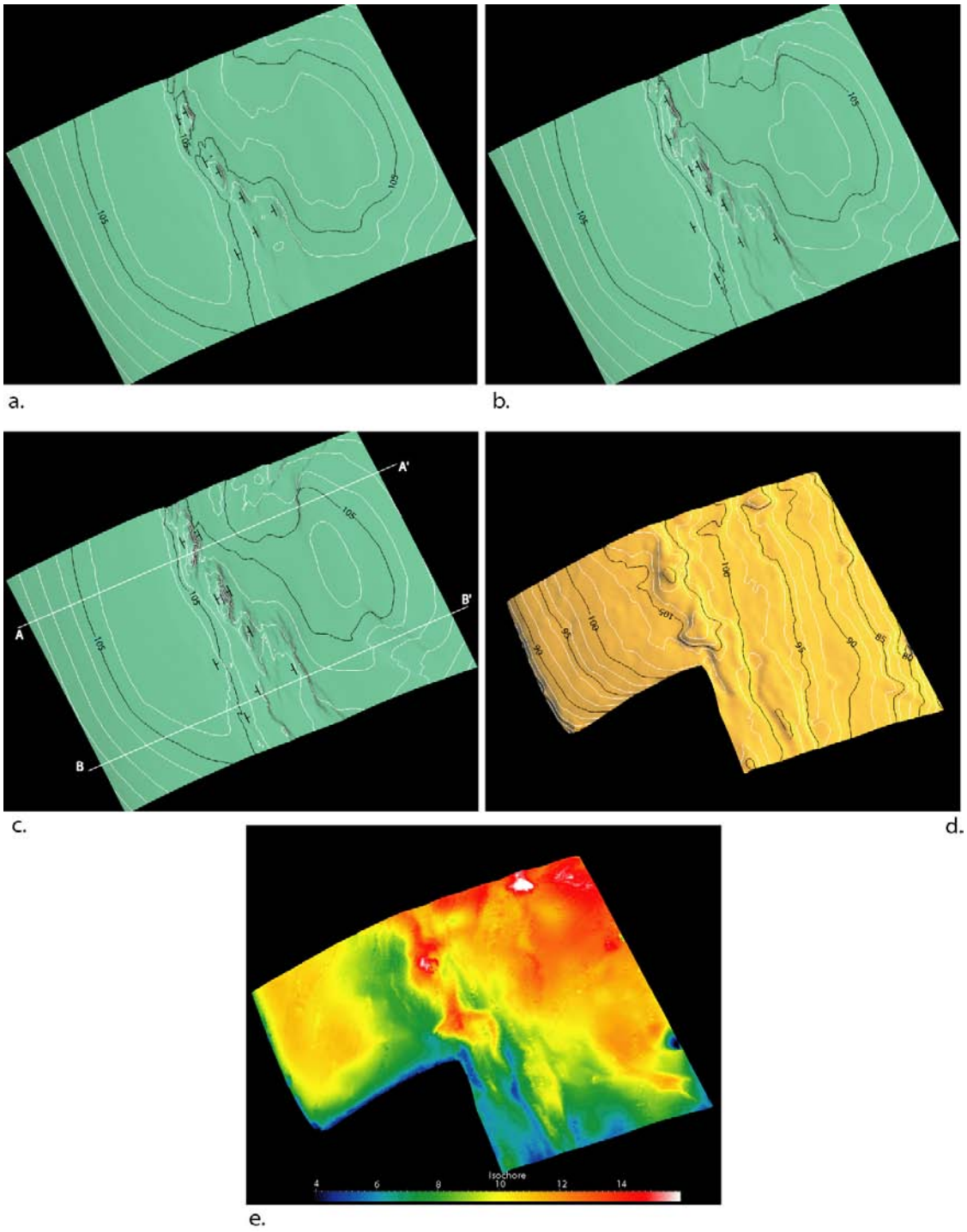

Figure 2.21: 3D model of the top of the clay surface at the (a) initial, (b) middle and (c) final stage. The fault dips are annotated on the clay surface and the orientation of the surface is the same as shown in the setup. Locations of schematic cross sections of next figure are shown in (c). (d) The contoured surface of the top of the silicone polymer indicating structural high above the basal hinge. (e) Isochore surface for the top of the silicone polymer indicating thicker silicone above the basal hinge.

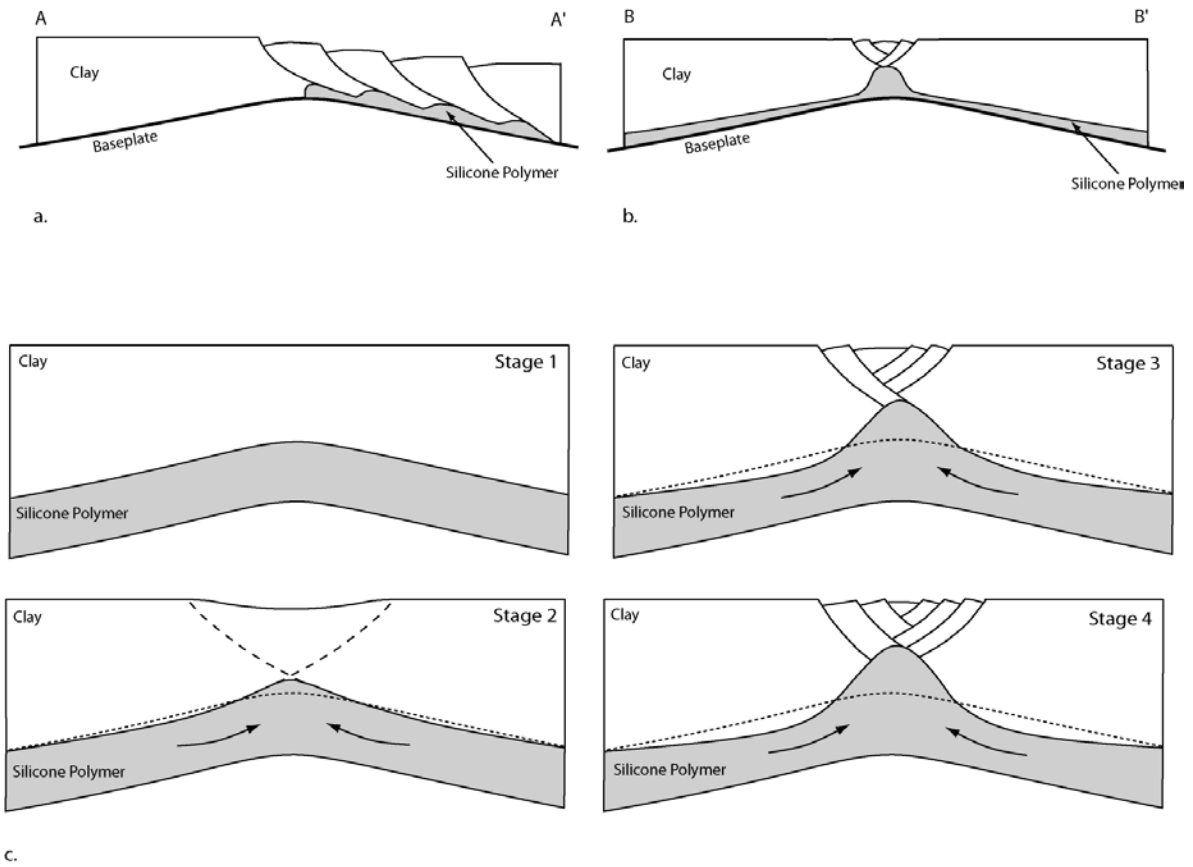

Figure 2.22: (a) Schematic cross section across the clay where silicone polymer is absent on the left slope. The polymer forms highs in the footwall of the faults. (b) Schematic cross section across the clay model where silicone polymer is present on both slopes. The polymer forms a high above the basal hinge. Locations of cross sections are shown in Figure 2.21 c. (c) Possible evolutionary process of the collapsed crestal structure. Dotted line indicates the original geometry of the top of the silicone polymer and as the structure evolves, the silicone from the two slopes migrate towards the basal hinge to form a structural high while lows form in areas immediately adjacent to the hinge.

CHAPTER 3

STYLES OF LISTRIC NORMAL FAULT SYSTEMS IN THE NORTHERN GULF OF MEXICO: INSIGHTS FROM 3D LASER SCANNED CLAY EXPERIMENTS

Abstract

Passive margin settings such as the Gulf of Mexico is abundant in listric normal faults that detach at different stratigraphic levels and lithological units, thereby giving rise to different styles of faulting. The salt cored structures offshore Louisiana are characterized by basinward and landward dipping short arcuate faults detaching above shallow or deep salt while fault systems involving only a homogenous lithological package in offshore Texas contain mostly basinward dipping long linear faults. Clay experimental models with sloping flat base plate setups have been used to gather insights on the controls of the two structural styles and how they interact with each other forming complex transfer zones. Silicone polymer has been used as an analog of salt in order to model fault patterns and ductile flow beneath wet clay layers. The surfaces of the clay cake have been scanned by 3D laser scanners to allow 3D visualizations and accurate measurements of features. The experiments were able to generate two fault styles, one detaching above the basal contacts of the plates, representing the homogeneous lithology fault style and the other detaching above the silicone polymer, representing the salt cored listric fault style. The results reveal that the dips of the series of synthetic faults above the silicone polymer are controlled by the basal slope with the faults initiating at the head of the silicone polymer layer, while the basal discontinuity controls the location and dip of the main fault when no silicone polymers were present. The direction of slope, the direction of down drop of basal discontinuities and the position of the basal discontinuity with respect to the head of the silicone polymer play important roles in determining orientation and styles of listric normal faulting. Complex transfer zones develop at the

boundary of the silicone polymer and fault patterns whose geometries also depend on the above mentioned factors.

3.1 Introduction

The northern Gulf of Mexico shelf region contains growth faults that are unique in style, varying with the tectono-stratigraphic settings. Structures within a relatively homogeneous package made up of interlayered sand and shale typically exhibit well-defined rollover folds related to listric faults resulting in the formation of asymmetric half-grabens (Groshong, 1989) or horst-graben blocks (Whitbread et al., 2000). The geometry of the rollover folds are closely related to the fault geometry and the mechanisms of deformation (Dula, 1991; Xiao and Suppe, 1992) and mostly related to secondary synthetic and antithetic faults in cross sections. Map patterns normally consist of long and straight major faults dipping mostly basinward. On the other hand, the presence of allochthonous salt at the base of the stratigraphic package results in a series of structures characterized by the flow of salt from the frontal to the distal parts of each block, and resultant footwall highs in each block. In map view, this style is characterized by short arcuate faults that detach at the allochthonous salt and have both regional and counterregional dips (Worrall and Snelson, 1989). Salt cored growth faults have been studied by integrating 2D and 3D seismic data (Worrall and Snelson, 1989; Rowan et al., 1994; Diegel et al., 1995, Schuster 1995; Peel et al., 1995; McBride et al., 1998; Rowan, 1995; Rowan et al., 1999; Rowan and Inman, 2006). The evolution of these structures has mostly been explained in relation to regional system of faults (the Roho System) and the counter regional faults (the Stepped Counter Regional Fault System).

These two distinct fault styles therefore have different fault shapes, secondary fault patterns and footwall deformations (Fig 3.1). Furthermore, the boundaries of the allochthonous salt sheets are likely to be marked by abrupt changes in the density, and

orientation of faults. This study addresses the primary controls of faults geometries for these two different styles, and the structures resulting from the interaction of the two styles, using scaled experimental models. First, it examines the controls of the direction of slope on the basal detachment and the direction of extension on each of the structural styles. Second, it examines the formation of transfer zones formed as a result of juxtaposition of the two styles along the boundaries of the allochthonous salt sheets.

The results of the study will be useful in understanding both the evolution of different types of growth fault structures in the Gulf of Mexico, as well as variations in fault patterns along transfer zones.

3.2 Previous Studies

Analog experimental models have been used to investigate evolution of structures associated with listric normal fault systems forming in homogeneous stratigraphic packages, using both sand (McClay and Ellis, 1987; Ellis and McClay, 1988) and clay (Cloos, 1968; Withjack et al, 1995; Serra and Nelson, 1988; Dula, 1991; Bose and Mitra, 2009, 2010). Cloos (1968) conducted one of the first experiments using wet clay on overlapping flat base plate setups to model listric faults in both sectional and map views. Flat base plate setups have been subsequently used in clay experiments to model fault patterns in listric normal fault systems (Serra and Nelson, 1988; Bose and Mitra, 2009, 2010). Stratigraphic packages with a ductile salt layer at the base have been successfully modeled using sand and silicone putty to model clastic package and salt respectively (Vendeville and Cobbold, 1988; Childs et al., 1993; Jackson et al., 1994). Although a combination of silicone polymer and wet clay has not been previously used to model

listric faults, it has been used to model salt related structures in rift systems (Withjack and Callaway, 2000; Ballahsen et al., 2003). Basal slope has rarely been applied to clay models to model listric faults, although Cloos (1968) obtained significant results by application of a slope and allowing clay to respond to gravitational forces.

Three dimensional visualization and modeling techniques enable more detailed analyses of structural evolution in experimental models that traditional methods using 2D photographs. Various methods have been applied to extract 3D data from analog models, viz. CAT scans of sandbox models (Schreurs et. al., 2001), digitizing and rendering serial cross sections (Guglielmo et. al., 1997) and photogrammetric techniques for extracting three dimensional geometry (Fischer and Keating, 2005). Other than the CAT scan technique, the rest do not provide a direct method of extracting data from the models nor do they have a high enough resolution to allow detailed analyses. A direct method of using high resolution scanning on clay models is the application of 3D laser scanners (Bose and Mitra, 2010) which not only gives a high precision of collecting data, but also allows accurate measurements to be performed on the surface of the clay.

The controls of directions of extension and basal slope on fault geometries have not been previously studied for homogenous or salt-cored systems, nor has the formation of transfer zones at the junctions of the two systems been previously investigated.

This study applies a slope to the flat base plate setup with silicone polymer underlying the wet clay in order to model the effect of slope and direction of extension on presence of a ductile basal unit such as the silicone polymer.

3.3 Experimental Procedure

For all the experiments in this work, two overlapping flat base plates are used, one of which is attached to a fixed backstop, and the other to a moveable backstop. Displacement is introduced by extending the moveable plate away from the fixed plate. The contact line between the plates represents stratigraphic or structural discontinuities of natural rocks, which may cause major faults to initiate above them. For each experiment, two separate stratigraphic packages, separated by a vertical boundary parallel to the length of the plates, are used. One package consists of 5 cms. of wet clay, representing a homogeneous sand/shale stratigraphy, whereas the other package consists of 1cm of silicon polymer layer overlain by 4 cm of wet clay representing a stratigraphy in which a sand/shale interlayer is underlain by salt. This configuration enables us to study the differences between the fault patterns within the two types of packages, and also the transfer zones formed along the boundary between the two packages.

Wet clay has been successfully used by various authors to model natural structures since it deforms in a similar manner as natural rocks under applied stress (Oertel, 1965; Cloos, 1968; Hildebrand-Mittlefehldt, 1979; Reches, 1988). It possesses a cohesive strength on the order of 10^{-4} to 10^{-5} of the upper crustal rocks and has a coefficient of internal friction of 0.6, making them ideal for scaled modeling materials (Hubbert, 1937; Withjack et al., 2007). Wet clay is chosen as the modeling material over dry sand in this particular study due its ability to form distributed discrete faults that enable various analyses with respect to length and orientation. The clay also allows 3D laser scanning of the top surface to analyze the topology of the structures formed (Bose and Mitra, 2010).

Pure Silicone Fluid (PSF) or Polydimethylsiloxane (PDMS) with a viscosity of 2,500,0000 centistokes has been used as an analog of wet evaporite due to similar physical properties (Weijermars 1986; Weijermars et al., 1996) and has been successfully used in experimental models involving gravity driven extension (Vendeville and Jackson, 1992 a&b; Fort et al., 2004). PDMS is a Newtonian fluid with no yield strength, a property that is shared with wet evaporites. The density ratio between wet clay (1.6 gm/cc) and PDSM (1 gm/cc) is 1.6, which is higher than that between natural sedimentary packages and salt (1.05 to 1.18), but since the deformation is driven by gravity and not by density ratio, this difference in ratio is acceptable (Weijermars, 1986).

The rate of displacement for the moveable backstop is maintained at a very slow rate of 0.01 cm/min. The silicone layer is enclosed on all sides by wet clay and the three surfaces of the clay cake are free surfaces where no shearing stresses occurred on them. The two sides are photographed while the top surface is scanned with a 3D laser scanner at equal increments of displacement. A basal slope of 5° is introduced in all the experiments. The up-slope boundary of the silicone is defined as the 'head' and the down-dip boundary as the 'toe'.

Five different setups (Figure 3.2) are used to study the effects of different parameters, as follows:

1. *Direction of the slope with respect to the direction of extension*: The slope is varied between setups A and B, other applied conditions remaining the same. Setup A has a slope in the direction of displacement of the moving plate, whereas B has the slope

dipping towards fixed plate. This set of experiments examines the controls of slope and direction of extension on the two types of stratigraphic setups.

2. *Overlap of the base plate with respect to the direction of extension*: The underlying plate is moving in setup A, whereas the overlying plate is moving in setup C. This set of experiments examines the control of the discontinuity that causes the propagation of the faults.

3. *Location of the silicone polymer head with respect to the plate boundary*: Setups A, D and E illustrate different positions of the head of the silicone layer with respect to the overlapping line of the plates. This set examines the control of the frontal boundary of the salt on the propagation of the faults for salt cored structures.

The top surface of the clay experiment is incrementally scanned by a 3D laser scanner, a technology that has been in use in numerous other industries. In addition the top of the silicone layer is scanned in the final stage.

Laser-scanning technology has been applied successfully to generate virtual surfaces for a much detailed and precise analyses (Bose and Mitra, 2010; Mitra and Paul, 2010). The laser scanner, placed above the top surface at a distance of 38 cm, is equipped with four sets of Class 1M, 10MW solid state line lasers and two 3.0 Megapixel CMOS sensors. The scanner collects data at a horizontal and vertical resolution of 75 DPI (about 0.03 cm point density) over a width of 34.3 cm by 25.6 cm. The four line lasers scan the surface and the CMOS sensor continuously captures the reflected beams from the clay surface. Figure 3.3 displays the working principle of the laser scanner, where the coordinates of points on the surface are calculated using a triangulation method, since the

angle of laser projection (α), the angle at which the sensor collects the data (β) and the distance between the sensor and laser source are known (Petrov et al., 1998). The angle β is calculated from the focal length and pixel size of the sensor. The four sets of line lasers provide further accuracy by measuring the coordinates of a point at least twice. The first point that the sensor calculates is taken as the reference or origin of the coordinate system in which the rest of the points are placed. Therefore, the scanner has to be retained in its original position throughout the experiments in order to place each scanned surface in the same coordinate system. The scanned data is exported as a point cloud into GoCAD that allows 3D virtual surfaces to be built from the point sets.

In addition to the laser scanning, the top photographs were used to trace the faults in ArcView GIS (Environmental System Research Institute, Redlands, CA) in order to obtain the fault orientations.

3.4. Experimental Results

3.4.1. Structural Geometries

In all experiments, two distinct fault styles develop in the experiments simultaneously, depending on the interlayer composition, one consisting of a clay layer and the other consisting of clay underlain by silicone layer.

1. Clay Layer Only (Representing Homogeneous Sand/Shale Interlayer): The major fault initiates at the discontinuity defined by the contact of the two metal plates, and the structure initially develops as a symmetrical graben centered above the contact of the underlying and overlying base plates. The graben is bound on either side by a primary

synthetic fault attached to the overlying plate and a primary antithetic fault tied to the moveable plate. As displacement progresses, the single primary synthetic fault accommodates most of the slip, while a series of secondary antithetic faults form that finally leads to an asymmetrical half-graben structure (Cloos, 1968; Bose and Mitra, 2009, 2010). Although a number of antithetic faults are present as opposed to a single master synthetic fault, the primary antithetic fault that develops at the very initiation of displacement accommodates more slip than the other secondary antithetic faults.

2. Clay Layer Underlain by Siicone Polymer (Representing Sand/Shale InterlayerUnderlain by Salt): The geometry of the faults controlled by the basal silicone layer differs significantly from those mentioned in the previous section. The shapes of the faults are more listric and they steepen towards the top free surface (Vendeville and Cobbold, 1987). A series of synthetic faults develop dipping towards the basal slope with no major antithetic faults forming within the system. Although the base plate is being extended, the faults are not localized above the plate contacts but initiate at the head of the silicone layer, often occurring as a spaced sequence of faults. Extending the plate only creates space and allows the silicone layer to flow down the slope and thereby develop faults above it.

Also, in contrast to the faults controlled by the base plate contact, no half-graben structure develops and the two fault styles interact to form complex transfer zones. The silicon layer typically flows towards the front to the back end of each fault block, thereby forming silicone ridges parallel to the trend of the faults.

The results of the individual experiments are discussed using the 3D surfaces and fault trace maps. The structural evolution is explained by grouping the experiments into three sets, following the classification in the Experimental Approach section. The individual sets are described and compared with each other in order to provide insights on the controlling factors for the fault patterns and localizations.

Experimental Set 1: Direction of Displacement Vs. Slope:

This experimental set compares experiment A, in which the direction of displacement is the same as the slope, to experiment B, where the direction of displacement is opposite to the slope. (Figure 3.4 and Fig 3.5). For both experiments in this set, the faults within the clay directly above the plates develop faults earlier than those above the silicone layer. The two styles of faulting mentioned above, form independently. The package consisting of homogeneous clay develops a major fault (package I), and a related major antithetic fault, along with a series of smaller synthetic and antithetic faults. The package with the clay underlain by the silicon layer (package II) develops a series of major faults all dipping in the same direction. The silicone layer underneath the clay cake deforms accordingly, forming structural highs in the footwall of the faults (Fig 3.4c and Fig 3.5c).

In experiment A, the major faults in both packages dip in the same direction as the slope and the direction of extension. However, in experiment B, the major fault in package I dips in the direction of extension, whereas the faults in package II dip in the same direction of slope. Therefore, in package II, the direction of extension does not

control the dip direction of the faults. The series of faults always dips towards the direction of the slope with very few minor faults dipping up slope.

In both experiments, a complex transfer zone forms at the boundary of the silicone layer (Fig 3.4a & b and 3.5a & b) with a large offset between two major faults dipping. The two fault systems curve towards each other and changed orientation by 30°. The trends of the oblique faults are not same for both experiments and are controlled by the direction of slope and the dip direction of faults above the silicone layer. For example, in setup A (Fig 3.4b) the faults were oriented at 110° - 120° with the direction of extension while that in Setup B (Fig 3.5b) were oriented at an angle of 30°.

Experimental Set 2: Direction of Plate Overlap or Discontinuity:

This set of experiments compares experiment A in which the underlying plate is moving, so that the drop in the detachment is in the direction of extension, with experiment C, in which the overlying plate is moving, so that the drop in the detachment is opposite to the direction of extension (Fig 3.4 and Fig 3.6). This set thereby compares whether the direction of the discontinuity plays a more major role than the direction of extension. The dip direction of the main fault in package I is opposite to the direction of extension, and in the same direction as the drop down in the detachment to the direction of extension. Faulting in package II is similar to that in experiment A, since the silicon polymer damps out the effects of the discontinuity, and the dip direction of the faults is the same as the direction of the slope. The geometry of the silicone layer after deformation (Fig 3.6c) and the change in orientation of faults within the transfer zone (Fig 3.6b) are similar to that in experiment A.

This experimental set shows that in a homogeneous sand/shale stratigraphy, the most important factor in determining the dip direction of the major fault is the direction of drop down of a pre-existing discontinuity.

Experimental Set 3: Position of Head of Silicon Polymer

This set of experiments compares the fault patterns in experiments A, D, and E, in which the position of the head of the silicon layer varies relative to the position of the boundary between the plates (Figure 3.4, Fig 3.7 and Fig 3.8). The head of the silicon layer is in front of the plate boundary in A, almost in the same position in D, and slightly behind it in E. The directions of extension, slope, and the down drop in the detachment are same in all three experiments, so that the fault patterns in package I are very similar. Compared to experiment A, the faults geometries in experiment D form in a similar manner, with the asymmetric half-graben developing in the clay directly above plates and a few synthetic faults forming above the silicone layer (Fig 3.4a and Fig 3.7a). The major antithetic fault in the clay directly above the plate interacts with the synthetic fault formed above the silicone layer although there is little or no change in orientation of the faults along the boundary of the silicone layer since the head of the silicone layer almost coincided with the contact between the base plates (Fig 3.7b). The linear trend of the silicone layer (Fig 3.7c) underlying the clay cake also exemplifies the lack of change in orientation of the structure at the transfer zone.

In experiment E, two systems of faults evolve on either side of the clay cake, offset along the boundary of the silicone layer (Fig 3.8a). The fault geometries are similar to the previous experimental sets, although they undergo a minor change in orientation

within the transfer zone (Fig 3.8b). Instead of developing a series of synthetic faults, a single master fault forms above the silicone layer close to the head of the silicone layer. The silicone accumulation beneath the wet clay shows similar geometry as that of the experiment D (Fig 3.8c). The structural offset causes the master synthetic fault above the silicone layer and the major antithetic fault directly above the plates to form a divergent transfer zone with the two main faults dipping away from each other. The results of these experiments show the variations in the geometry of the transfer zone that can result depending on the position of the silicon layer.

3.4.3 Structural Relief and Fault Evolution

The fault evolution and structural relief are illustrated in this section with the help of the virtual 3D surfaces generated from the laser scanned data. The three dimensional analyses allows certain operations such as accurate area and fault displacement measurements that were not possible in traditional methods of photography. The structural relief and fault evolution analyses are shown for the experiment with setup B since the processes are similar for the rest of the experiments.

The two styles of faulting that develop in the clay cake are caused by the same amount of displacement along the moveable backstop. In order to demonstrate the amount of deformation on both sides of the clay cake, the relief changes are calculated on either side. Figure 3.9a displays the two sections 1 and 2, along the package II and I respectively, along which the relief is calculated. These sections are oriented parallel to the direction of extension and perpendicular to the strike of the faults. Extension causes a subsiding clay surface bounded by normal faults and the change in relief increased during

progressive displacement on either side of the clay cake. The areas on the two sections, bounded by the traces of the undeformed and deformed clay surfaces, are calculated to be constant on both sections at each incremental stage of displacement (Fig 3.9 b & c). For example, in the initial stages, section 1 has a relief area of 173 sq. mm while section 2 has an area of 179 sq. mm. In the final stage of the experiment, section 1 attains a relief area of 638 sq. mm and section 2 has an area of 623 sq. mm. This proves that although the fault geometries and styles were different for the two fault systems, the amounts of deformation accommodated by them were the same.

The fault evolution analysis allows the visualization of the incremental growth of faults, also displaying their relative timing and three dimensional connectivity. A tilt correction is applied to the surfaces to remove the 5° inclination and the major fault scarps are color coded with respect to throw. Figure 3.10 a-c displays only the fault surfaces in the map view through three stages of displacement. The growth patterns of the fault scarps are illustrated by focusing on a few selected faults. In Fig 3.10a-b faults A1-A2 and B1-B2 occur as isolated fault segments with low throw values and as displacement progresses, they increase in length and throw, ultimately connecting to form larger faults A and B respectively. Fault segments D1-D2 form at a later stage of extension and although they grow and coalesce to form a single fault D, their throw do not increase as much as the previous faults. Fault C, on the other hand, forms at an angle to the direction of extension/slope and therefore does not accommodate a large amount of deformation. It remains relatively constant length and throw, not connecting with other segments to increase its size. One fault (Fault A) has been chosen to demonstrate in detail its growth and three dimensional connectivity as it laterally links while accommodating

larger displacements (Fig 3.10 d-f). The figure shows the fault scarps by facing in a perpendicular direction at the fault surface.

3.5 Discussion and Comparison to Natural Examples

The natural subsurface structures in this section have been categorized according to the two styles of listric normal faults in the Gulf of Mexico viz. the salt cored and the homogenous sedimentary package listric normal fault systems. Transfer zones exist within each type, as well as between the two fault styles. Each is presented with their uniqueness and the common features that are observed in all structures along with their similarities to structures obtained in the experiments.

1. The Salt Cored Style of Faulting: The Louisiana growth fault system detaches above the allochthonous salt forming the Roho system or the Counterregional system. The controlling factor favoring the Roho system has been put forward as extension driven by sedimentation and basal slope and that for the Counterregional system as subsidence (Schuster, 1995; Jackson and Schultz-Ela, 2000), although natural systems are a combination of the two (Hudec and Jackson, 2006). In all the previous studies, slope has never played an important role in formation of the Counterregional system. It has been established, though, from the experiments in this study that a slope opposite to extension can, in fact, still be able to form faults dipping opposite to extension and the natural examples will be exemplify this fact as well.

The localization of faulting above the salt has also been a matter of debate and due to the absence of any basal discontinuities, the factor responsible for detaching a fault

at a particular location has also been vaguely understood. The experimental results reveal that faulting always initiates at the head of the silicone layer and dip down slope, no matter where the center of extension may lie. A series of synthetic faults ensue along the slope after initial faulting with silicone layer accumulating in the hanging wall of the major faults.

The natural examples from the Gulf of Mexico exemplify the above mentioned factors and therefore lead to a better understanding of the controls determining the fault geometries and their localizations. Figure 3.11 shows a north-south trending section through the Plio-Pliestocene zone in offshore western Louisiana that display salt cored geometries of the listric regional faults with a prominent basinward slope. As observed in the experiments, the faulting causes the salt to evacuate from the hanging wall to the footwall of the major faults, resulting in the formation of salt ridges. This causes salt thickening of and formation of structural highs in the footwall. The series of down to the basin major faults also have fewer antithetic faults associated with them.

The counterregional fault system had previously been described to be formed not by extension, but by out of the plane salt evacuations leading to pseudo-extension. The following examples, though, show a landward slope which would make it difficult to explain the formation of the counterregional fault only by sedimentation and salt evacuation. Figure 3.12 displays a seismic section along a counterregional fault (CR) with the entire salt supposed to be evacuated. In this example a landward basal slope can be observed along which the fault has detached indicating to the fact that the slope could play a role in controlling the direction of faulting and salt evacuation.

2. Homogeneous Sedimentary Package Faulting: Listric faults in homogeneous sedimentary packages are typical features in offshore Texas that form primarily due to pre-existing stratigraphic or structural discontinuities. The Vicksburg Detachment System and the Brazos Ridge in south Texas are two areas where a shale detachment system can be imaged in seismic. These systems of faults typically form major down to the basin listric faults with secondary faults forming in the hanging walls (Fig 3.13a) affecting the Oligocene and Miocene sediments along the Texas coast. Both the systems show master basinward dipping faults (R1 and R2) with the antithetic faults outnumbering the synthetic faults (Fig 3.14b and Fig 3.14) Besides the presence of salt, faults within homogeneous sedimentary package (the Texas style) are geometrically distinct from the salt cored fault systems of Louisiana. Here, the master faults are less listric than those observed in salt related systems and at deeper levels and as a result, the faults continue in the same angle of dip for more than 20 km. Both Vicksburg system and Brazos Ridge display one or two major antithetic faults (CR1 in case of Vicksburg and CR1 through CR4 in Brazos) that take up more extension than the numerous other smaller faults. The total extension in the Vicksburg system has been calculated to be about 7% of that in the salt related systems of the Louisiana (Diegel et al., 1995) indicating the influence of a ductile unit in accommodating extension.

3.6 Conclusions

The present study reveals insights on the conditions and factors controlling the development of the two different listric normal fault styles in the Gulf of Mexico and other passive margins. The effects of ductile detachment, basal discontinuity, basal slope

and direction of extension on the geometry of listric normal faults are illustrated using analog clay models. The experimental results, confirmed with natural examples, illustrate that the slope of the basal detachment plays the most important role in determining the dip directions of faults above a ductile unit. The directions of extension as well as the localized centers of extension impart little or no influence on the fault patterns above the silicone layer. On the other hand, the geometry of the basal discontinuity and the direction of extension are responsible for fault patterns and geometries where no ductile basal layer is present. In addition, the faults are more listric and possess fewer antithetic faults in the presence of a silicone layer.

The two systems of faults form complex transfer zones along the boundary of the silicone layer where the orientation of the major faults changed by as much as 30°. The orientations and overall geometry of faults within the transfer zone are controlled by the direction of slope and the relative position of the silicone layer with respect to the location of the basal contact of the plates. This suggests that in basins marked by discontinuous salt bodies, the boundaries of the salt layer may represent areas for the formation of important transfer zones.

When compared to natural subsurface structures and their final fault geometries, the experimental results are important in deciphering the evolutionary history and conditions controlling their final geometries. As opposed to previous theories regarding regional and counterregional faults in offshore Louisiana, the experiments suggest that the occurrence of regional (roho) and counterregional fault systems may be controlled by the initial slopes of the allochthonous salt bodies. The more common Roho systems marked by basin ward dipping faults may form where the salt bodies slope basinward,

whereas the less common counterregional systems may develop in directions opposite to the overall extension where local slope reversals in the allochthonous salt bodies are present. On the other hand, fault patterns in more homogeneous and/shale packages without underlying salt are more controlled by the orientation of pre-existing discontinuities, and the direction of regional extension

Other kinematic observations, confirmed from experiments and restorations performed by other authors, included the initial development of faults in the upslope boundaries (head of the silicone layer or heel of the salt bodies) with progressive faulting down slope, greater listricity of master faults and fewer of antithetic faults when ductile detachments are present and formation of transfer zones at the lateral boundary of the ductile detachments. These results are important in understanding the controls and factors affecting faults style in the Gulf of Mexico.

References

Ballahsen, N., J-M Daniel, L. Bollinger and E. Burov, 2003, Influence of viscous layers in the growth of normal faults: insights from experimental and numerical models: Journal of Structural Geology, v. 25, p. 1471-1485.

Bose, S. and S. Mitra, 2010, Analog modeling of divergent and convergent transfer zones in listric normal fault systems: American Association of Petroleum Geologists Bulletin (in press).

Bose, S., and S. Mitra, 2009, Deformation along oblique and lateral ramps in listric normal faults: Insights from experimental models: American Association of Petroleum Geologists Bulletin, v. 93, p. 431-451.

Childs, C., J. Watterson, and J. J. Walsh, 1995, Fault overlap zones within developing normal fault systems: Journal of the Geological Society of London, v. 152, p. 535-549.

Christensen, A. F., 1983, An example of a major syndepositional listric fault, in A. W. Bally ed., Seismic expressions of structural styles; a picture and work atlas: American Association of Petroleum Geologists Studies in Geology, v. 15, p. 2.3.1-36-2.3.1-40.

Cloos, E., 1968, Experimental analysis of Gulf Coast fracture patterns: American Association of Petroleum Geologists Bulletin, v. 52, p. 420-444.

Diegel, F. A., J. F. Karlo, D. C.Schuster, R. C. Shoup, and P. R. Tauvers, 1995, Cenozoic structural evolution and tectono-stratigraphic framework of the northern Gulf Coast continental margin, in M. P. A. Jackson, D. G. Roberts, and S. Snelson,

eds., Salt tectonics: A global perspective: American Association of Petroleum Geologists Memoir, v. 65, p. 109–151.

Dula Jr., W. F., 1991, Geometric models of listric normal faults and rollover folds: AAPG Bulletin, v. 75, p. 1609–1625.

Ellis, P. G and K. R. McClay, 1988, Listric extensional fault systems; results of analogue model experiments: Basin Research, v.1, p. 55-70.

Erxleben, A. W and G. Carnaham, 1983, Slick Ranch area, Starr County, Texas, in A. W. Bally ed., Seismic expressions of structural styles; a picture and work atlas: American Association of Petroleum Geologists Studies in Geology, v. 15, p. 2.3.1-22-2.3.1-26.

Fischer, M. P. and D. P. Keating, 2005, Photogrammetric techniques for analyzing extension, strain, and structural geometry in physical models: Application to the growth of monoclonal basement uplifts: Geological Society of America Bulletin, v. 117, p. 369-382.

Fort, X, J-P Brun, F. Chauvel, 2004, Salt tectonics on the Angolan margin, synsedimentary deformation processes: American Association of Petroleum Geologists Bulletin, v. 88, p. 1523-1544.

Groshong Jr., R. H., 1989, Half-graben structures: Balanced models of extensional fault-bend folds: Geological Society of America Bulletin, v. 101, p. 96–105.

Guglielmo, G., M. P. A. Jackson and B. C. Vendeville, 1997, Three-dimensional visualization of salt walls and associated fault systems: American Association of Petroleum Geologists Bulletin, v. 81, p. 46-61.

Hildebrand-Mittlefehldt, N., 1979, Deformation near a fault termination, part I: A fault in a clay experiment: Tectonophysics, v. 57, p. 131-150.

Hubbert, M. K., 1937, Theory of scale models as applied to the study of geologic structures: Geological Society of America Bulletin, v. 48, p. 1459-1520.

Hudec, M. R. and M.P.A Jackson, 2006, Advance of allochthonous salt sheets in passive margins and orogens: American Association of Petroleum Geologists Bulletin, v. 90, p. 1535-1564.

Jackson, M. P. A. and D. D. Schultz-Ela, 2000, Why roho, why counterregional?: Annual Meeting Expanded Abstracts – American Association of Petroleum Geologists, v. 2000, p. 23.

McClay, K. R. and P.G. Ellis, 1987, Geometries of extensional fault systems developed in model experiments: Geology, v. 15, p. 341-344.

Mitra, S. and D. Paul, 2010, Structural geometry and evolution of releasing and restraining bends: insights from laser-scanned experimental models: American Association of Petroleum Geologists Bulletin (accepted).

Oertel, G., 1965, The mechanism of faulting in clay experiments: Tectonophysics, v. 2, p. 343-393.

Peel, F. J, C. J. Travis and J. R. Hossack, 1995, Genetic structural provinces and salt tectonics of the Cenozoic offshore U.S. Gulf of Mexico: a preliminary analysis, in M. P. A. Jackson, D. G. Roberts, and S. Snelson, eds., Salt tectonics: A global perspective: American Association of Petroleum Geologists Memoir, v. 65, p. 153–175.

Petrov, M., A. Talapov, T. Robertson, A. Lebedev, A. Zhilyaev and L. Polonskiy, 1998, Optical 3D digitizers: Bringing life to the virtual world: IEEE Computer Graphics and Applications, v. 18, p. 28-37.

McBride, B. C., M. G. Rowan and P. Weimer, 1998, The evolution of allochthonous salt systems, northern Green Canyon and Ewing Bank (offshore Louisiana), northern Gulf of Mexico: American Association of Petroleum Geologists Bulletin, v. 82, p. 1013-1036.

Rowan, M. G., 1995, Structural styles and evolution of allochthonous salt, central Louisiana outer shelf and upper slope, in M. P. A. Jackson, D. G. Roberts, and S. Snelson, eds., Salt tectonics: A global perspective: American Association of Petroleum Geologists Memoir, v. 65, p. 199-228.

Reches, Z., 1988, Evolution of fault patterns in clay experiments: Tectonophysics, v. 145, p. 141-156.

Rowan, M. G. and K. F. Inman, 2006, Counterregional-style deformation in the deep shelf of the northern Gulf of Mexico: Gulf Coast Association of Geological Societies Transactions, v. 55, p. 716-724.

Rowan, M. G., M. P. A. Jackson and B. D. Trudgill, 1999, Salt-related fault families and fault welds in the northern Gulf of Mexico: American Association of Petroleum Geologists Bulletin, v. 83, p. 1454-1484.

Rowan, M. G, P. Weimer and P. B. Flemings, 1994, Three dimensional geometry and evolution of a composite, multilevel salt system, Western Eugene Island, Offshore Louisiana: Gulf Coast Association of Geological Societies Transactions, v. 44, p. 641-648.

Schreurs, G., R. Haenni and P. Vock, 2001, Four-dimensional analysis of analog models; experiments on transfer zones in fold and thrust belts, in H. A. Koyi and N. S. Mancktelow eds., Tectonic modeling: a volume in honor of Hans Ramberg: Geological Society of America Memoir, v. 193, p. 179-190.

Schuster, D. C., 1995, Deformation of allochthonous salt and evolution of related salt–structural systems, eastern Louisiana Gulf Coast, in M. P. A. Jackson, D. G. Roberts, and S. Snelson, eds., Salt tectonics: a global perspective: American Association of Petroleum Geologists Memoir, v. 65, p. 177-198.

Serra, S., and R. A. Nelson, 1988, Clay modeling of rift asymmetry and associated structures: Tectonophysics, v. 153, p. 307–312.

Vendeveille, B., 1987, Champs de failles et tectonique en extension: Modelisation experimentale,Memoires et Documents du Centre d'eude structurale des socles, No. 15, Rennes Cedex, France, 395 p.

Vendeville, B. and P. R. Cobbold, 1988, How normal faulting and sedimentation interact to produce listric fault profiles and stratigraphic wedges: Journal of Structural Geology, v. 10, p. 649-659.

Withjack, M. O., Q. T. Islam and P. R. LaPointe, 1995, Normal faults and their hanging wall deformation; an experimental study: American Association of Petroleum Geologists Bulletin, v. 79, p. 1-18.

Withjack, M. O., R. W. Schlische and A. A. Henza, 2007, Scaled experimental models of extension: Dry sand vs. wet clay: Houston Geological Society Bulletin, v. 49, p. 31-49.

Withjack, M. O. and S. Callaway, 2000, Active normal faulting beneath a salt layer: an experimental study of deformation patterns in the cover sequence: American Association of Petroleum Geologists Bulletin, v. 84, p. 627-651.

Whitbread, T., T. Nicholson and B. Owens, 2000, The Vicksburg of south Texas: A shelf-delta system with an attitude: Gulf Coast Association of Geological Societies Transactions, v. 1, p. 293-308.

Worrall, D. M., and M. Snelson, 1989, Evolution of the 764 northern Gulf of Mexico, with emphasis on Cenozoic 765 growth faulting and the role of salt, in A. W. Bally and 766 A. R. Palmer, eds., The geology of North America: An overview: Geological Society of America Decade of 768 North American Geology, v. A, p. 97–138.

Xiao, H., and J. Suppe, 1992, Origin of rollover: American Association of Petroleum Geologists Bulletin, v. 76, p. 509–529.

Figure Captions

Figure 3.1: Two distinct fault styles in the presence and absence of a salt substrate. (a) Schematic diagram of listric faults above salt (b) Experimental sandbox model of faulting above silicone polymer with a series of listric normal faults dipping towards extension (modified from Vendeville, 1987). (c) Subsurface example of listric faults above ductile salt in the Rhone delta (modified from Vendeville, 1987). (d) Schematic diagram of fault geometries in homogeneous sedimentary package. (e) Experimental clay model demonstrating synthetic (green) and antithetic (red) fault geometries formed in the hanging wall of listric faults devoid of ductile detachment. (f) Natural example of faulting in homogeneous sedimentary sequence showing similar synthetic (green) and antithetic (red) fault geometries (modified from Xiao and Suppe, 1992).

Figure 3.2 Experimental configurations with varying upslope boundary of silicone (Head) with respect to base plate contact and slope with respect to direction of extension (indicated by arrows). Base plate overlap is indicated by curved arrows. (a) Straight edge overlapping plates with slope in the direction of extension. Head of silicone polymer placed far from moveable backstop than base plate contact. (b) Straight edge overlapping plates with slope opposite to direction of extension. Head of silicone polymer placed further from the moveable backstop than the base plate contact. (c) Straight edge overlapping plates with slope in direction of extension. Head of silicone polymer placed further from moveable backstop than base plate contact. (d) Straight edge overlapping plates with slope in direction of extension. Head of silicone placed at same distance from moveable backstop as that of base plate contact. (e) Indented edge overlapping plates

with slope in direction of extension. Head of silicone polymer placed closer to moveable backstop than the base plate contact.

Figure 3.3: (a) Schematic diagram of the working principle of the laser scanner with the triangulation formed by the laser source, the detector and the point on the clay surface where the laser is reflected from. In three dimensions, the point on the surface would be a line. (b) Schematic view of the laser scanner projecting a line laser and sweeping across the clay surface at a constant velocity. (c) Real surface of the clay that has been scanned with the laser scanner. (d) Final virtual surface of the clay recreated from the point cloud.

Figure 3.4: (a) 3D structural geometry in the final stages of the Setup A. (b) Fault patterns developed in the final stages of the experiments in Setup A. The changes in orientation of the faults (20°-30°) are depicted in the Rose diagrams showing consistent bending along the boundary of the silicone polymer. (c) 3D geometry of the base plate and basal silicone polymer at the final stages of the experiments showing structural highs and accumulations in the head of the silicone polymer in Setup A.

Figure 3.5: (a) 3D structural geometry in the final stages of the Setup B. (b) Fault patterns developed in the final stages of the experiments in Setup B. The changes in orientation of the faults (20°-30°) are depicted in the Rose diagrams showing consistent bending along the boundary of the silicone polymer. (c) 3D geometry of the base plate and basal silicone polymer at the final stages of the experiments showing structural highs and accumulations in the head of the silicone polymer in Setup B.

Figure 3.6: (a) 3D structural geometry in the final stages of the Setup C. (b) Fault patterns developed in the final stages of the experiments in Setup C. The changes in orientation of the faults (20°-30°) are depicted in the Rose diagrams showing consistent bending along

the boundary of the silicone polymer. (c) 3D geometry of the base plate and basal silicone polymer at the final stages of the experiments showing structural highs and accumulations in the head of the silicone polymer in Setup C.

Figure 3.7: (a) 3D structural geometry in the final stages of the Setup D. The dip directions of the faults are marked along with the directions of extension and slope. The transfer zones form at the boundary of the silicone polymer. (b) Fault patterns developed in the final stages of the experiments in Setup D. No change of orientation of faults in setup D within the transfer zones are depicted in the Rose diagrams. (c) 3D geometry of the base plate and basal silicone polymer at the final stages of the experiments showing structural highs and accumulations in the head of the silicone polymer in Setup D.

Figure 3.8: (a) 3D structural geometry in the final stages of the Setup E. The dip directions of the faults are marked along with the directions of extension and slope. The transfer zones form at the boundary of the silicone polymer. (b) Fault patterns developed in the final stages of the experiments in Setup E. Little change (5°-10°) of orientation of faults within the transfer zones are depicted in the Rose diagrams. (c) 3D geometry of the base plate and basal silicone polymer at the final stages of the experiments showing structural highs and accumulations in the head of the silicone polymer in Setup E.

Figure 3.9: (a) Locations of two cross sections across the surface of clay in the final stage of experimental Setup B. (b) Areas within the cross sections 1 and 2, bounded by the undeformed stage and the initial deformed stage, reveal similar values of 173 and 179 square mm respectively. (b) Areas within cross sections 1 and 2, bounded by the undeformed stage and final deformed stage, show similar values of 638 and 623 square mm.

Figure 3.10: (a-c) Incremental stages of fault scarp growth (view from top) in experimental Setup B displaying lateral growth and connectivity between faults. The fault scarps are color coded with respect to the amounts of individual throw. Faults A, B and D form by the growth and coalescence of A1-A2, B1-B2 and D1-D2 respectively. Fault C being at an angle to extension, has limited growth. (d-f) View perpendicular to Fault A showing fault nucleation, lateral connectivity and extension accommodation.

Figure 3.11: (a) Locations of regional seismic lines in the shallow water Gulf of Mexico, offshore Louisiana. (b) Typical Roho style of faulting with a series of basinward dipping listric growth faults detaching at the shallow allochthonous salt sheet. (Modified from Diegel et al., 1995)

Figure 3.12: Seismic sections across the Bourbon Dome, offshore Louisiana showing Counterregional fault system (CR) forming at the upslope boundary of the salt body. The salt has been completely evacuated and the section shows a basal slope along the detachment. Location of section in Figure 4.12. (Modified from Schuster, 1995)

Figure 3.13: (a) Line drawing of seismic section showing typical fault geometries in a homogeneous sedimentary package in Slick Ranch field, Texas. (b) Seismic section across the Slick Ranch field, Texas showing large basinward dipping listric normal fault (blue), known as the Vicksburg Glide Place (R1) and secondary synthetic (green) and antithetic (red) faults formed in the hanging wall. Master fault is less listric and contains more secondary faults as also observed in the experiments.

Figure 3.14: Seismic section across the Brazos Ridge, Texas showing major basinward dipping fault, R1 (blue) and numerous secondary antithetic faults (red) and fewer synthetic (green) faults.

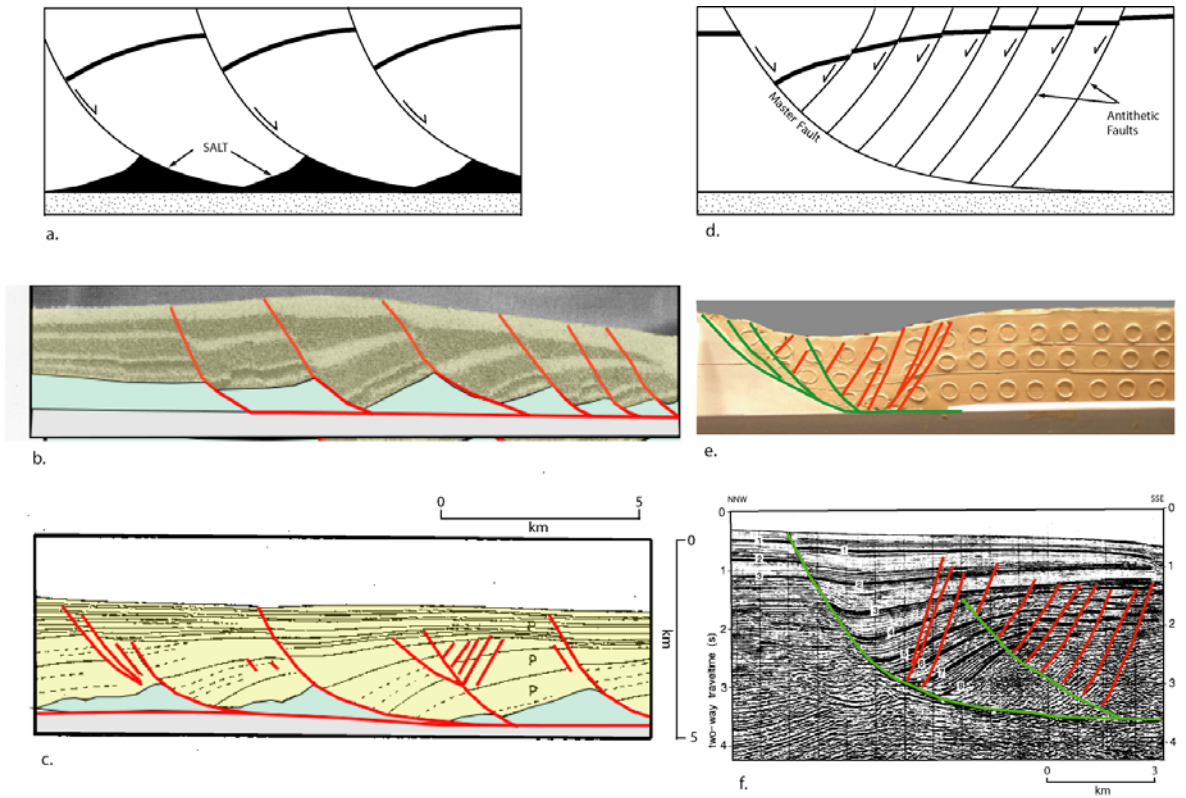

Figure 3.1: Two distinct fault styles in the presence and absence of a salt substrate. (a) Schematic diagram of listric faults above salt (b) Experimental sandbox model of faulting above silicone polymer with a series of listric normal faults dipping towards extension (modified from Vendeville, 1987). (c) Subsurface example of listric faults above ductile salt in the Rhone delta (modified from Vendeville, 1987). (d) Schematic diagram of fault geometries in homogeneous sedimentary package. (e) Experimental clay model demonstrating synthetic (green) and antithetic (red) fault geometries formed in the hanging wall of listric faults devoid of ductile detachment. (f) Natural example of faulting in homogeneous sedimentary sequence showing similar synthetic (green) and antithetic (red) fault geometries (modified from Xiao and Suppe, 1992).

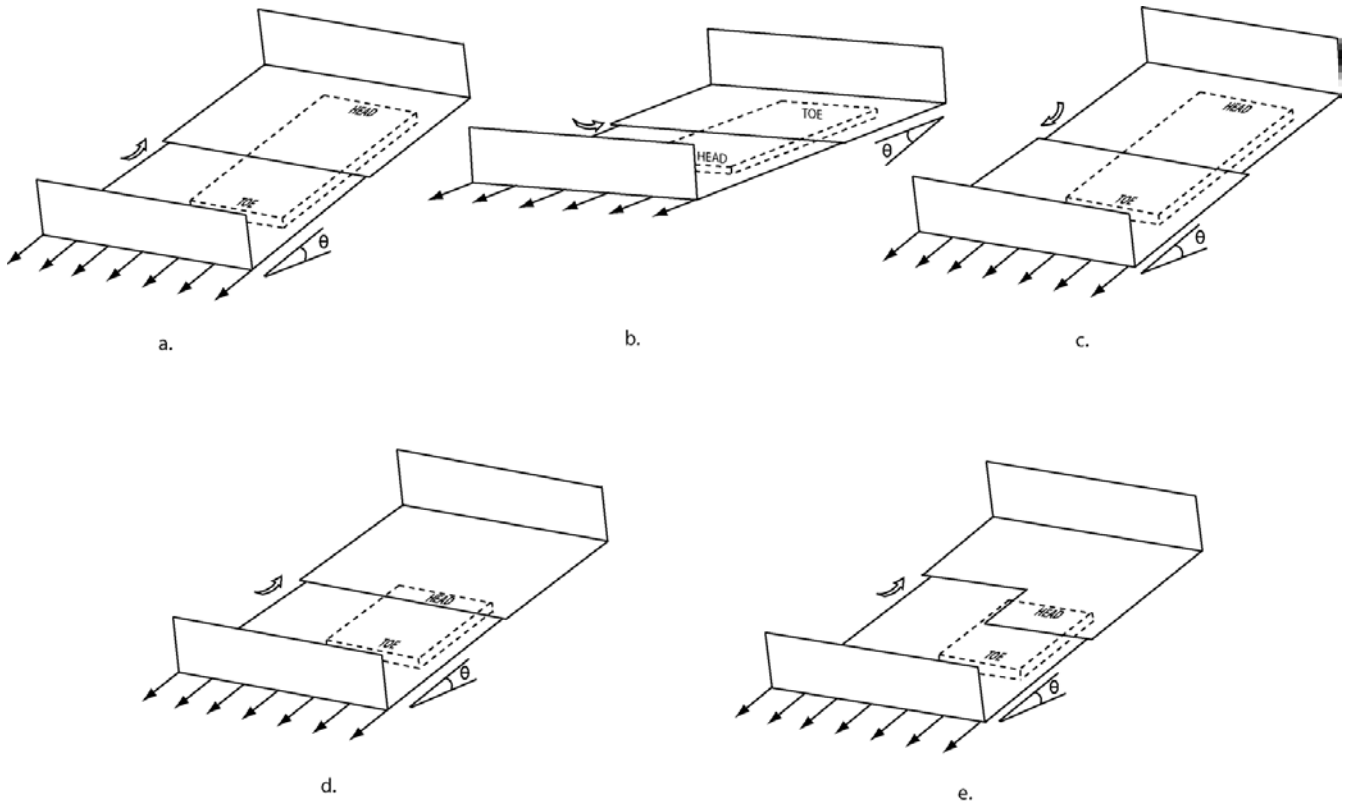

Figure 3.2: Experimental configurations with varying upslope boundary of silicone (Head) with respect to base plate contact and slope with respect to direction of extension (indicated by arrows). Base plate overlap is indicated by curved arrows. (a) Straight edge overlapping plates with slope in the direction of extension. Head of silicone polymer placed far from moveable backstop than base plate contact. (b) Straight edge overlapping plates with slope opposite to direction of extension. Head of silicone polymer placed further from the moveable backstop than the base plate contact. (c) Straight edge overlapping plates with slope in direction of extension. Head of silicone polymer placed further from moveable backstop than base plate contact. (d) Straight edge overlapping plates with slope in direction of extension. Head of silicone placed at same distance from moveable backstop as that of base plate contact. (e) Indented edge overlapping plates with slope in direction of extension. Head of silicone polymer placed closer to moveable backstop than the base plate contact.

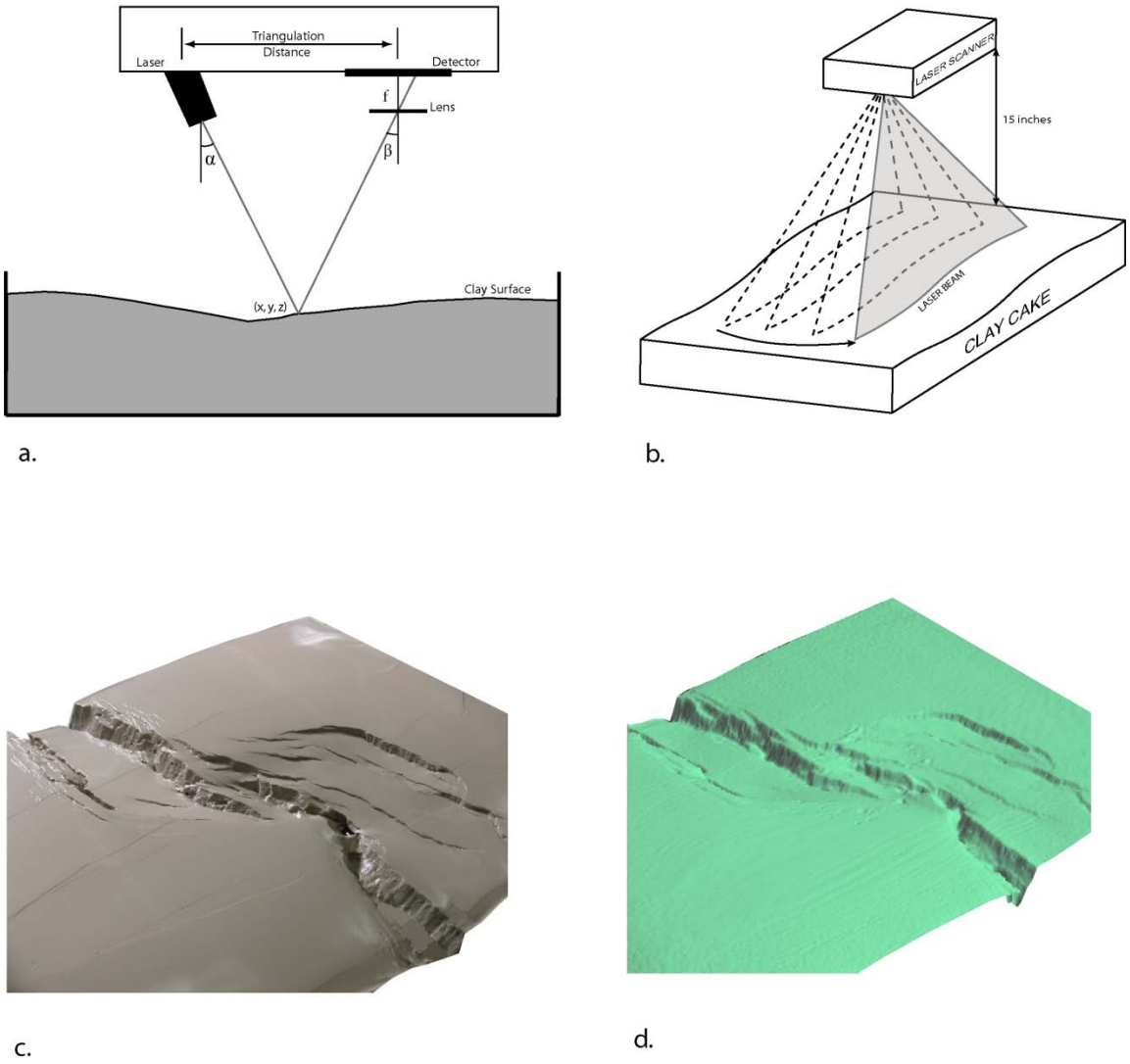

Figure 3.3: (a) Schematic diagram of the working principle of the laser scanner with the triangulation formed by the laser source, the detector and the point on the clay surface where the laser is reflected from. In three dimensions, the point on the surface would be a line. (b) Schematic view of the laser scanner projecting a line laser and sweeping across the clay surface at a constant velocity. (c) Real surface of the clay that has been scanned with the laser scanner. (d) Final virtual surface of the clay recreated from the point cloud.

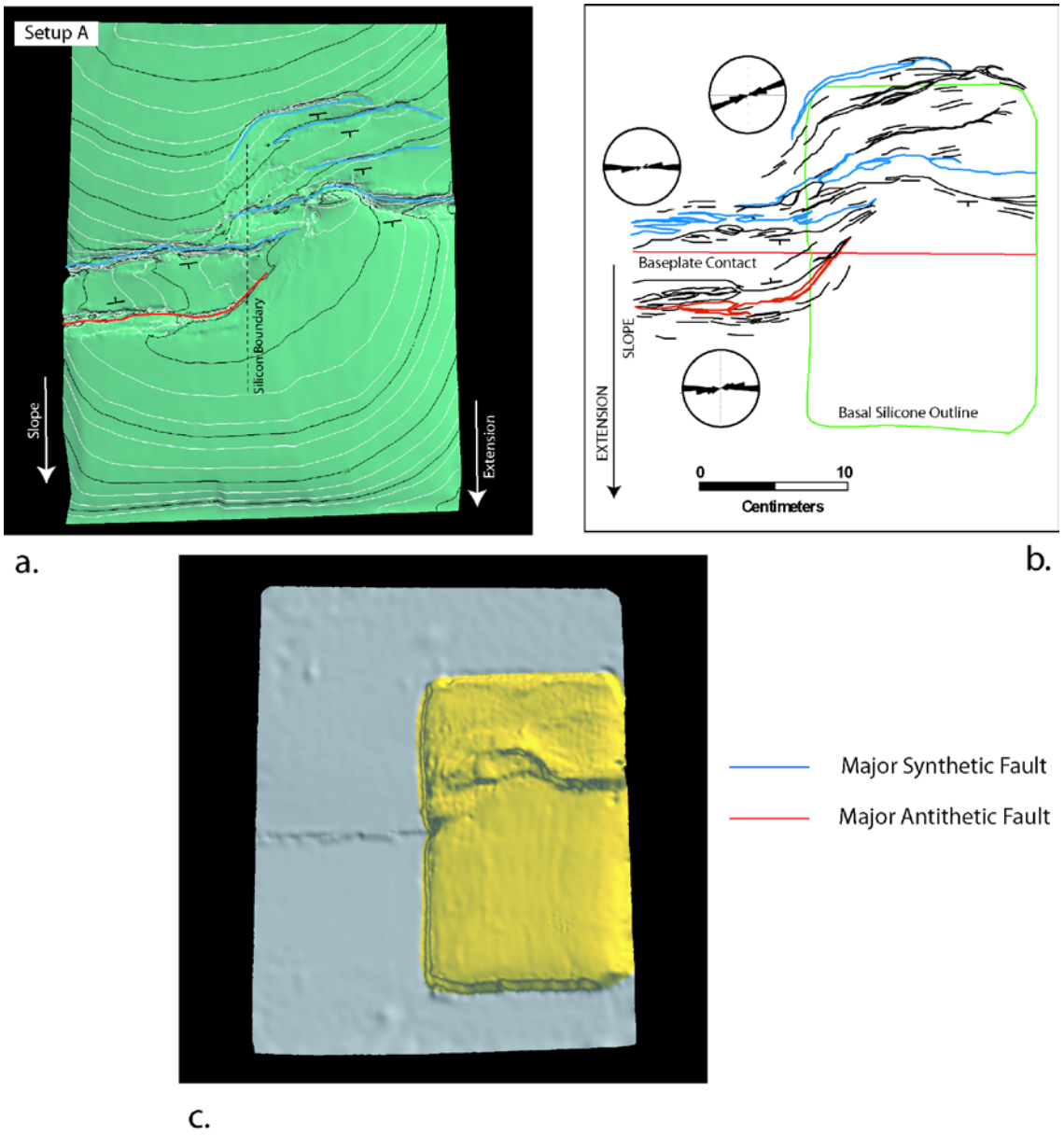

Figure 3.4: (a) 3D structural geometry in the final stages of the Setup A. (b) Fault patterns developed in the final stages of the experiments in Setup A. The changes in orientation of the faults (20°-30°) are depicted in the Rose diagrams showing consistent bending along the boundary of the silicone polymer. (c) 3D geometry of the base plate and basal silicone polymer at the final stages of the experiments showing structural highs and accumulations in the head of the silicone polymer in Setup A.

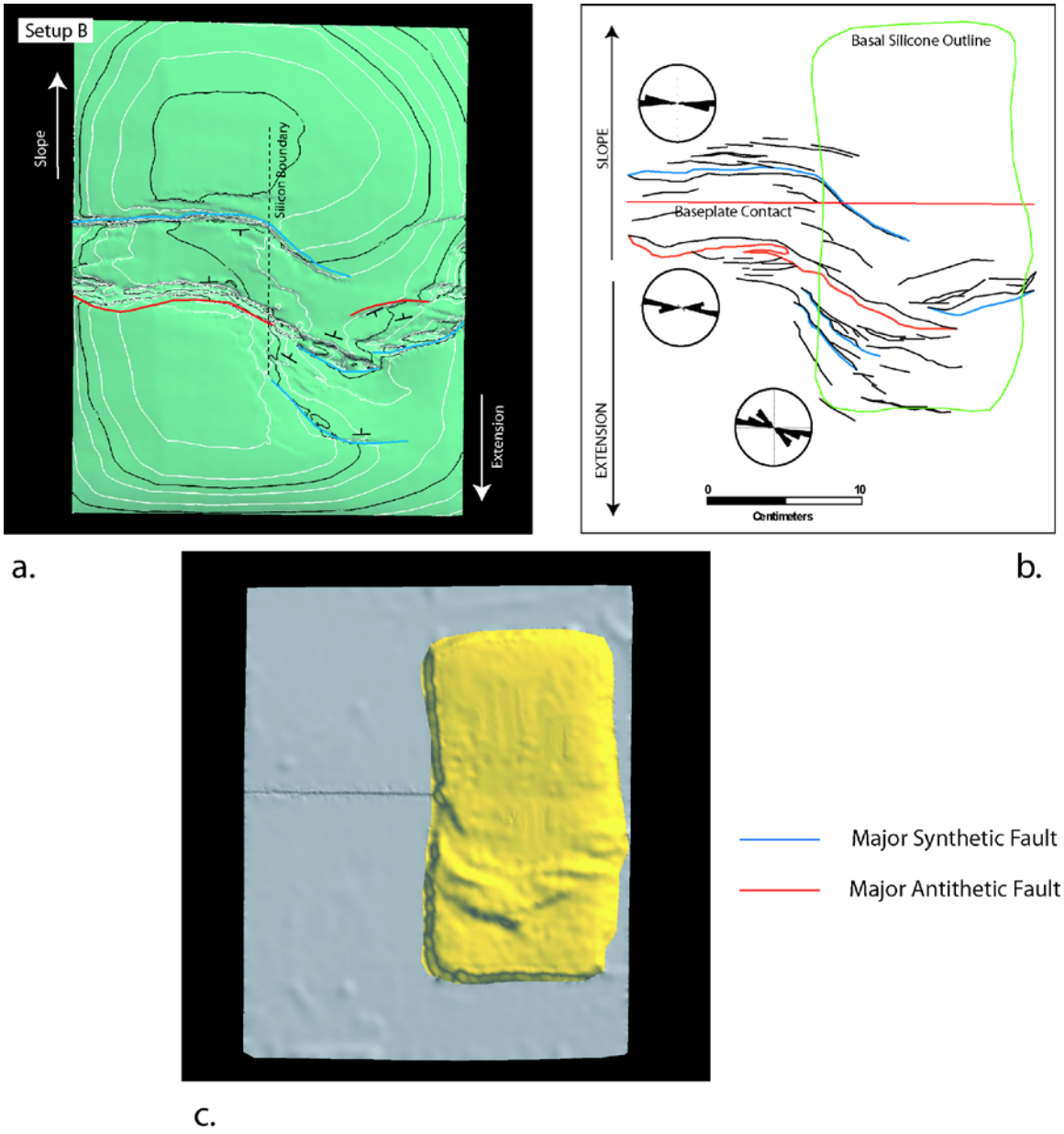

Figure 3.5: (a) 3D structural geometry in the final stages of the Setup B. (b) Fault patterns developed in the final stages of the experiments in Setup B. The changes in orientation of the faults (20°-30°) are depicted in the Rose diagrams showing consistent bending along the boundary of the silicone polymer. (c) 3D geometry of the base plate and basal silicone polymer at the final stages of the experiments showing structural highs and accumulations in the head of the silicone polymer in Setup B.

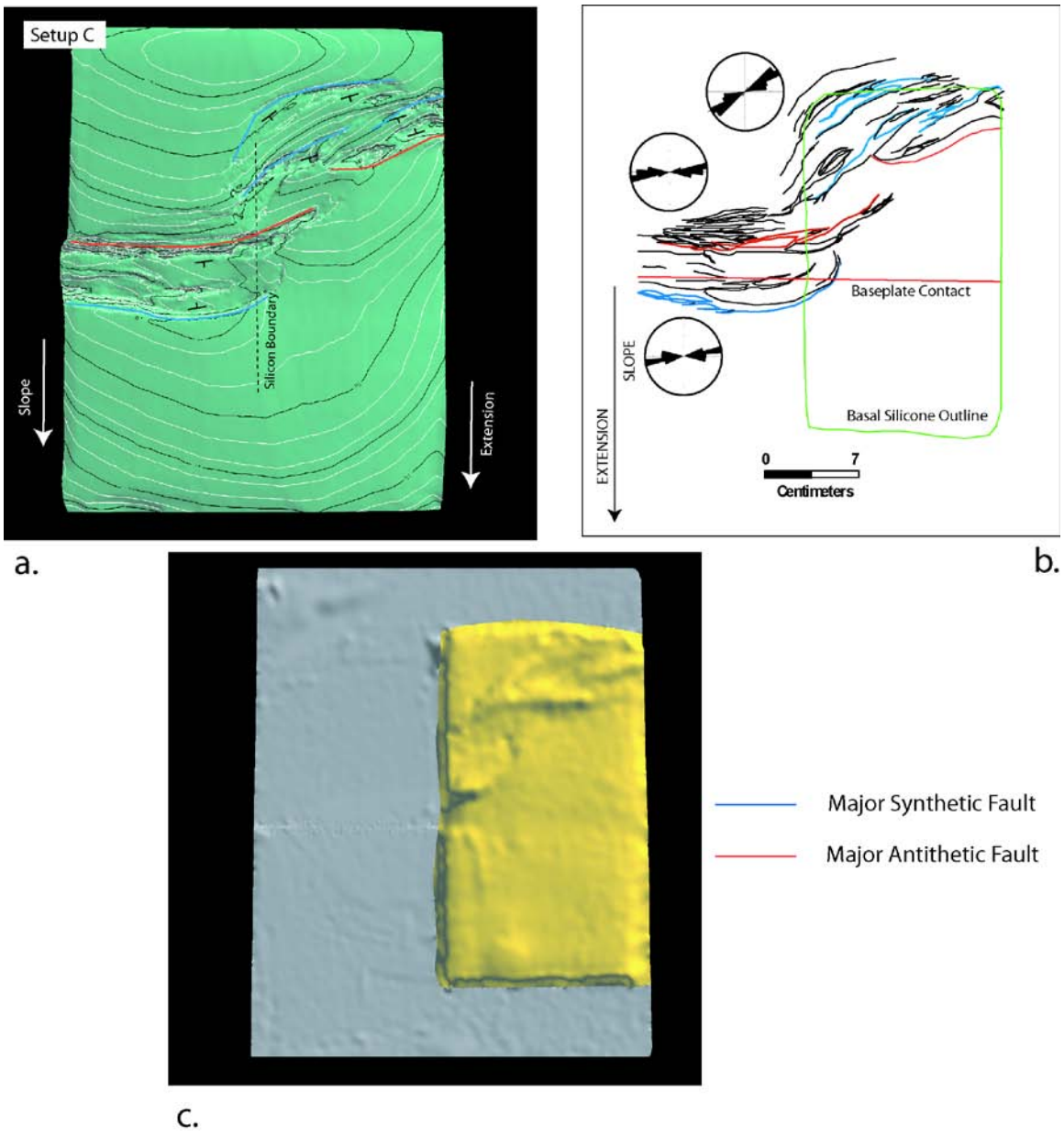

Figure 3.6: (a) 3D structural geometry in the final stages of the Setup C. (b) Fault patterns developed in the final stages of the experiments in Setup C. The changes in orientation of the faults (20°-30°) are depicted in the Rose diagrams showing consistent bending along the boundary of the silicone polymer. (c) 3D geometry of the base plate and basal silicone polymer at the final stages of the experiments showing structural highs and accumulations in the head of the silicone polymer in Setup C.

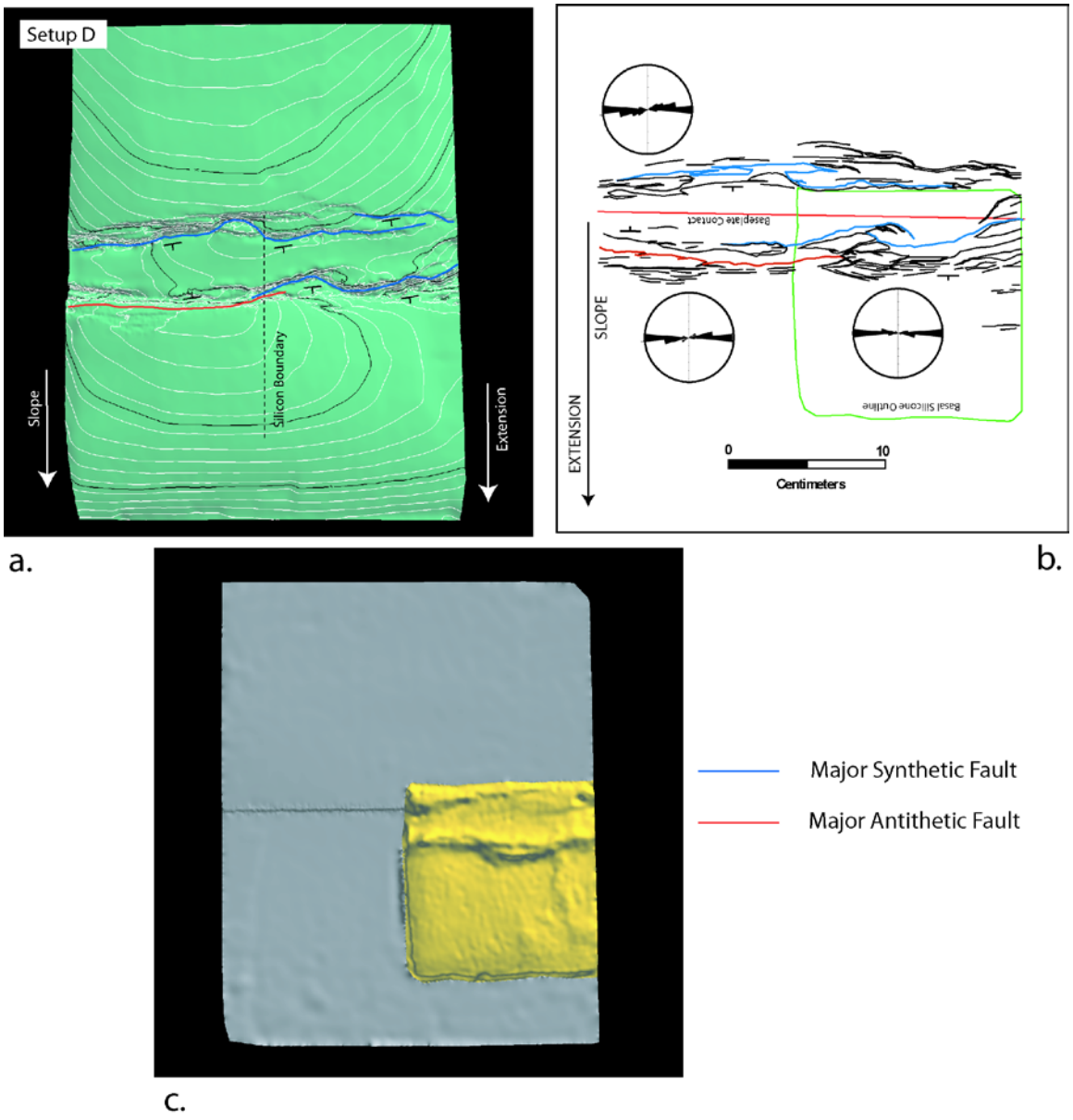

Figure 3.7: (a) 3D structural geometry in the final stages of the Setup D. The dip directions of the faults are marked along with the directions of extension and slope. The transfer zones form at the boundary of the silicone polymer. (b) Fault patterns developed in the final stages of the experiments in Setup D. No change of orientation of faults in setup D within the transfer zones are depicted in the Rose diagrams. (c) 3D geometry of the base plate and basal silicone polymer at the final stages of the experiments showing structural highs and accumulations in the head of the silicone polymer in Setup D.

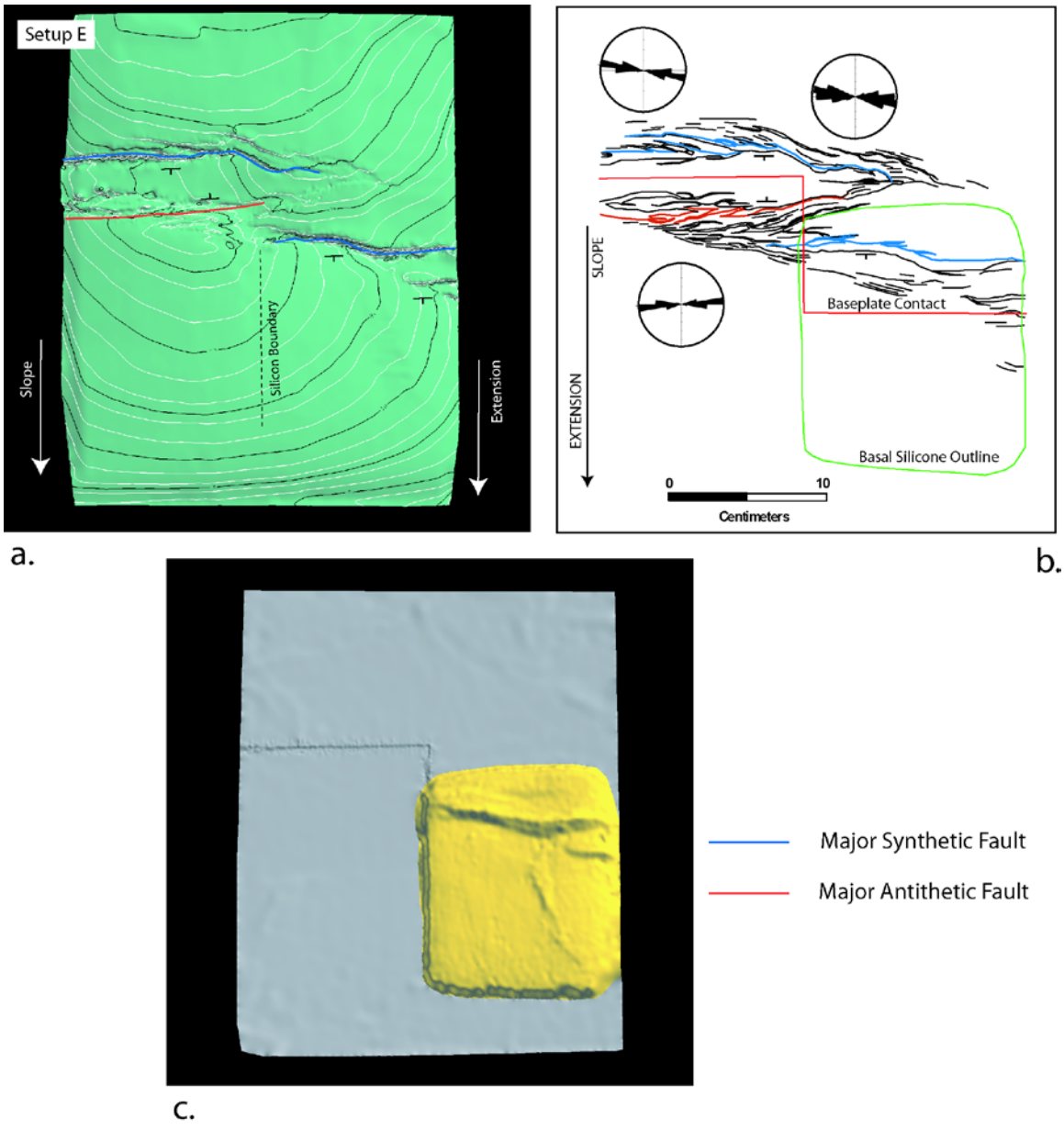

Figure 3.8: (a) 3D structural geometry in the final stages of the Setup E. The dip directions of the faults are marked along with the directions of extension and slope. The transfer zones form at the boundary of the silicone polymer. (b) Fault patterns developed in the final stages of the experiments in Setup E. Little change (5°-10°) of orientation of faults within the transfer zones are depicted in the Rose diagrams. (c) 3D geometry of the base plate and basal silicone polymer at the final stages of the experiments showing structural highs and accumulations in the head of the silicone polymer in Setup E.

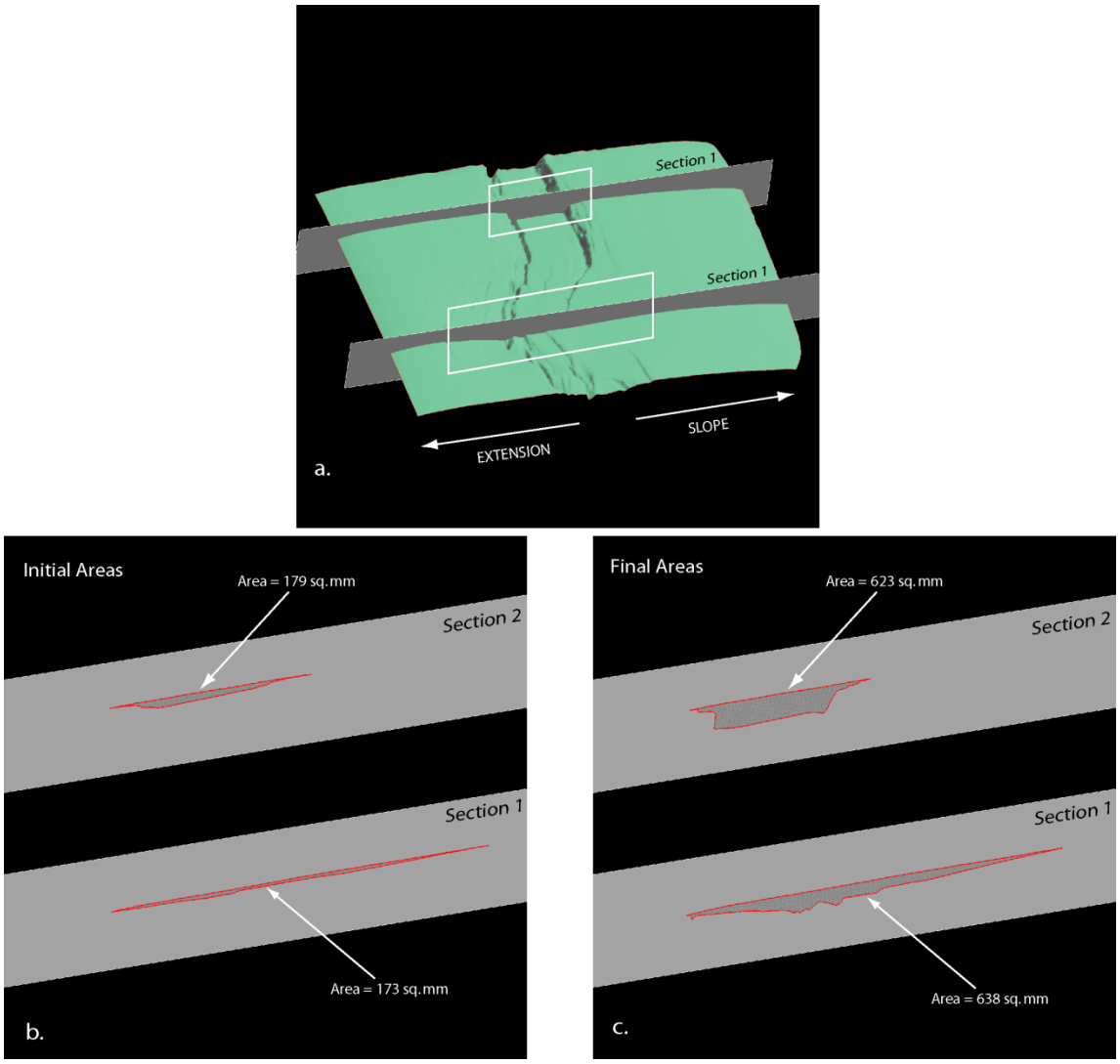

Figure 3.9: (a) Locations of two cross sections across the surface of clay in the final stage of experimental Setup B. (b) Areas within the cross sections 1 and 2, bounded by the undeformed stage and the initial deformed stage, reveal similar values of 173 and 179 square mm respectively. (b) Areas within cross sections 1 and 2, bounded by the undeformed stage and final deformed stage, show similar values of 638 and 623 square mm.

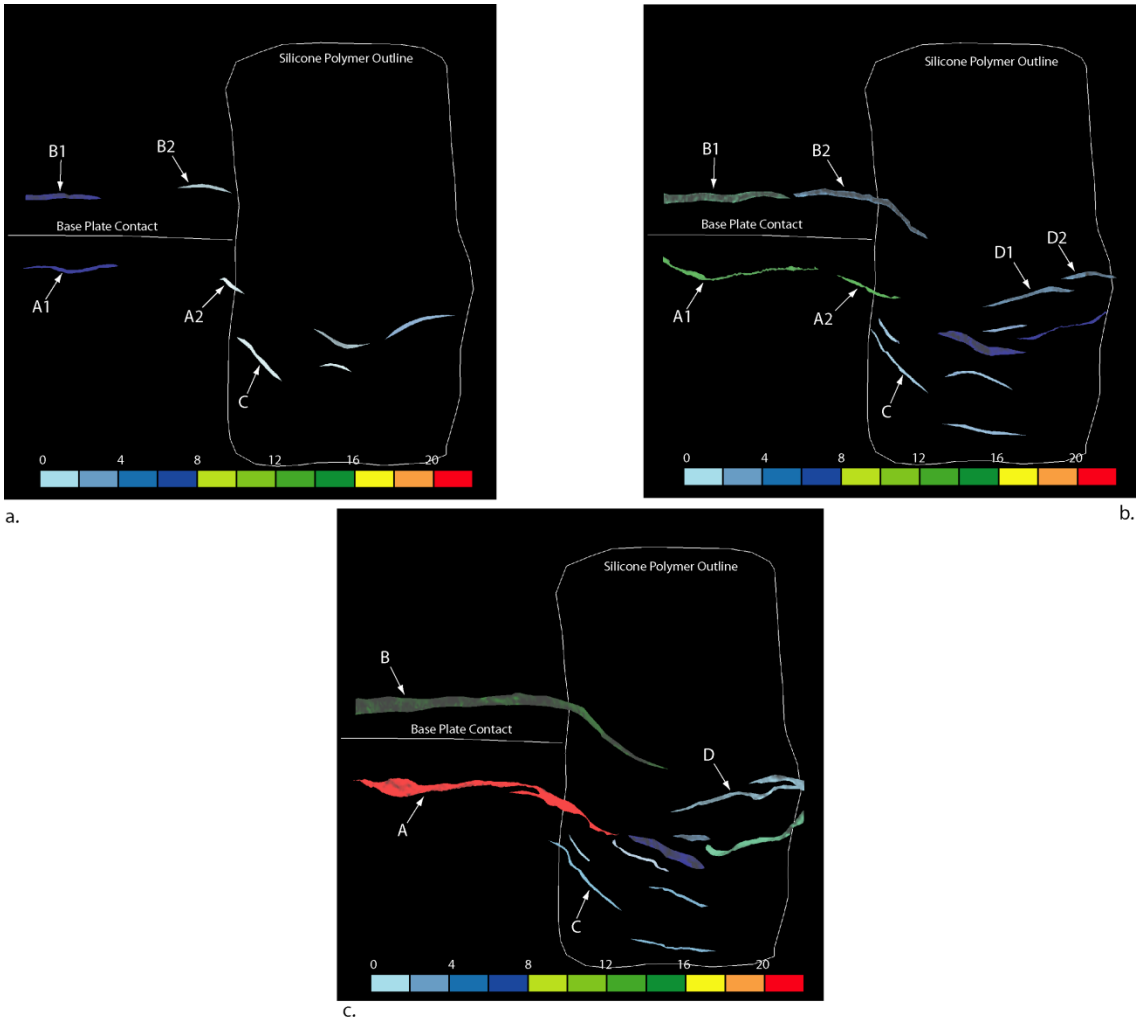

Figure 3.10: (a-c) Incremental stages of fault scarp growth (view from top) in experimental Setup B displaying lateral growth and connectivity between faults. The fault scarps are color coded with respect to the amounts of individual throw. Faults A, B and D form by the growth and coalescence of A1-A2, B1-B2 and D1-D2 respectively. Fault C being at an angle to extension, has limited growth. (d-f) View perpendicular to Fault A showing fault nucleation, lateral connectivity and extension accommodation.

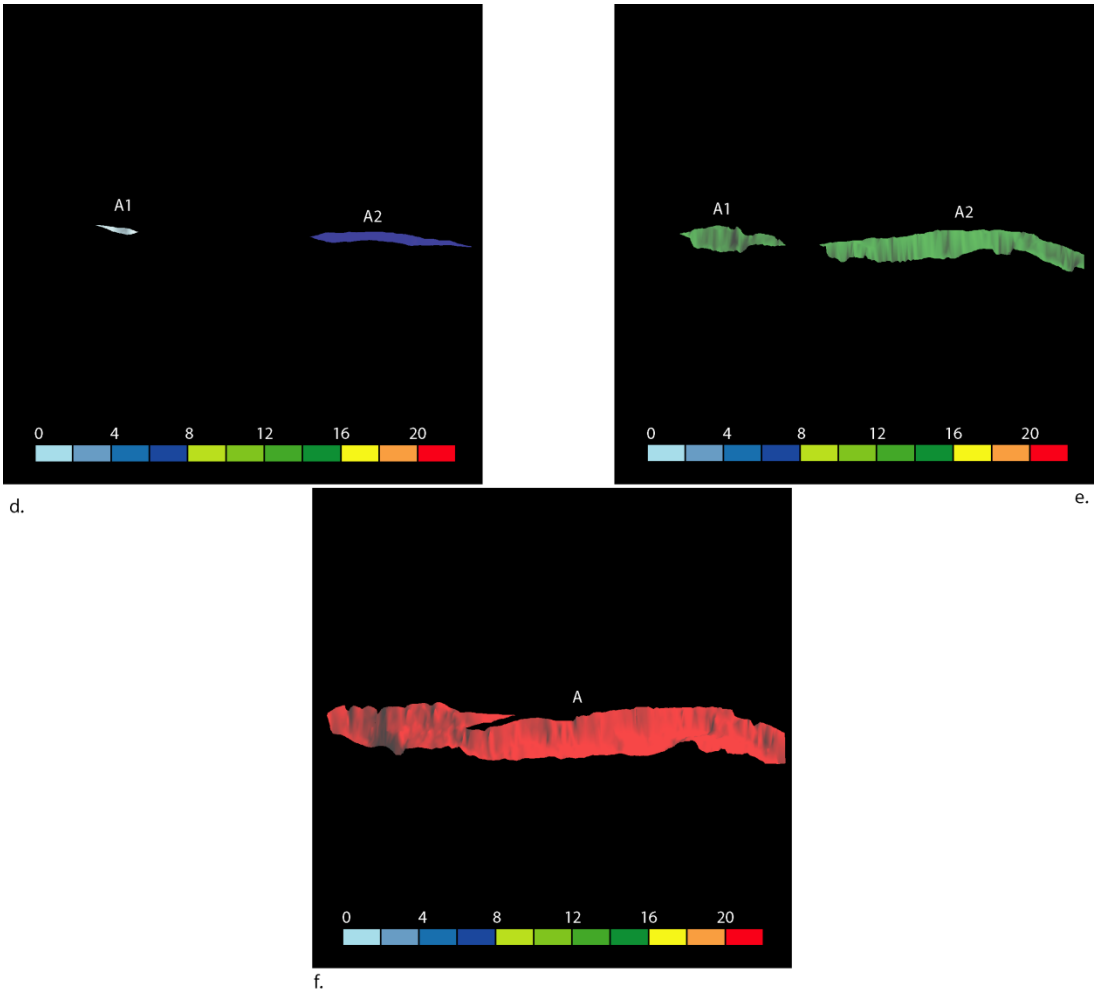

Figure 3.10: (d-f) View perpendicular to Fault A showing fault nucleation, lateral connectivity and extension accommodation.

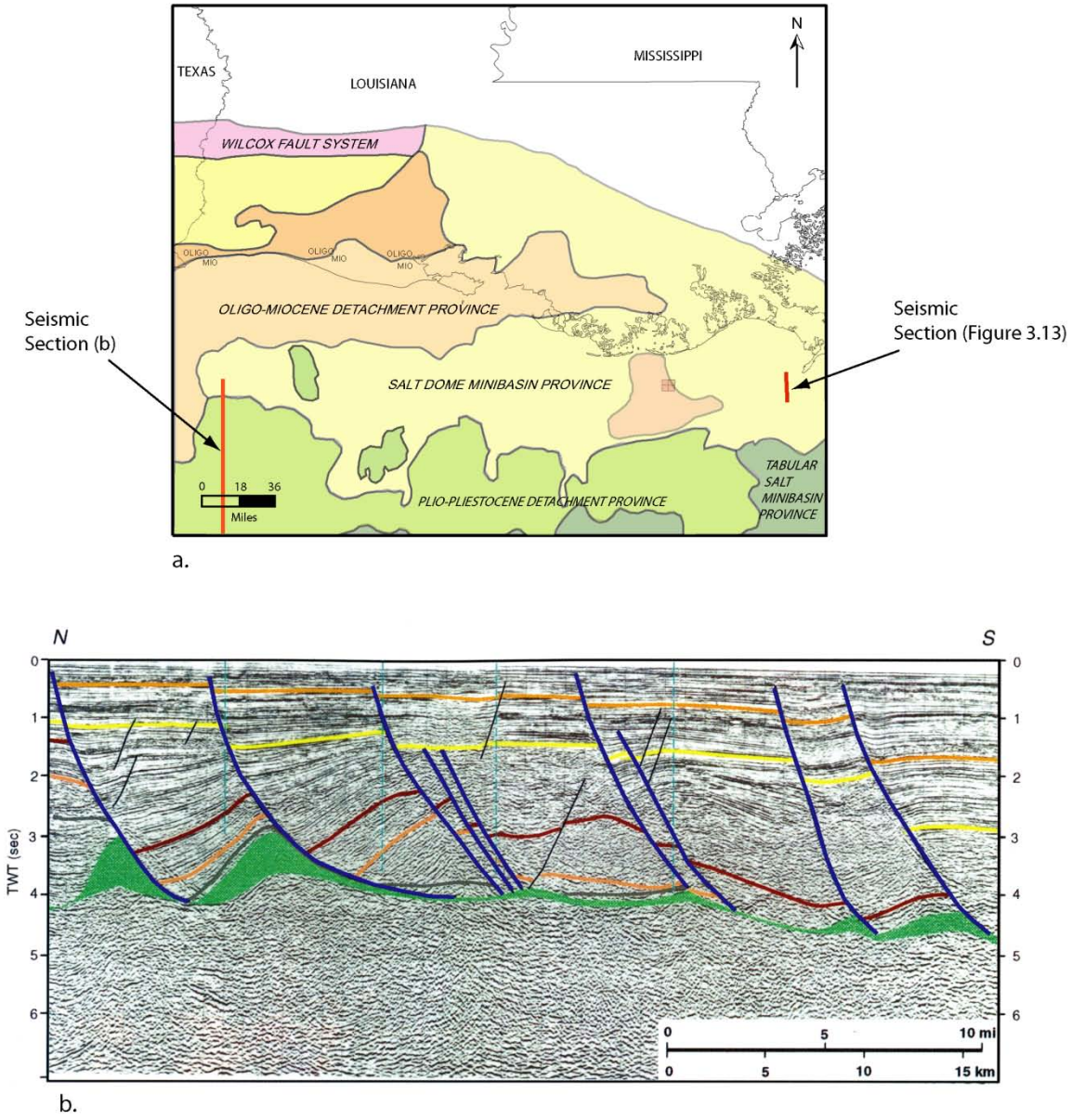

Figure 3.11: (a) Locations of regional seismic lines in the shallow water Gulf of Mexico, offshore Louisiana. (b) Typical Roho style of faulting with a series of basinward dipping listric growth faults detaching at the shallow allochthonous salt sheet. (Modified from Diegel et al., 1995)

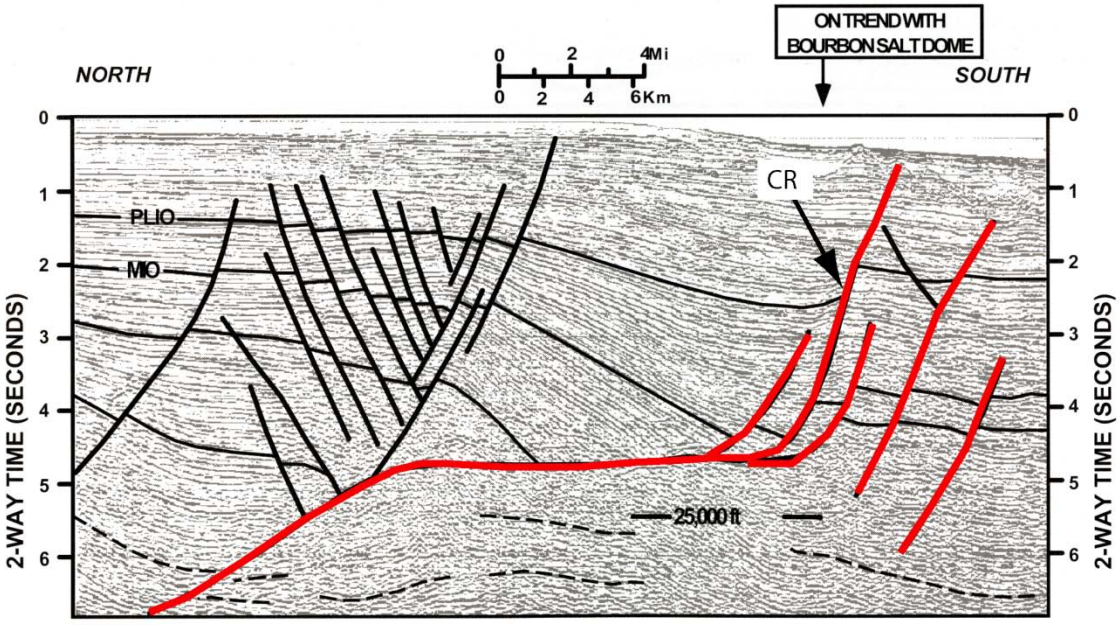

Figure 3.12: Seismic sections across the Bourbon Dome, offshore Louisiana showing Counterregional fault system (CR) forming at the upslope boundary of the salt body. The salt has been completely evacuated and the section shows a basal slope along the detachment. Location of section in Figure 4.12. (Modified from Schuster, 1995)

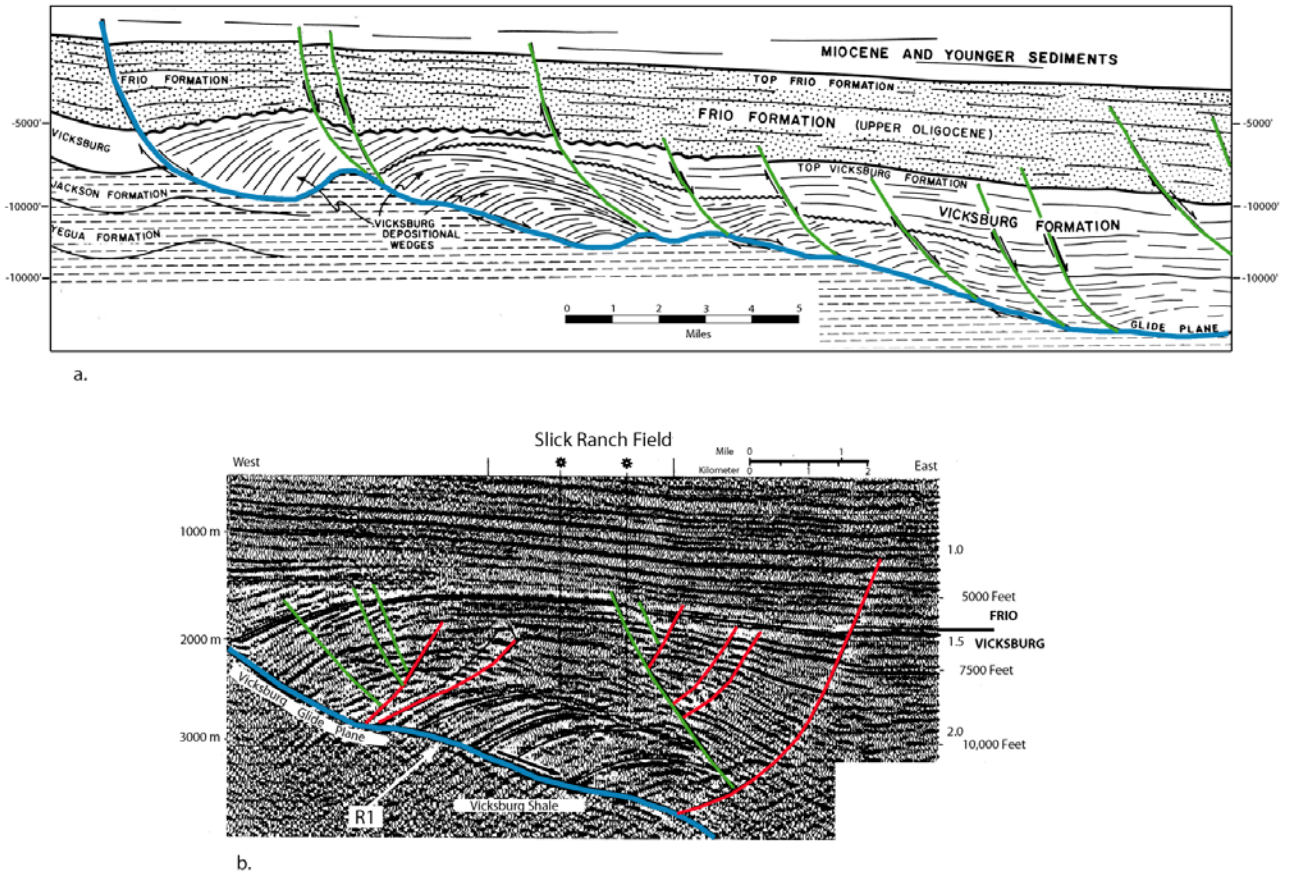

Figure 3.13: (a) Line drawing of seismic section showing typical fault geometries in a homogeneous sedimentary package in Slick Ranch field, Texas. (b) Seismic section across the Slick Ranch field, Texas showing large basinward dipping listric normal fault (blue), known as the Vicksburg Glide Place (R1) and secondary synthetic (green) and antithetic (red) faults formed in the hanging wall. Master fault is less listric and contains more secondary faults as also observed in the experiments.

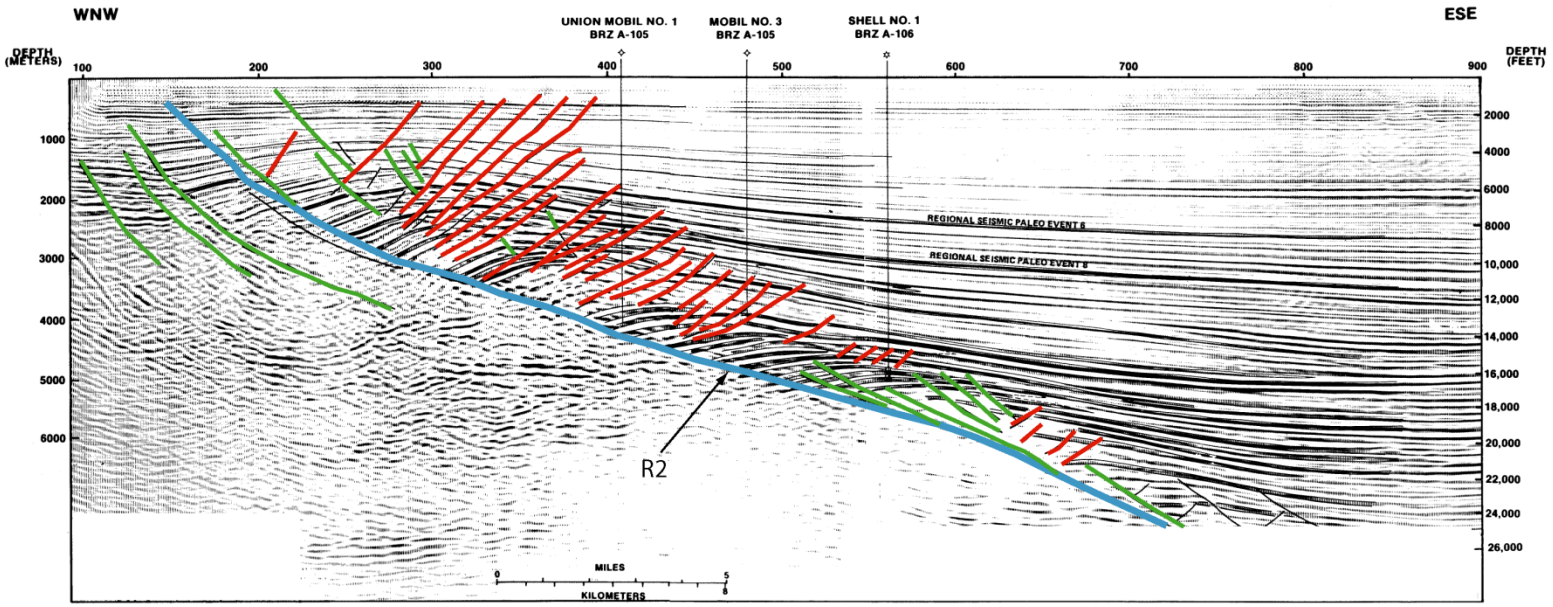

Figure 3.14: Seismic section across the Brazos Ridge, Texas showing major basinward dipping fault, R1 (blue) and numerous secondary antithetic faults (red) and fewer synthetic (green) faults.

APPENDIX A

TERMINOLOGY

TERMS	DEFINITIONS
Transfer Zone	Area between two adjacent faults where accommodation of deformation from the two faults takes place.
Convergent Transfer Zone	Transfer zone formed between two faults dipping towards each other.
Divergent Transfer Zone	Transfer zone formed between two faults dipping away from each other.
Synthetic Transfer Zone	Transfer zone between two faults dipping in the same direction.
Primary Synthetic Fault	Large displacement fault that is attached to the overlying base plate and dips towards the underlying base plate.
Secondary Synthetic Faults	Small displacement faults dipping in the same direction as the Primary Synthetic Fault.
Primary Antithetic Fault	Large displacement fault that is attached to the underlying base plate and dips towards the overlying base plate.
Secondary Antithetic Faults	Small displacement faults parallel dipping in the same direction as the Primary Antithetic Fault.
Regional Fault	Large fault dipping towards the direction of extension.
Counterregional Fault	Large displacement fault dipping away from extension direction.
Salt Weld	When sedimentary layers overlying and underlying a salt body come in contact after complete salt evacuation, it forms a salt weld.

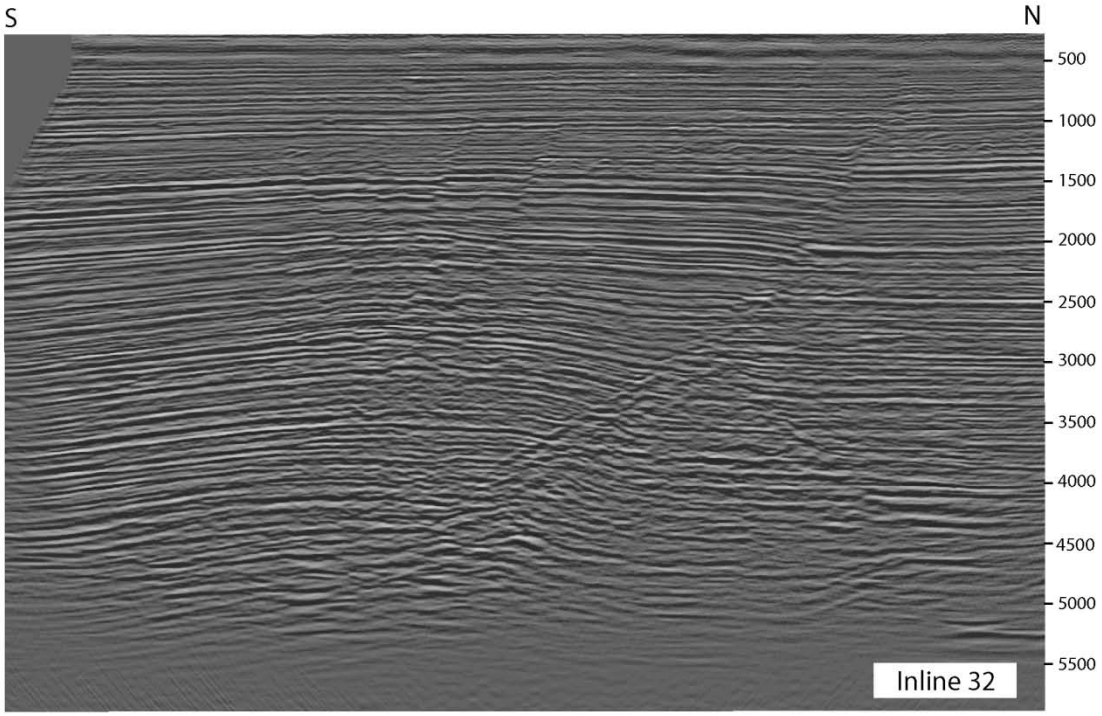

a.

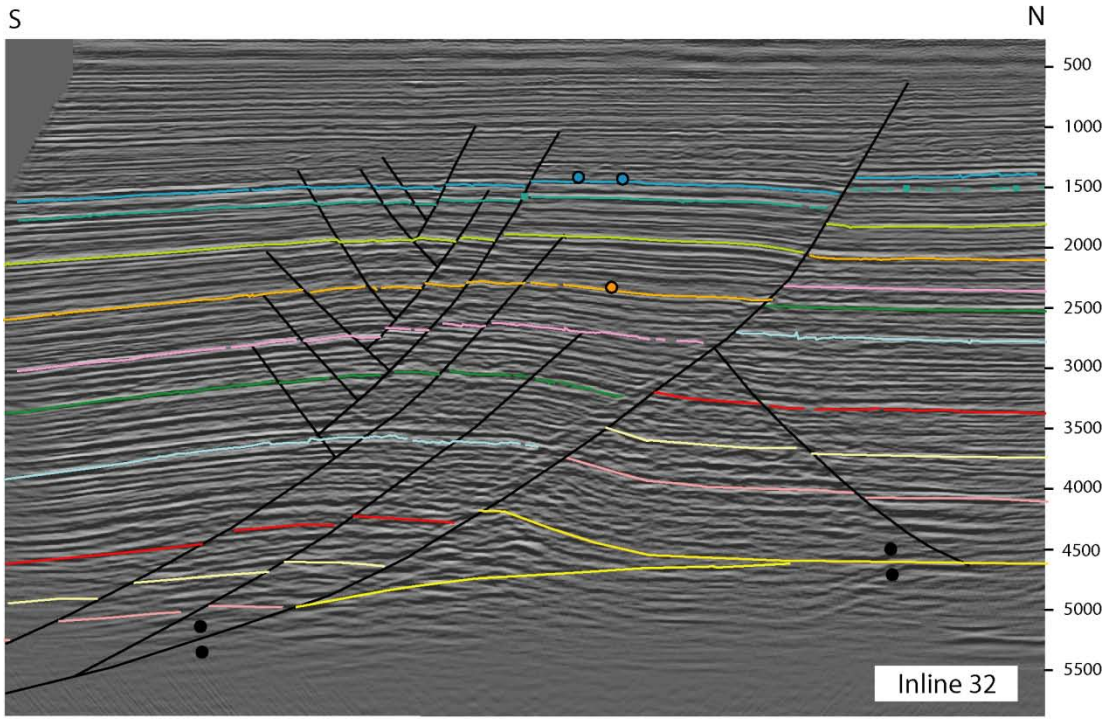

b.

Figure A1: (a) Uninterpreted Inline 32 in time (ms). (b) Interpreted Inline 32 in time (ms). Well tops of horizons color coded according to Figure 2.4 in Chapter 2.

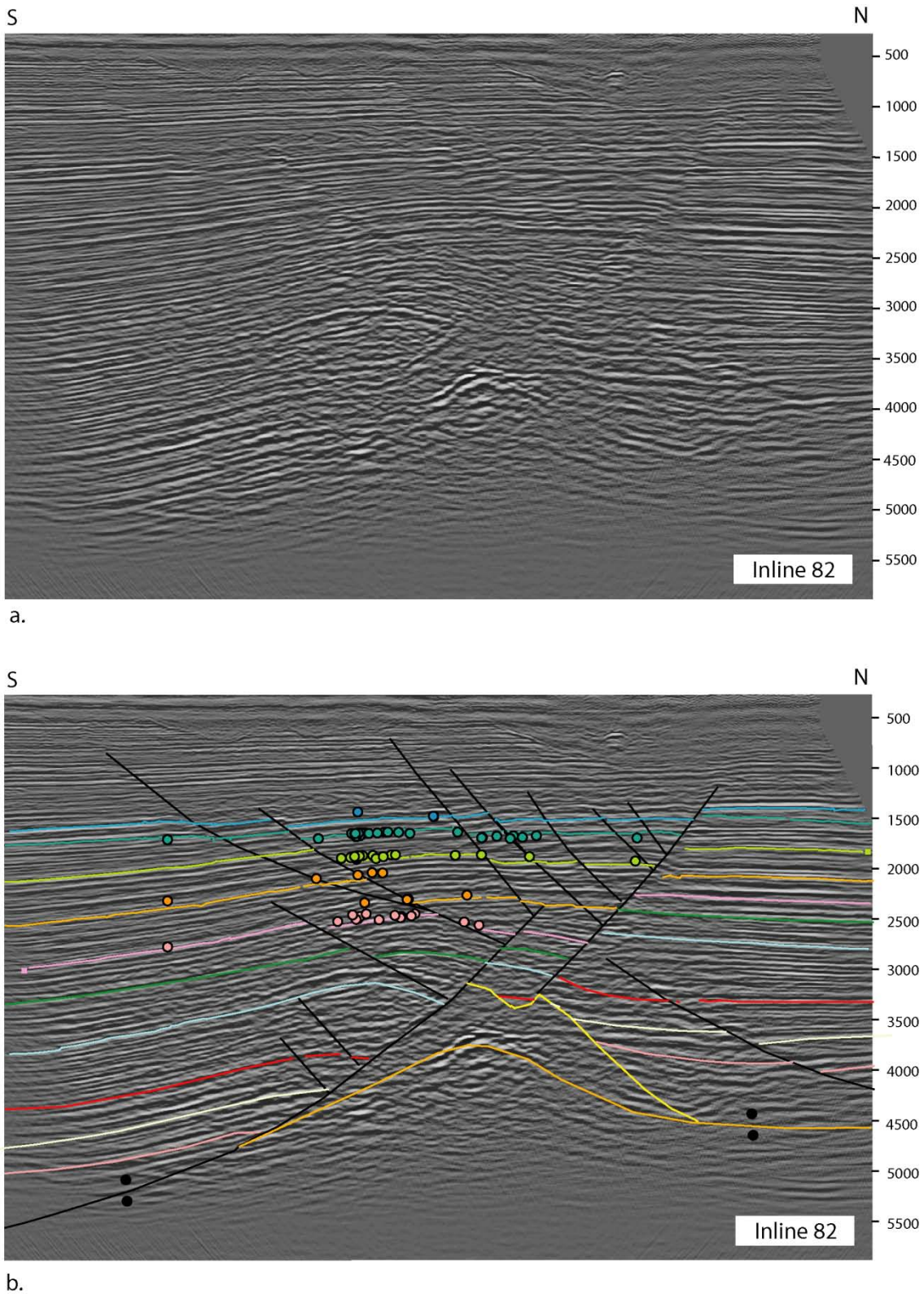

Figure A2: (a) Uninterpreted Inline 82 in time (ms). (b) Interpreted Inline 82 in time (ms). Well tops of horizons color coded according to Figure 2.4 in Chapter 2.

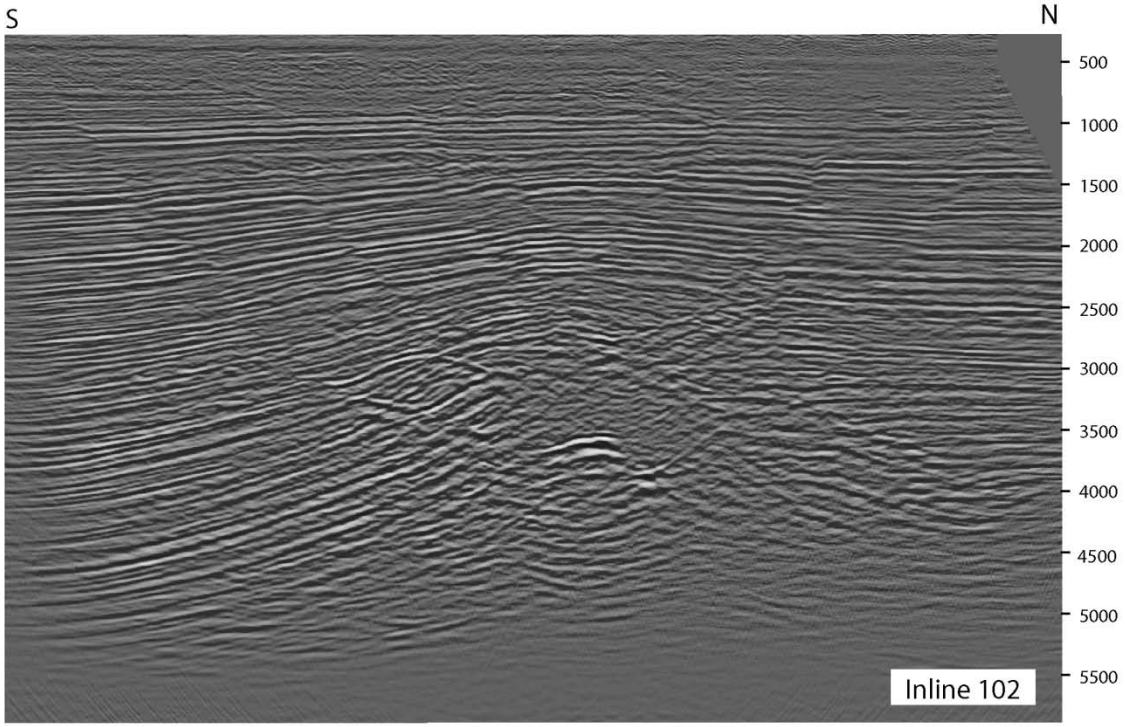

a.

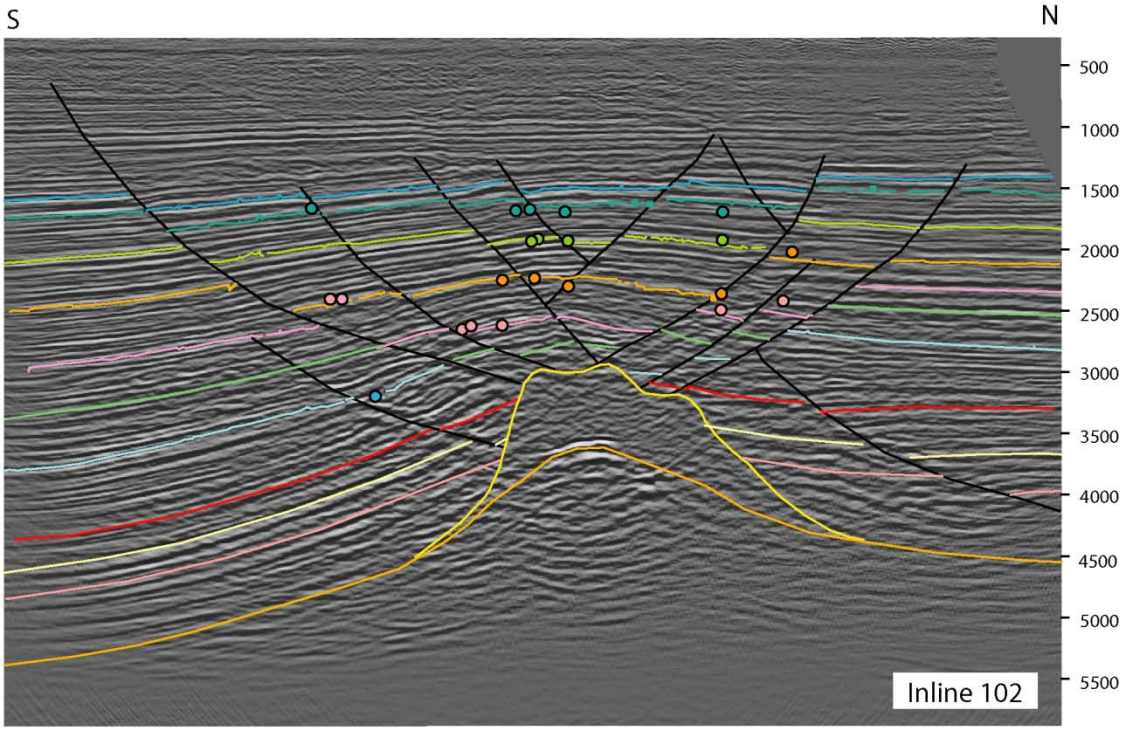

b.

Figure A3: (a) Uninterpreted Inline 102 in time (ms). (b) Interpreted Inline 102 in time (ms). Well tops of horizons color coded according to Figure 2.4 in Chapter 2.

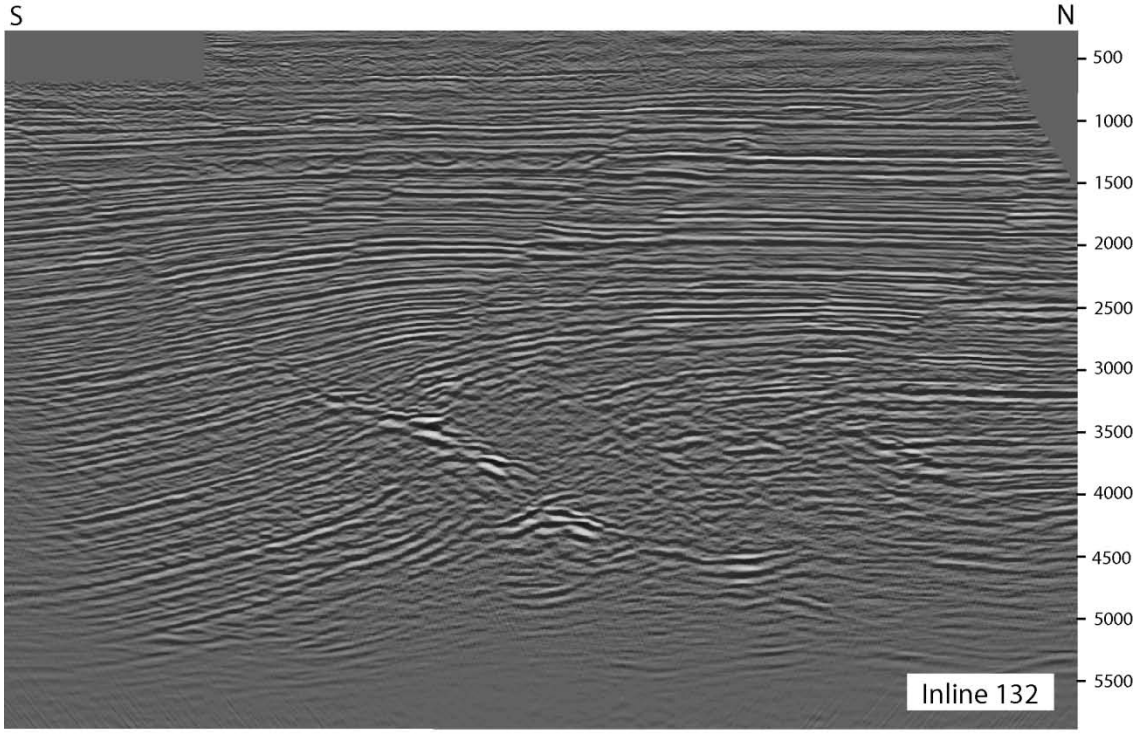

a.

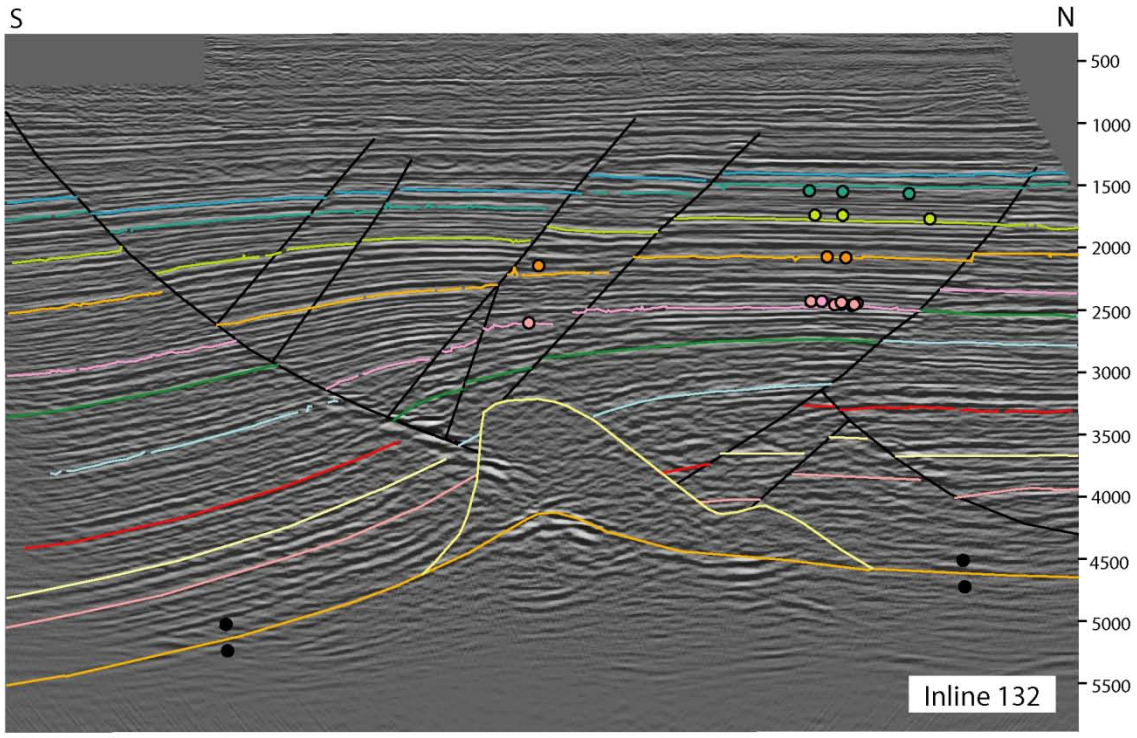

b.

Figure A4: (a) Uninterpreted Inline 132 in time (ms). (b) Interpreted Inline 132 in time (ms). Well tops of horizons color coded according to Figure 2.4 in Chapter 2.

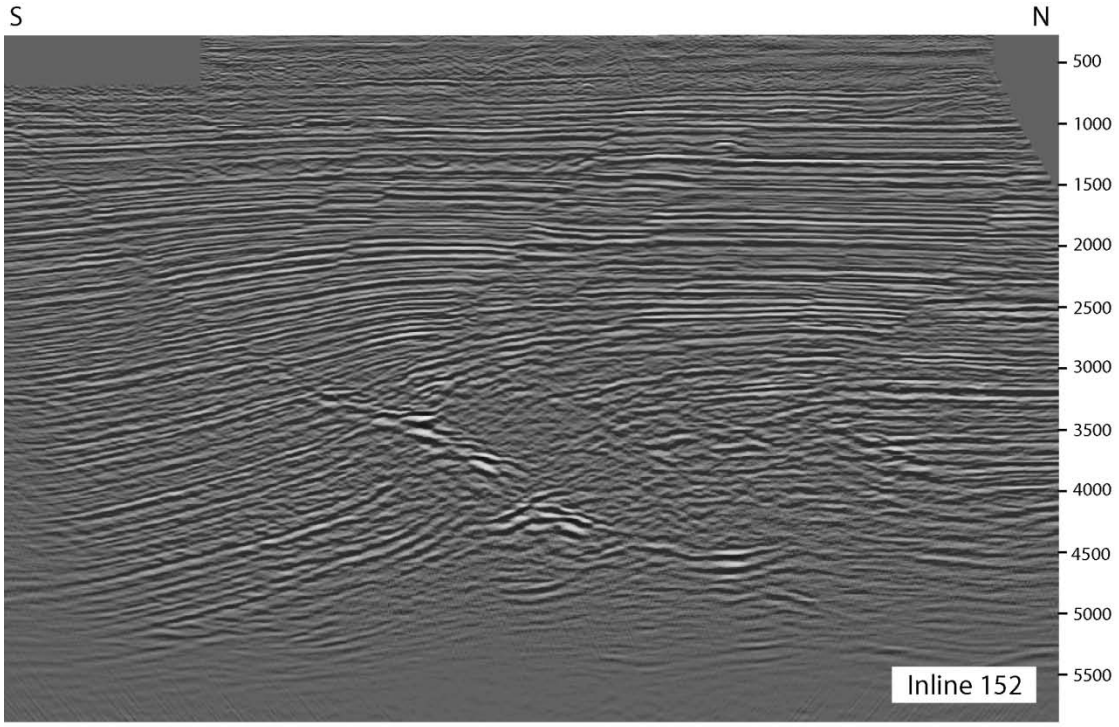

a.

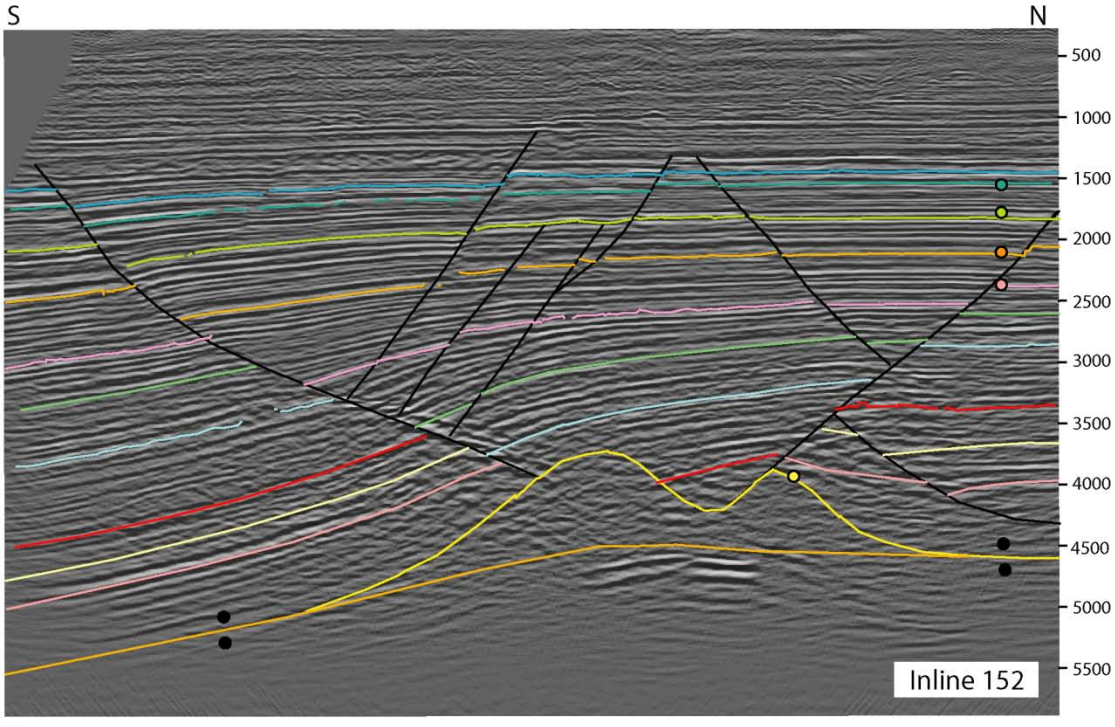

b.

Figure A5: (a) Uninterpreted Inline 152 in time (ms). (b) Interpreted Inline 152 in time (ms). Well tops of horizons color coded according to Figure 2.4 in Chapter 2.

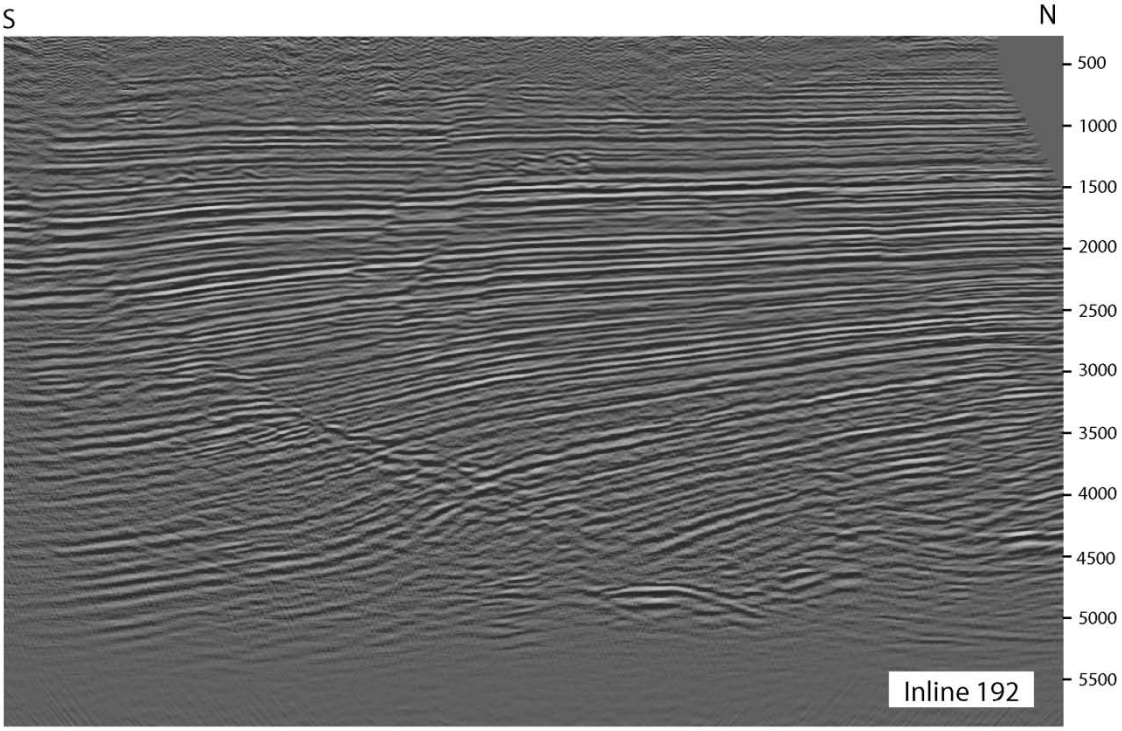

a.

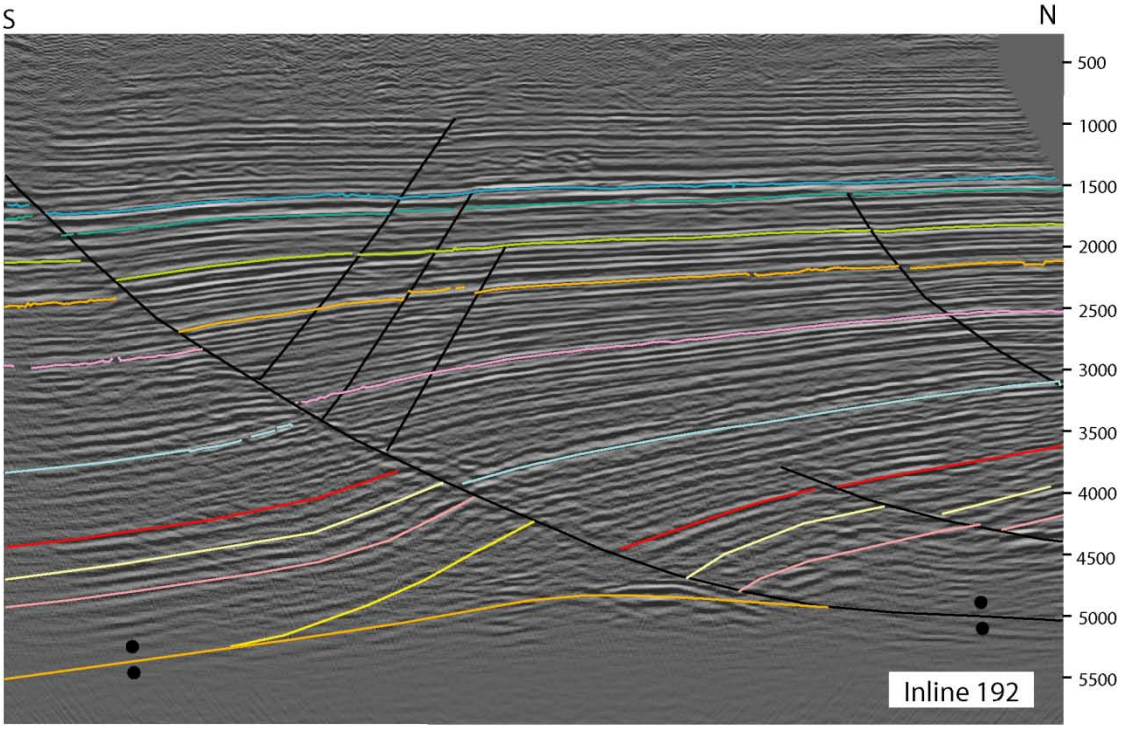

b.

Figure A6: (a) Uninterpreted Inline 192 in time (ms). (b) Interpreted Inline 192 in time (ms). Well tops of horizons color coded according to Figure 2.4 in Chapter 2.

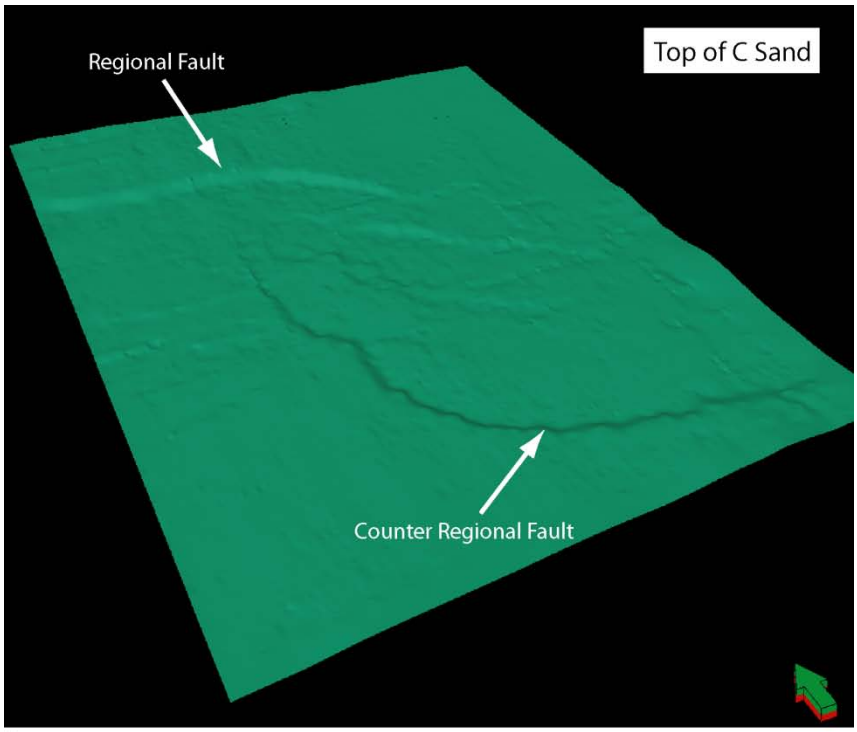

a.

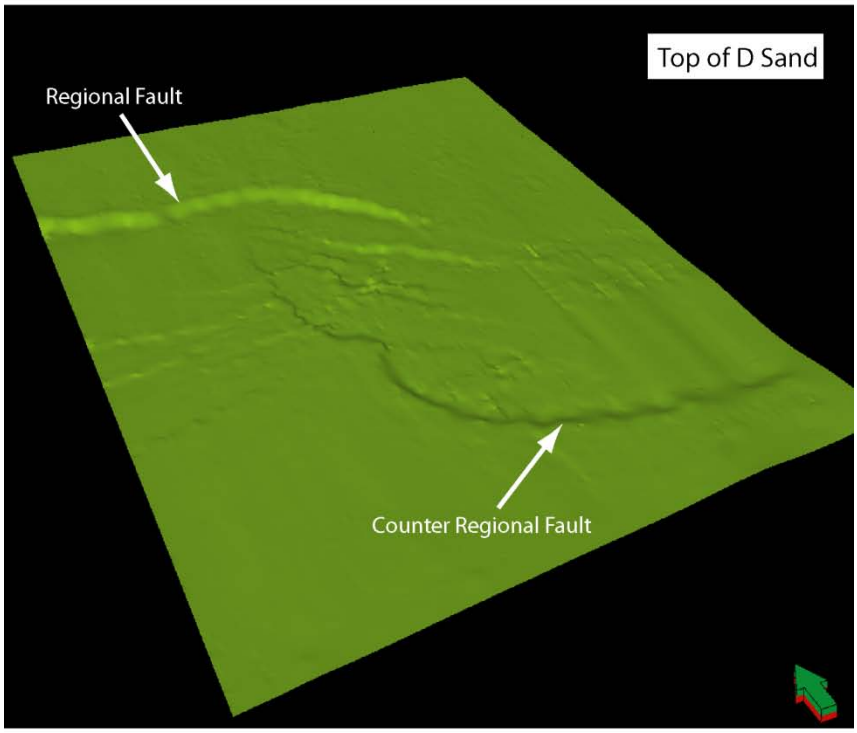

b.

Figure A7: Time surfaces created from interpreting inlines and crosslines for (a) C Sand and (b) D Sand. These surfaces were used as input for depth converted surfaces.

APPENDIX B

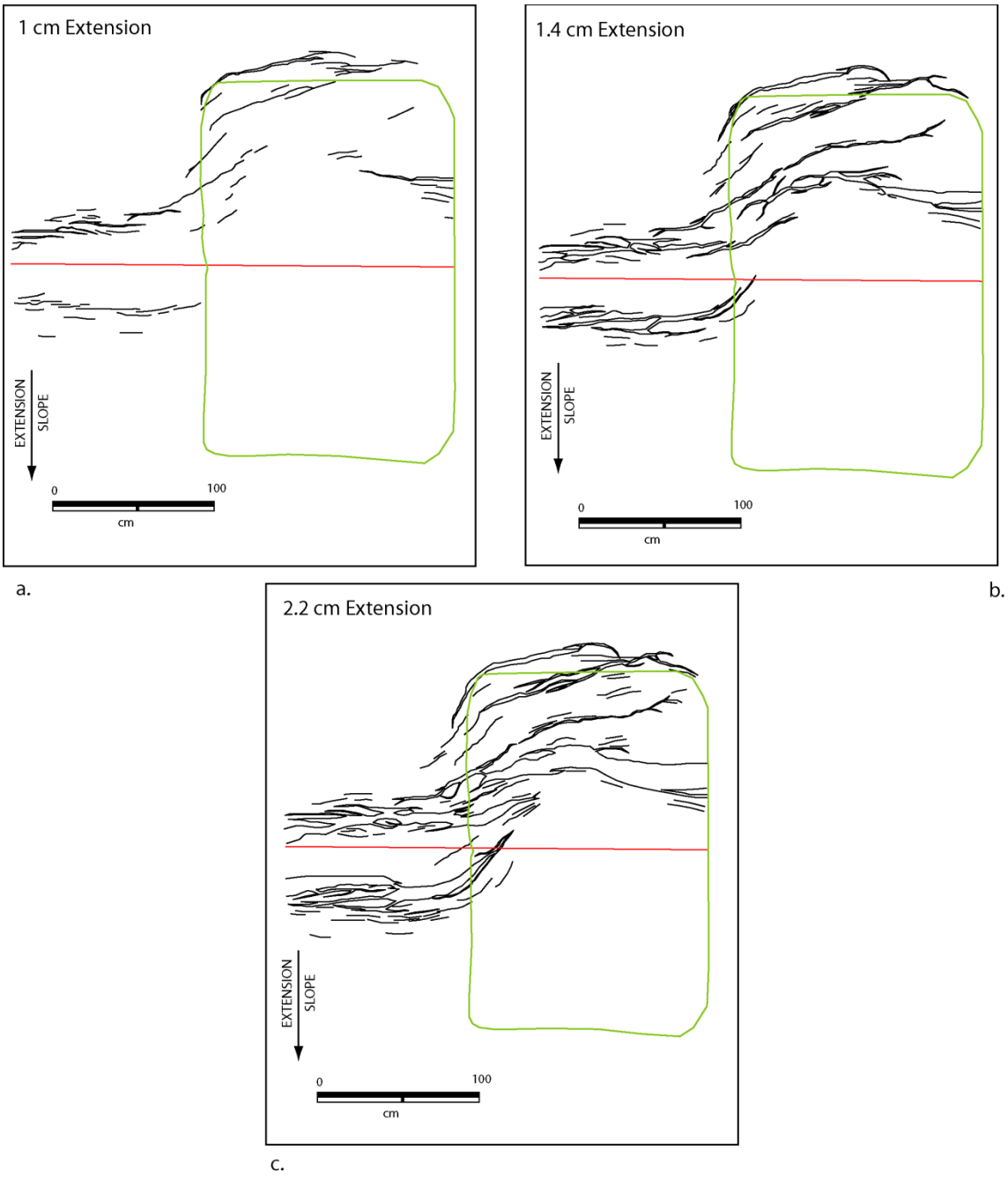

Figure B1: (a-c) Incremental stages of extension showing fault growth and patterns in setup A. Base plate contact is marked with red and the outline of the silicone polymer by green.

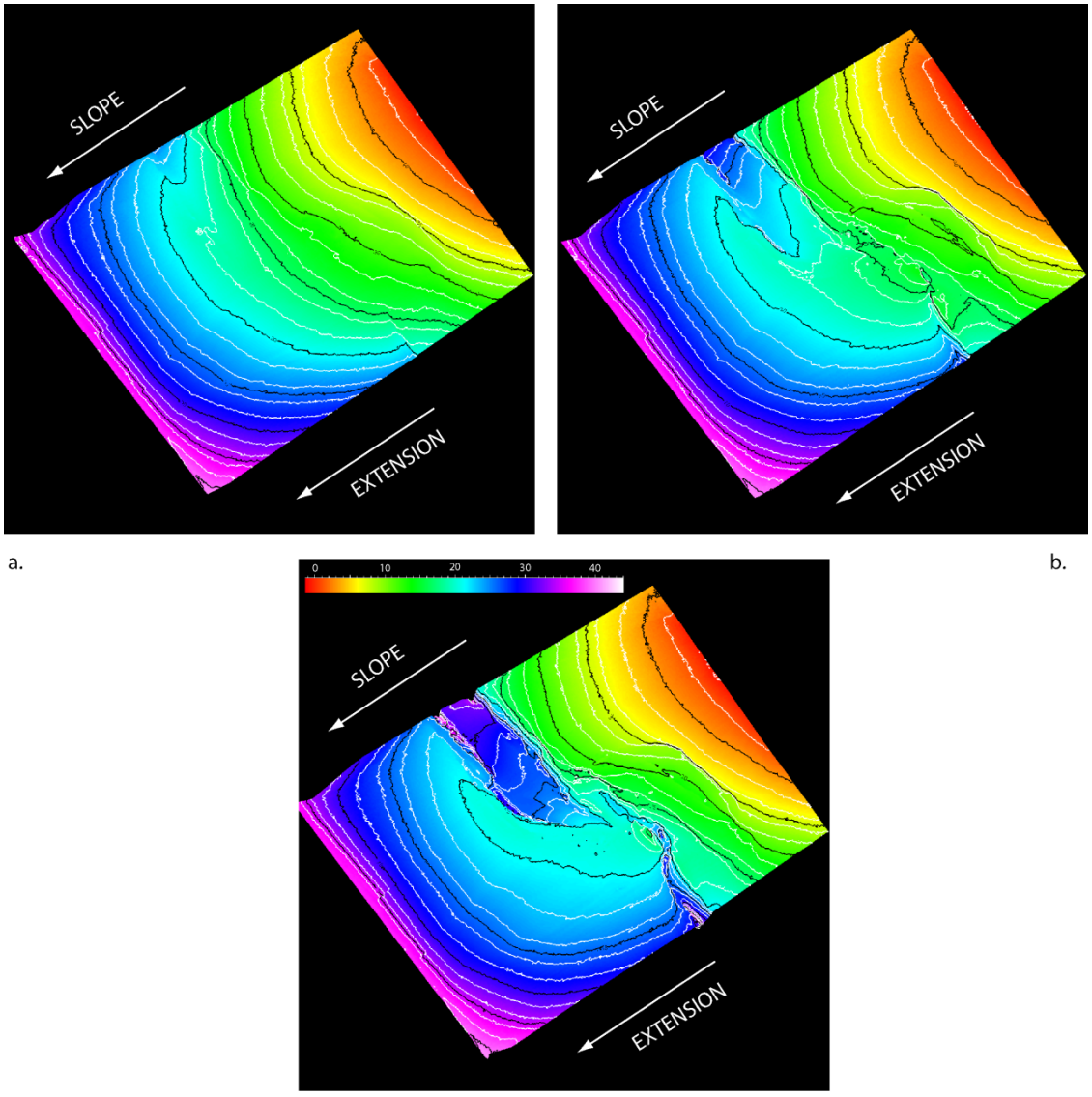

Figure B2: Three dimensional geometry of the clay surface through the stages of extension in setup A. High areas indicated by red and lows by blue.

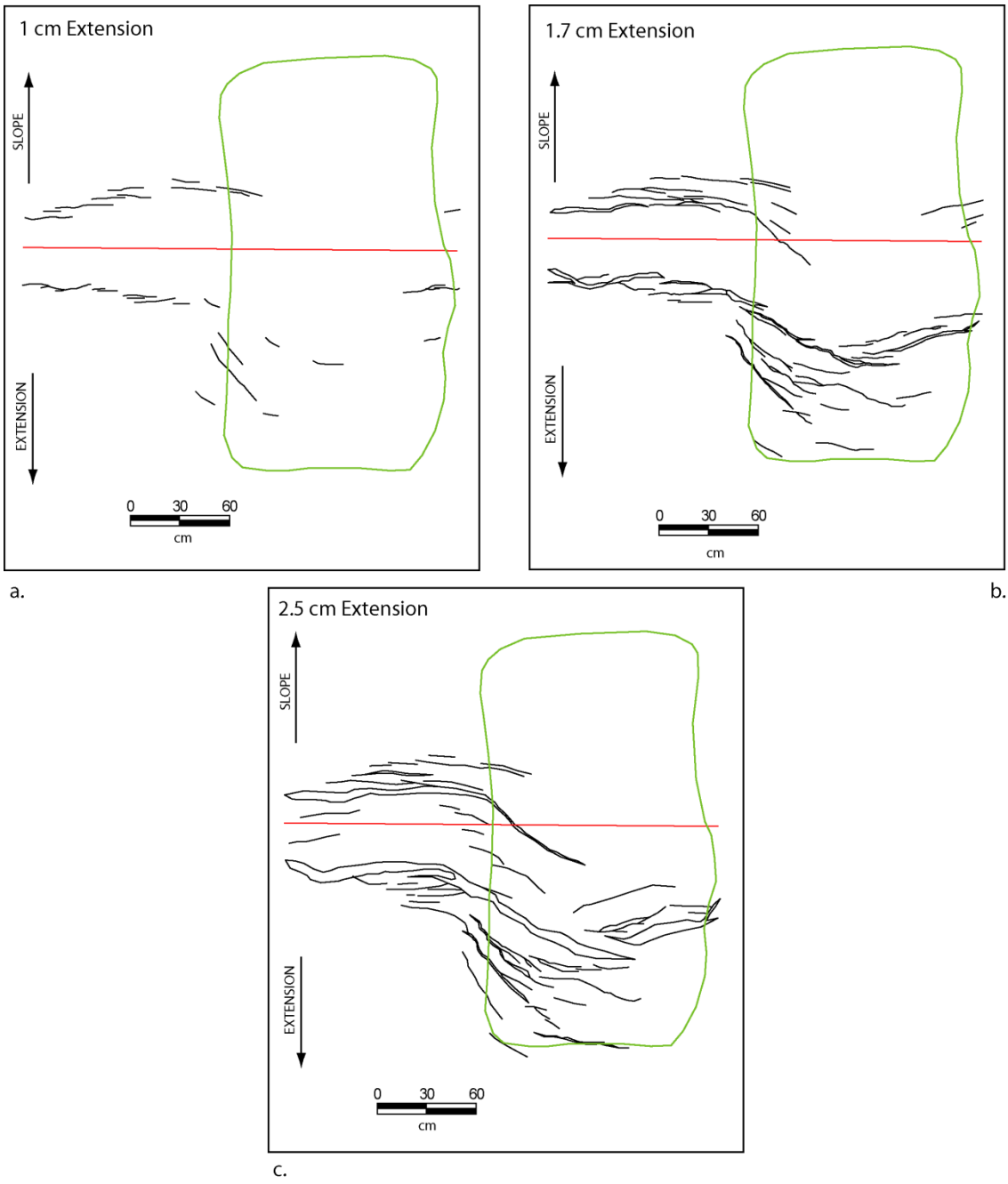

Figure B3: (a-c) Incremental stages of extension showing fault growth and patterns in setup B. Base plate contact is marked with red and the outline of the silicone polymer by green.

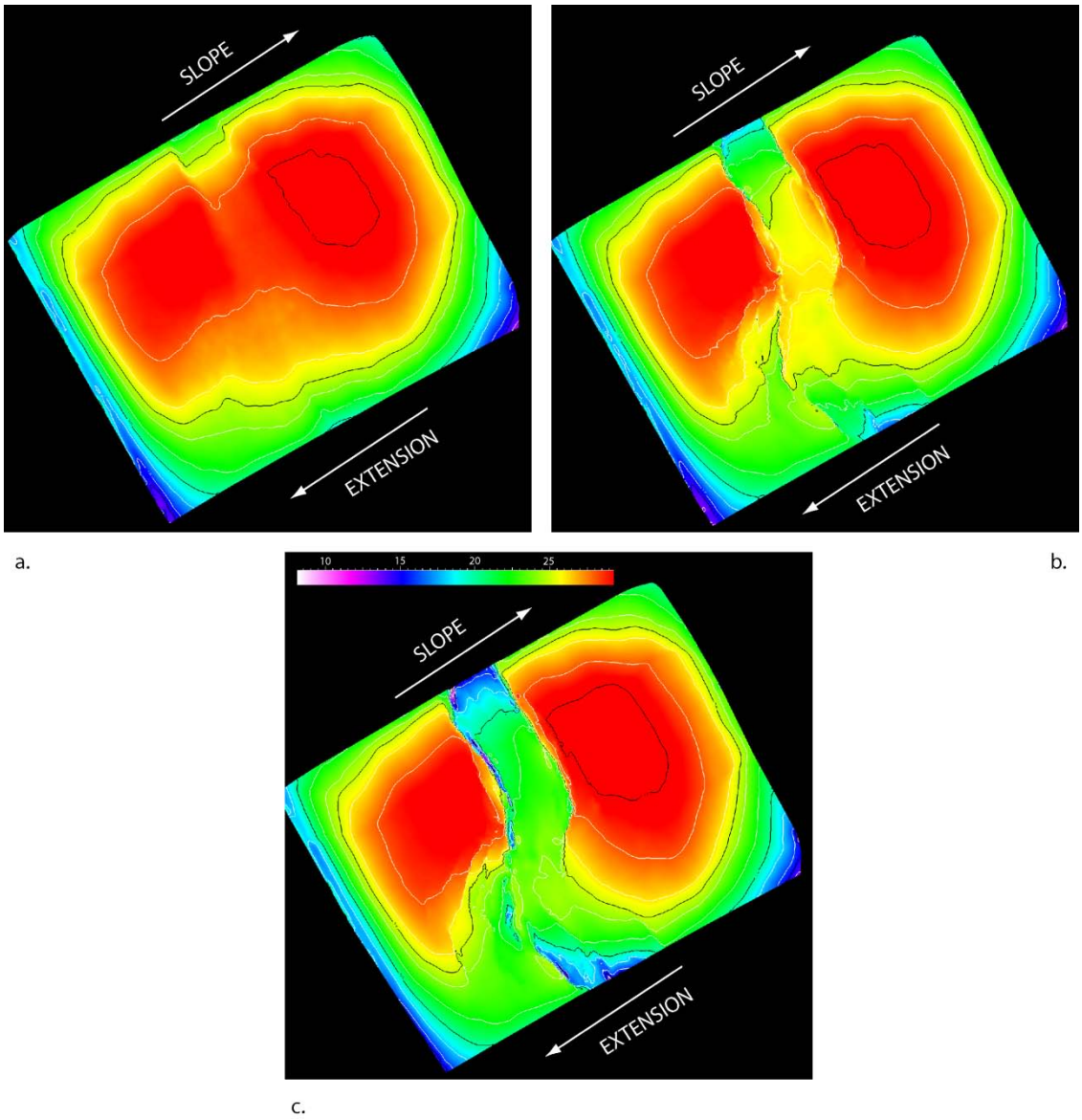

Figure B4: Three dimensional geometry of the clay surface through the stages of extension in setup A. High areas indicated by red and lows by blue. Tilt correction has been performed to this surface in order to take away 5° inclination.

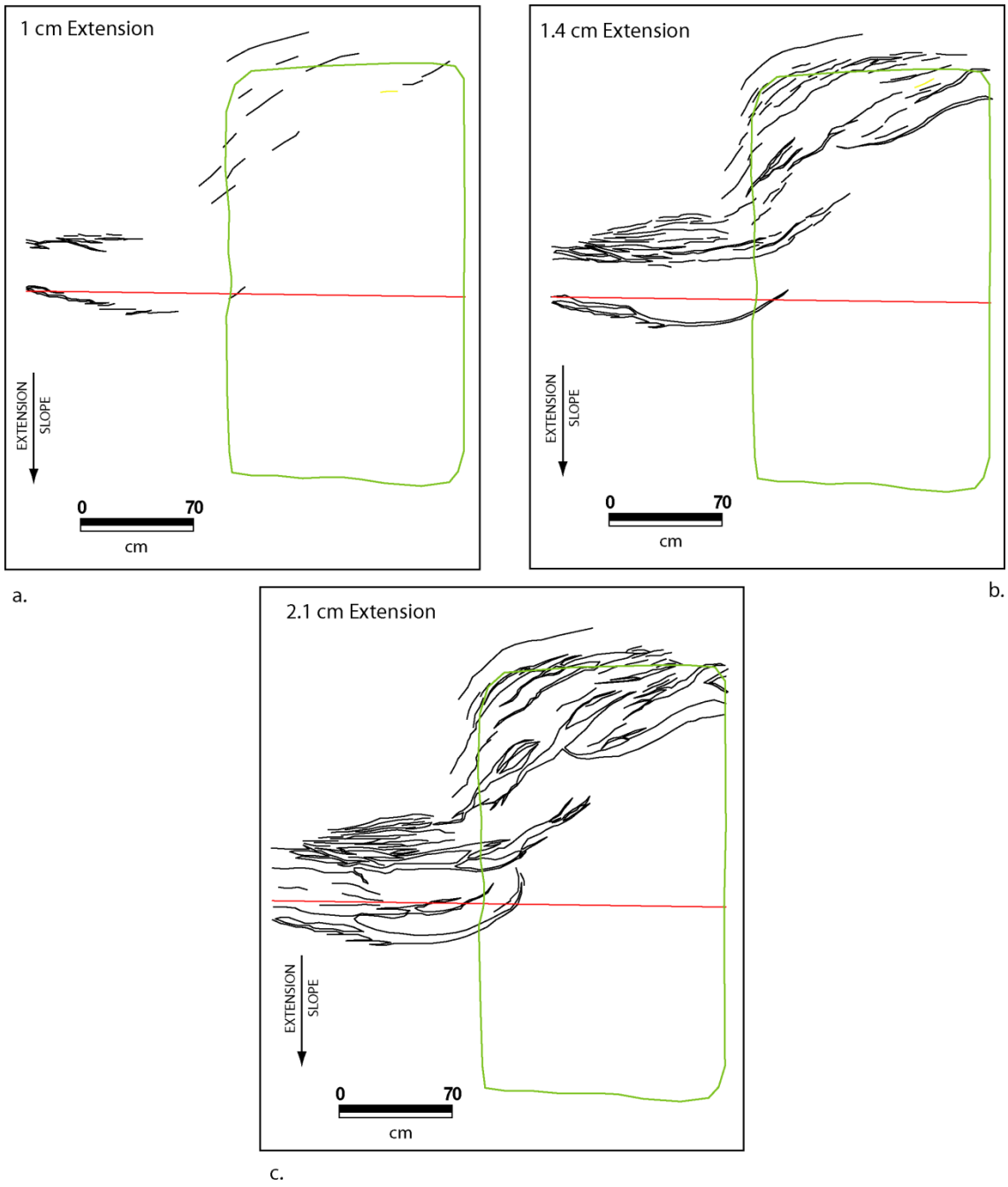

Figure B5: (a-c) Incremental stages of extension showing fault growth and patterns in setup C. Base plate contact is marked with red and the outline of the silicone polymer by green.

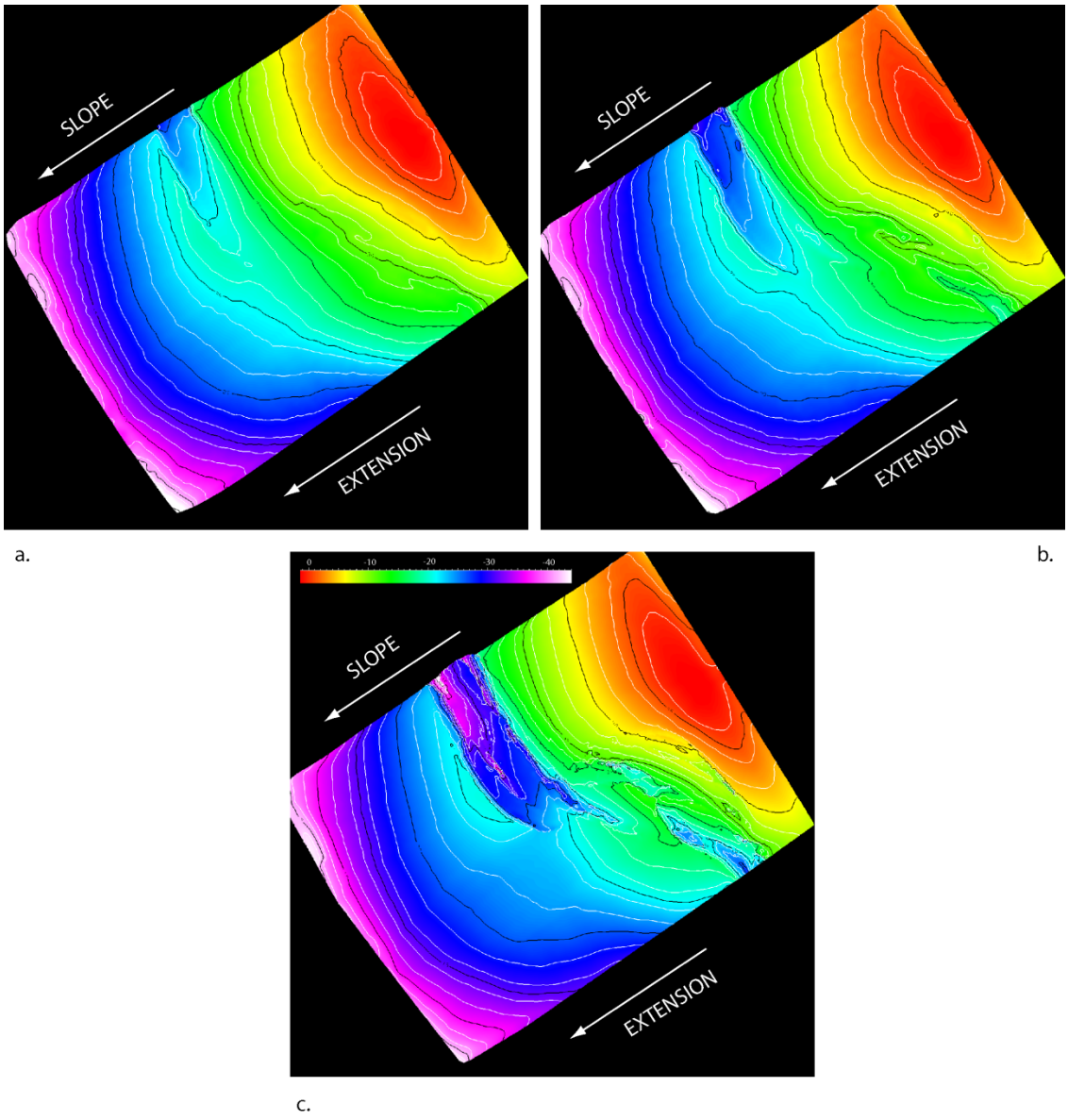

Figure B6: Three dimensional geometry of the clay surface through the stages of extension in setup A. High areas indicated by red and lows by blue.

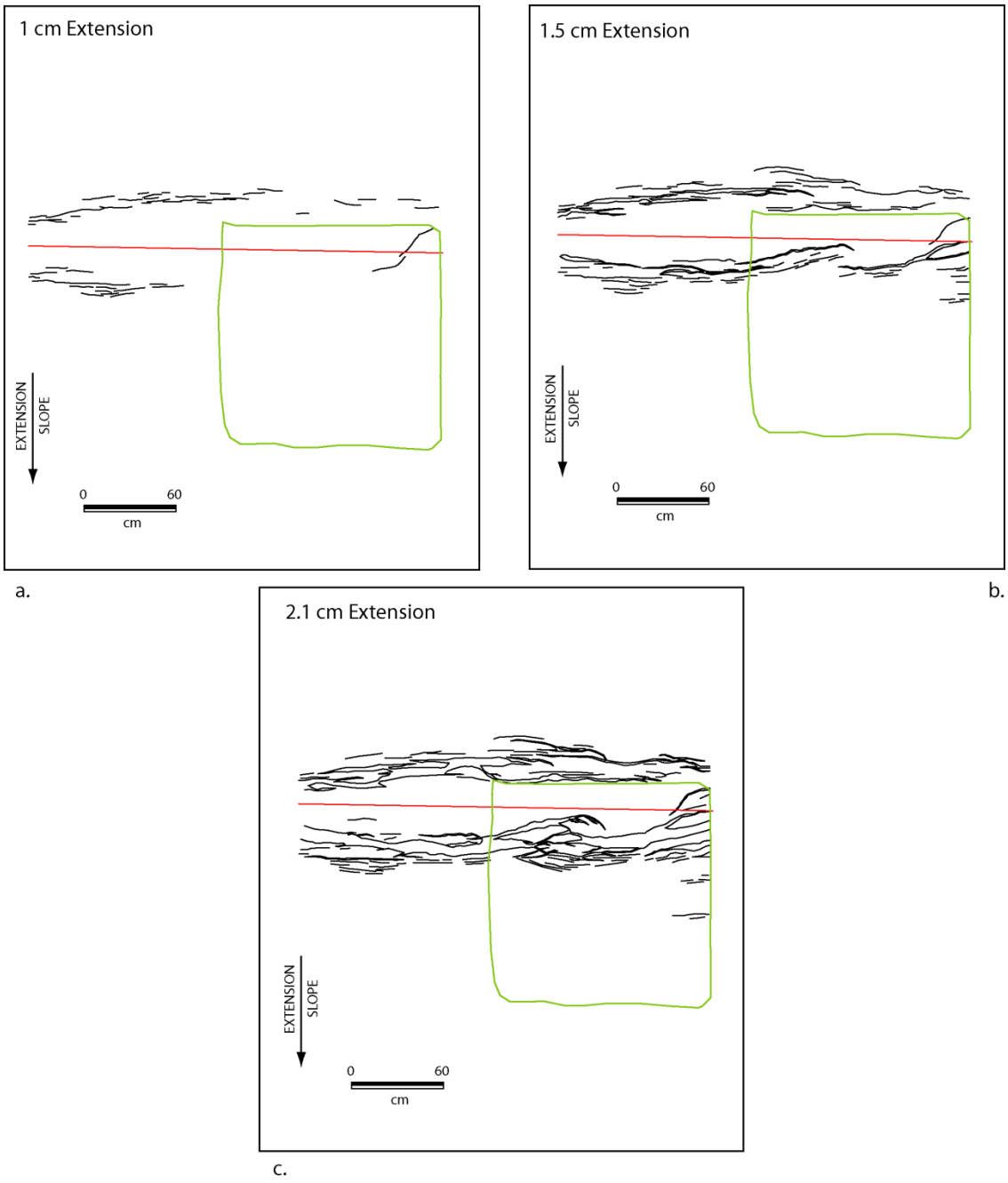

Figure B7: (a-c) Incremental stages of extension showing fault growth and patterns in setup D. Base plate contact is marked with red and the outline of the silicone polymer by green.

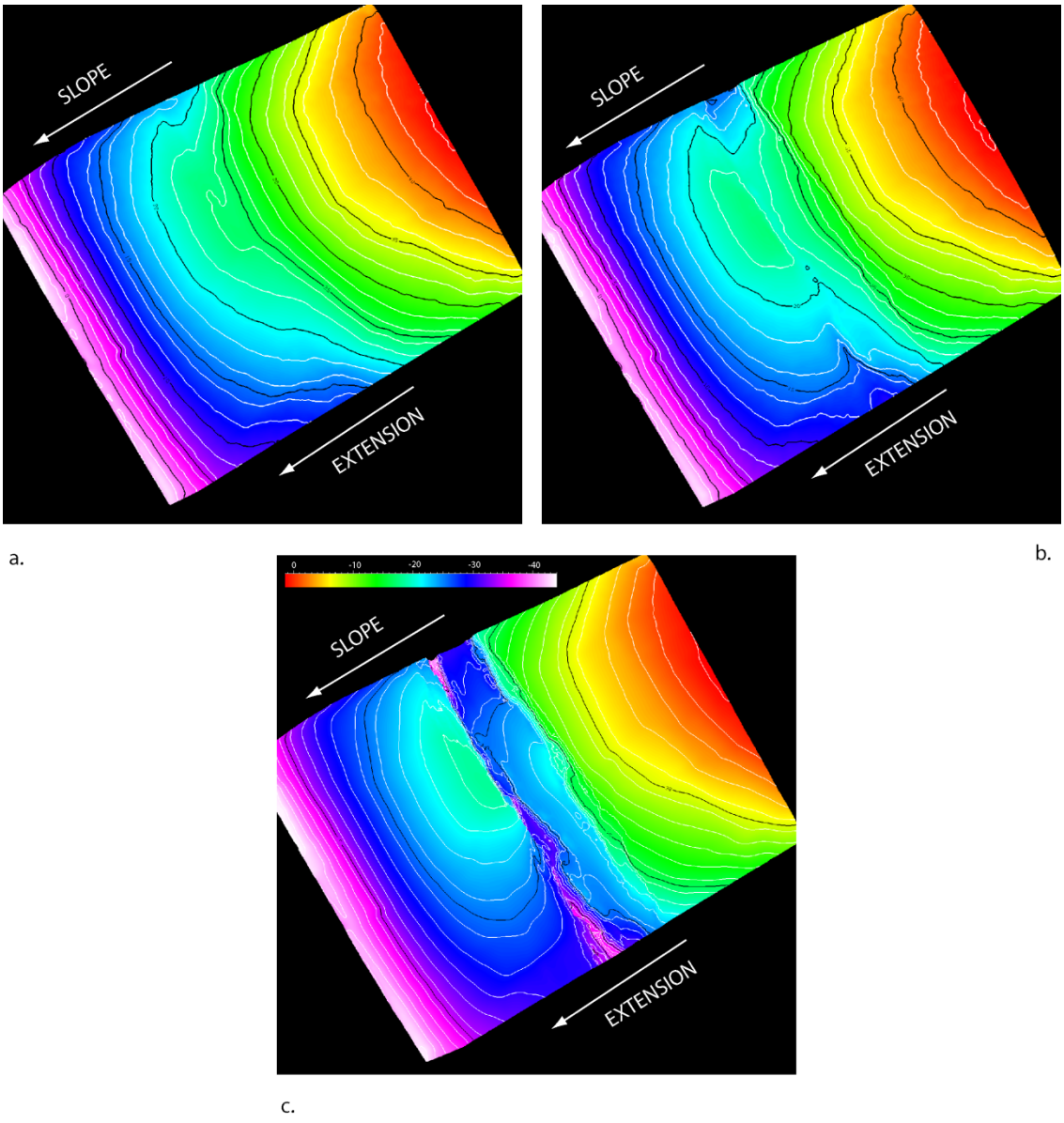

Figure B8: Three dimensional geometry of the clay surface through the stages of extension in setup A. High areas indicated by red and lows by blue.

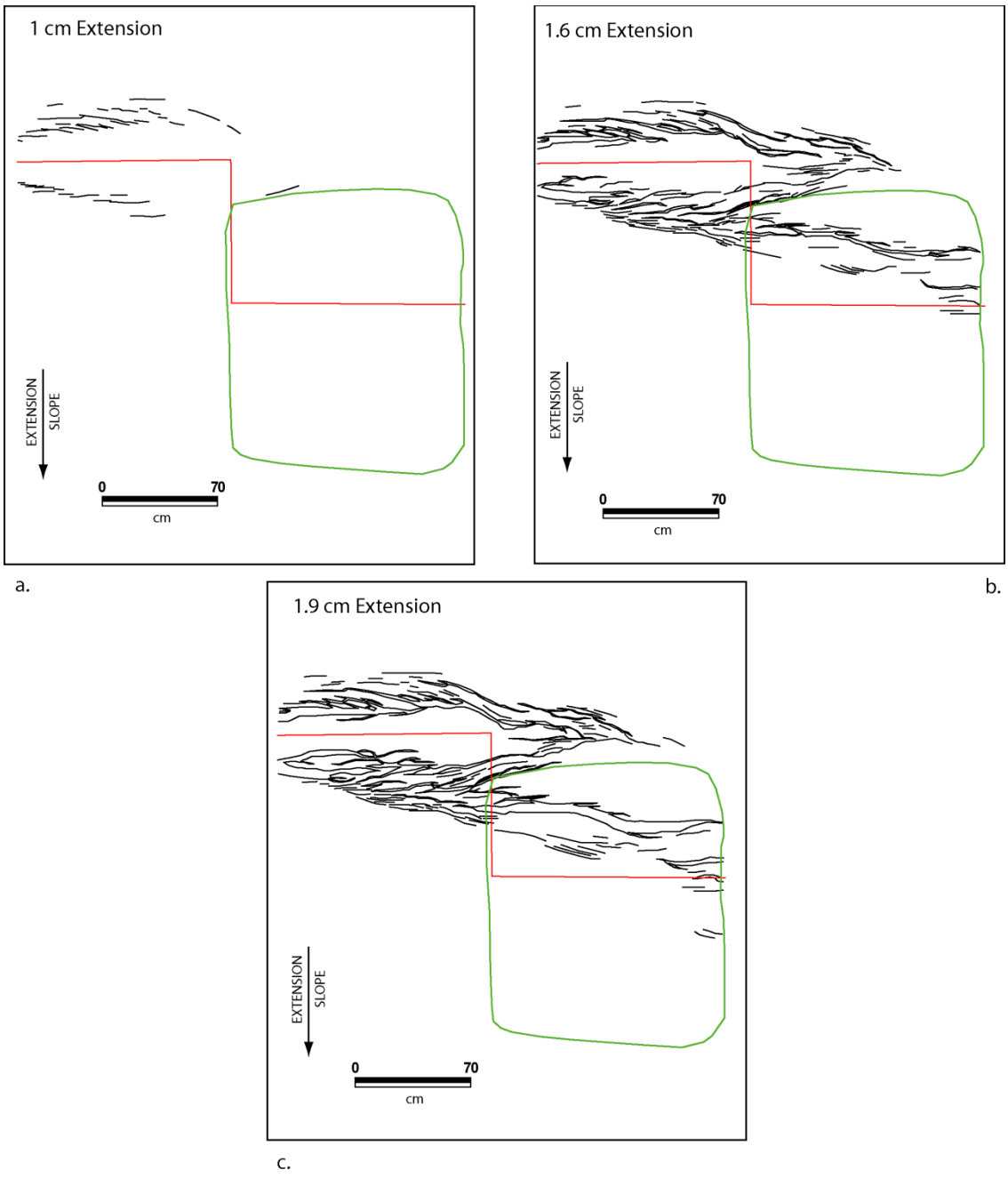

Figure B9: (a-c) Incremental stages of extension showing fault growth and patterns in setup E. Base plate contact is marked with red and the outline of the silicone polymer by green.

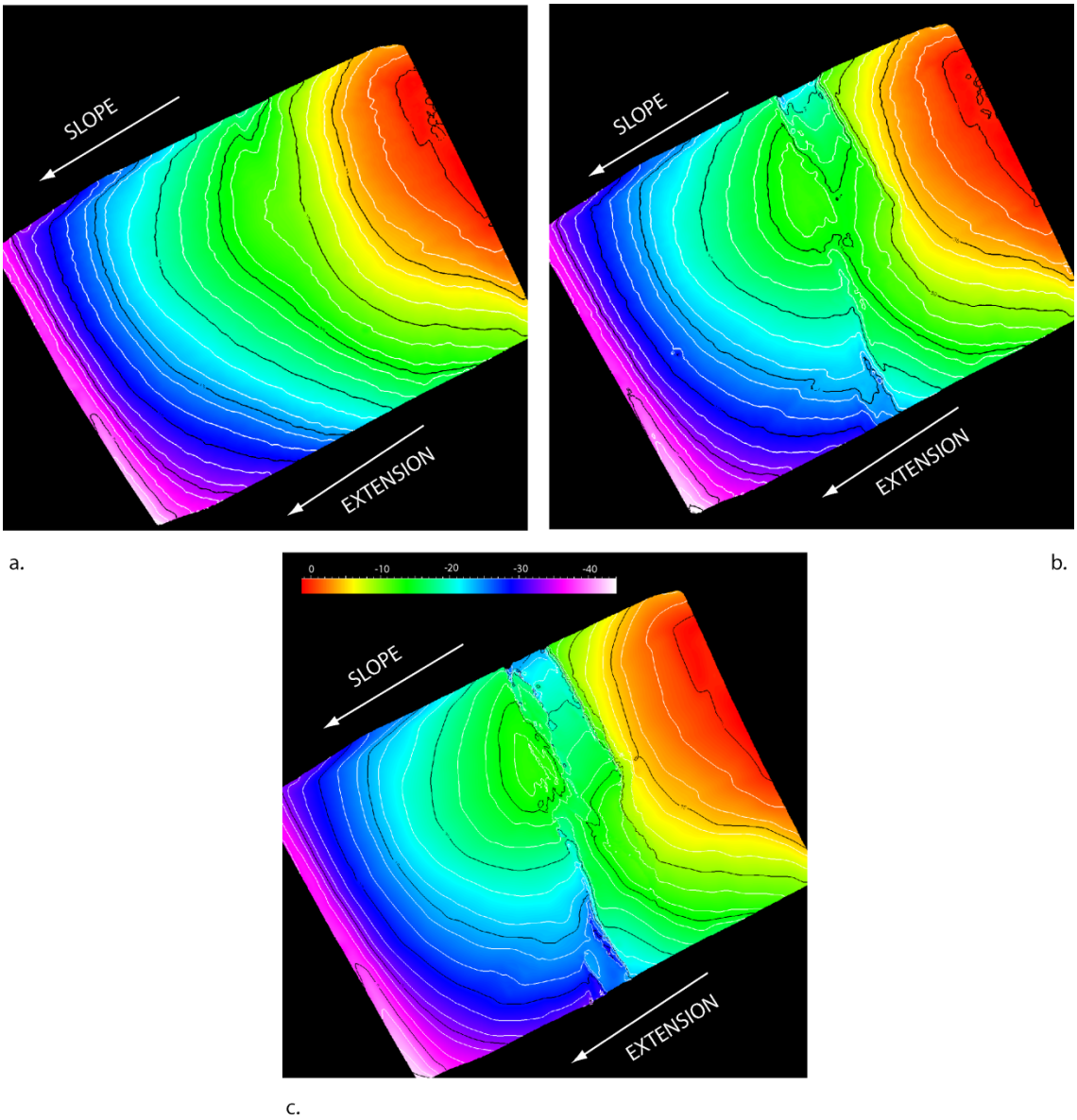

Figure B10: Three dimensional geometry of the clay surface through the stages of extension in setup A. High areas indicated by red and lows by blue.